Recent Progress on Spray Pyrolysis for High Performance Electrode Materials in Lithium and Sodium Rechargeable Batteries

Yujie Zhu, Seung Ho Choi, Xiulin Fan, Jaeho Shin, Zhaohui Ma, Michael R. Zachariah,* Jang Wook Choi,* and Chunsheng Wang*

Advanced electrode materials have been intensively explored for next-generation lithium-ion batteries (LIBs), and great progresses have been achieved for many potential candidates at the lab-scale. To realize the commercialization of these materials, industrially-viable synthetic approaches are urgently needed. Spray pyrolysis (SP), which is highly scalable and compatible with on-line continuous production processes, offers great fidelity in synthesis of electrode materials with complex architectures and chemistries. In this review, motivated by the rapid advancement of the given technology in the battery area, we have summarized the recent progress on SP for preparing a great variety of anode and cathode materials of LIBs with emphasis on their unique structures generated by SP and how the structures enhanced the electrochemical performance of various electrode materials. Considering the emerging popularity of sodium-ion batteries (SIBs), recent electrode materials for SIBs produced by SP will also be discussed. Finally, the powerfulness and limitation along with future research efforts of SP on preparing electrode materials are concisely provided. Given current worldwide interests on LIBs and SIBs, we hope this review will greatly stimulate the collaborative efforts among different communities to optimize existing approaches and to develop innovative processes for preparing electrode materials.

1. Introduction

Since the introduction to market by Sony in the early 1990s,[1] lithium-ion batteries (LIBs) have become dominate power sources for consumer electronics and have been recognized as a critical enabling technology to make electric vehicles (EVs)/hybrid electric vehicles (HEVs) a success.[2] They are also being used to store carbon-free and renewable energy sources, such as solar, wind, and ocean (wave, currents, and tides), because these renewable energy sources are seasonal and intermittent. Compared with other battery systems, such as lead-acid, Ni-Cd, and Ni-MH batteries, LIBs present much higher energy densities (both gravimetric and volumetric), and also feature no memory effects or slow self-discharge, which make them popular in many applications.[3]

The 1st generation commercial LIBs utilized $LiCoO_2$ and graphite for the cathode and anode, respectively. The energy density of LIBs is mainly limited by the capacities of electrode materials. To further increase the energy density of LIBs to meet the requirements of EVs and other high energy applications, considerable effort has been made to seek cathode and anode materials with higher capacities over the past decades.[4–6] Several candidates have demonstrated significant advantages over $LiCoO_2$ cathode and graphite anode used in the 1st generation commercial LIBs.[7–9]

The electrochemical performance of a LIB is mainly determined by properties of its anode and cathode. These properties can be roughly classified into: intrinsic material properties (such as theoretical capacity, ion conductivities, volume changes upon charge-discharge, and voltage with respect to lithium metal) and extrinsic structure properties (for example active materials' particle size, morphology, porosity, and spatial distribution). While it is relatively difficult to tune the intrinsic natures of electrode materials,[10] appropriate synthetic methods offer the possibility to manipulate the electrode microstructure/architecture to improve electrochemical performance. There are numerous examples demonstrating how the performance is highly dependent on electrode structure.[11–14]

Prof. Y. Zhu
School of Chemistry and Environment
Beihang University
Beijing 100191, P. R. China
S. H. Choi, J. Shin
Department of Chemical
and Biomolecular Engineering
Korea Advanced Institute of Science and Technology (KAIST)
Yuseong-gu, Daejeon 305–701, Republic of Korea
Dr. X. Fan, Dr. Z. Ma, Prof. M. R. Zachariah, Prof. C. Wang
Department of Chemical and Biomolecular Engineering
University of Maryland College Park
MD 20742, USA
E-mail: mrz@umd.edu; cswang@umd.edu
Prof. J. W. Choi
Graduate School of Energy
Environment, Water, and Sustainability (EEWS)
Korea Advanced Institute of Science and Technology (KAIST)
Daehakro 291, Yuseong-gu, Daejeon 305–701, Republic of Korea
E-mail: jangwookchoi@kaist.ac.kr

ADVANCED
ENERGY
MATERIALS
www.advenergymat.de

ADVANCED
SCIENCE NEWS
www.advancedsciencenews.com

REVIEW

The literature offers a wide variety of synthetic methods for fabricating advanced electrode materials with special structures, designed to enhance the electrochemical performance of electrode materials. Unfortunately, most reported synthetic methods, especially those methods for producing electrode materials with beneficial structures for electrochemical performances, fail in their potential for scale-up due to high cost and other scalability issues (for example, low yield and complex, multiple synthetic steps). To develop next generation high energy density commercial LIBs, suitable synthetic methods for mass-production of advanced electrode materials with desired structures are needed. However, in contrast to the numerous excellent review articles focused on the intrinsic properties, structures, and electrochemical performances of active materials and electrodes,[4,6,11,15–29] only very limited number of articles discuss synthetic methods for electrode materials, particularly those that might be considered industrially-viable.[30–36] Considering recent rapid developments of advanced electrode materials at the lab-scale and the upcoming massive consumption of LIBs in the future due to the widespread use of EVs/HEVs, industrially-viable synthetic methods are urgently needed for mass-production of these new electrode materials.

The ideal manufacturing methods for electrode materials at industrial-level should meet several critical criteria, including low cost, high yield, simple operation, ability to rationally designing materials' properties (e.g., stoichiometry, morphology, porosity, particle size, etc.), and environmental benignity. This review article aims at such a method, spray pyrolysis (SP), which is scalable, compatible with on-line continuous production processes, and offers very high fidelity in synthesis of multi-element electrode materials with complex architectures and chemistries, from relatively common precursor materials.[37–40]

SP has been used for years in various applications (fuel cell,[41] photocatalyst,[42] display,[43] sensor,[44] bioceramic,[45] etc.) but has also found unique advantages for producing battery electrode materials,[46] such as uniform mixing among composite components, void space control to accommodate large volume change of active materials, formation of secondary micro-particles while containing nanostructured primary particles, and established scalability through long manufacturing history. Such unique capabilities of SP are in comparison with other synthetic methods available for battery active materials, such as solid-state reaction and co-precipitation, in a sense that SP can result in a narrow size distribution of particles typically much smaller than classical methods and is able to produce hollow internal structures. These structural advantages can play a crucial role in improving key electrochemical properties of various electrode materials for rechargeable batteries as described in Section 3 and 4, although SP occasionally requires additional heat treatments to increase the crystallinity. Furthermore, because the most common solvent for SP is water there is no need for dealing with liquid waste stream and recycling, while the economics of organic chemical free system are highly beneficial. In fact, the application of SP in the field of LIBs has shown rapid growth in recent years (**Figure 1**), and thus a review regarding this topic is timely. Since the basis of this review aims to summarize recent progress achieved by SP for preparation of electrode materials, the fundamental

Michael Zachariah is Patrick and Marguerite Sung Distinguished Professor in Chemical Engineering and Chemistry. He has expertise in aerosol generated materials and has published extensively on the metrology of nanoparticles in both the liquid and gas phases. This includes the development of new mass-spectrometry and ion-mobility methods to characterize nanoparticles and their reactivity.

Jang Wook Choi is presently Associate Professor in Graduate School of Energy, Environment, Water, and Sustainability (EEWS) at Korea Advanced Institute of Science and Technology (KAIST) in Korea. Prof. Choi received B.S. from Department of Chemical Engineering at Seoul National University in 2002 and Ph.D. from Division of Chemistry and Chemical Engineering at Caltech in 2007 under the supervision of Prof. James R. Heath. Prof. Choi conducted Postdoctoral research in Department of Materials Science and Engineering at Stanford University under the supervision of Prof. Yi Cui. His research focuses on materials design and characterization, targeting rechargeable batteries and CO_2 capture.

Chunsheng Wang is presently Professor in the Chemical & Biomolecular Engineering at the University of Maryland. He received Ph.D in Materials Science & Engineering from Zhejiang University, China in 1995. Prior to joining University of Maryland in 2007, he was Assistant Professor in Department of Chemical Engineering at Tennessee Technological University (TTU) in 2003–2007 and research scientist in the Center for Electrochemical System and Hydrogen Research at Texas A&M University in 1998–2003. His research focuses on rechargeable batteries and fuel cells.

working principles of some popular electrode materials will only be briefly touched. Readers, interested in learning more about those aspects, will find many outstanding review articles in the literature.[6,15,16,20,27,28] Following the introduction section,
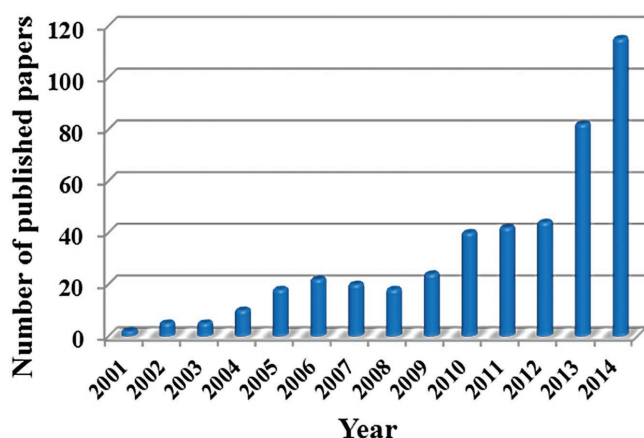
Figure 1. The number of published paper with topics "lithium ion battery" and "spray pyrolysis" from 2001 to 2014. Data from Web of Science.

the working principles of SP along with three typical atomization techniques will be presented. After that, electrode materials (both anode and cathode) for LIBs designed by SP will be thoroughly discussed with emphasis on their unique structures generated by SP and how the structures enhanced the electrochemical performance of various electrode materials. Then, considering the emerging popularity of sodium-ion batteries

(SIBs) and the great similarity between LIBs and SIBs,[47–51] recent electrode materials for SIBs produced by SP will also be discussed. Finally, the powerfulness, design procedures, and future efforts of SP for fabrication of electrode materials will be briefly discussed.

2. Spray Pyrolysis (SP) Methods

Since its invention, SP has found a variety of applications, including batteries, fuel cells, superconductors, catalysis, and thin film deposition.[37] It has been used to generate a wide variety of materials, including metals, metal alloys, metal oxides, metal nitrides, and organic-inorganic composites, with diverse structures (**Figure 2**).[38] In sharp contrast to conventional batch reactions based synthetic methods, e.g., solid-state, precipitation, hydrothermal, and sol-gel, SP is a continuous flow synthetic technique requiring relatively simple apparatus, that can be easily scaled up with a productivity of tons per day.[52] The basic concept is that a precursor solution is first atomized (also called nebulized) into mist, which contains numerous micronsized droplets, by an atomizer. Then, these droplets are introduced into a heat source (e.g., tube furnace, flame, etc.) by a carrier gas. Inside the heat source, each droplet serves as microreactors in which a series of physical and chemical processes,
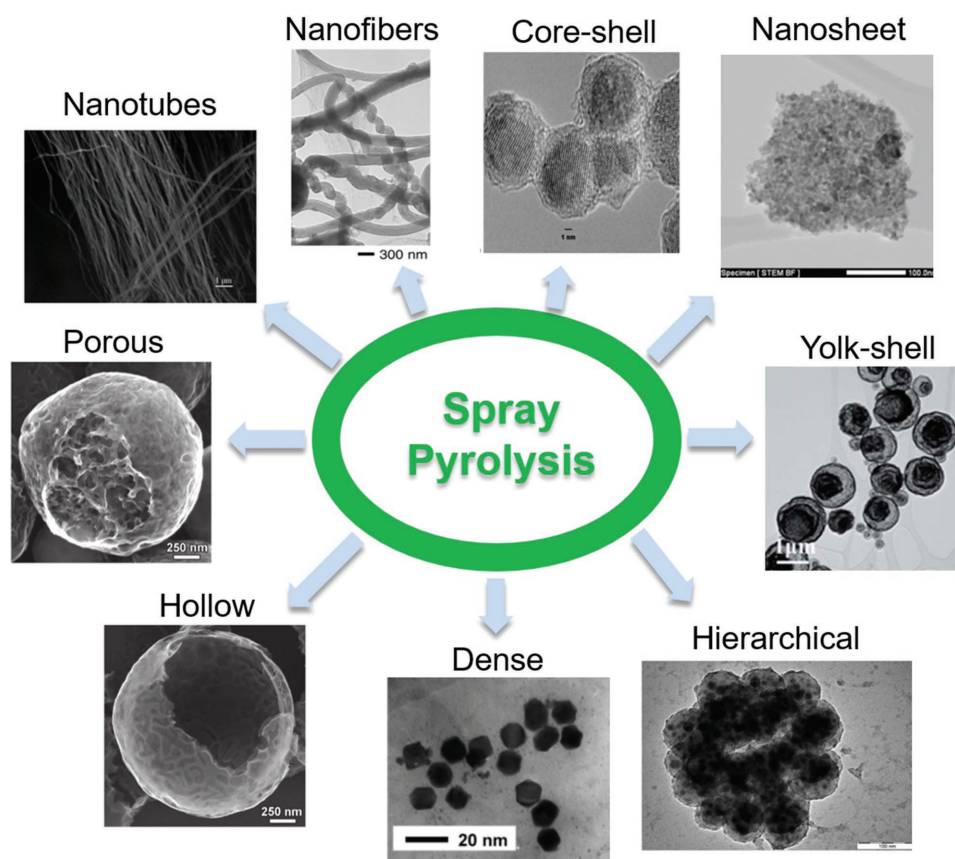

Figure 2. Various particle morphologies prepared by SP. Reproduced with permission.[62,64,65,88,90,98,102,220] Copyright 2006, 2012, 2005, 2013, 2005, 2013, 2014, 2008, Elsevier, Wiley-VCH, Elsevier, Royal Society of Chemistry, American Chemical Society, Royal Society of Chemistry, Elsevier, American Chemical Society
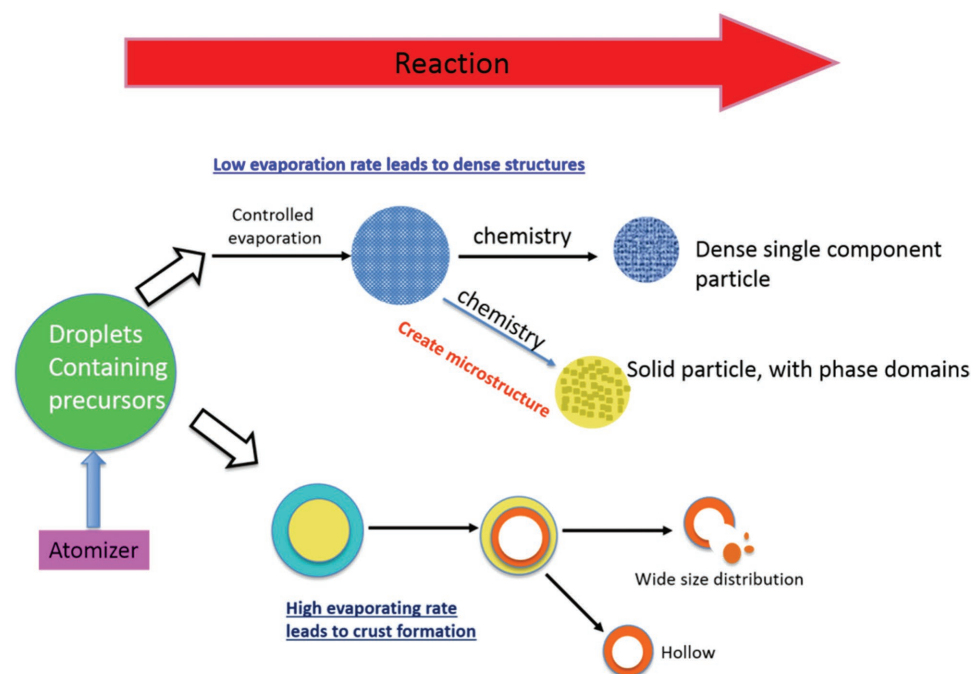
**ADVANCED
ENERGY
MATERIALS**

www.advenergymat.de

**ADVANCED
SCIENCE NEWS**

www.advancedsciencenews.com

Figure 3. Evolution of the particles processing in spray pyrolysis, demonstrating different morphologies. Reproduced with permission.[53] Copyright 1998, Wiley-VCH.

including solvent(s) vaporization, solute(s) precipitation/diffusion/decomposition/reaction, and particles agglomeration/sintering, take place.[52] Finally, the products are collected at the outlet by filters (typically either electrostatically or bag house). The chemical and physical properties of the final products synthesized by SP can be facilely controlled by simply changing the composition of precursor solution and process parameters (drop size, residence time, temperature, etc.), which makes SP particularly useful for preparation of composite materials. A wide variety of precursors, including metal acetates, chlorides, nitrates, lactate, citrate and oxalates solution, have been employed to fabricate a variety of mixed metal materials. Such precursors have the advantage of being inexpensive and readily water soluble. The final particle size is determined by the initial droplet size distribution, which depends on the type of atomizer used and the concentration of solute used. So in principle there is so lower size limit of particles that can be fabricated. However, from a practical point of view, SP is not a good method to produce particles under 50 nm, simply because the mass product rate becomes exceedingly small. Nominal thermal conditions are typically below 1000 °C, enabling the use of standard tubular furnaces, and most in-flight residence time is less than 5 sec. However, subsequent post-processing can of course be conducted on the collected powders (annealing, calcination, oxidation, etc.) in order to tune final chemistries or morphologies of the products. Care must be taken during the reaction process, since typically different components (precursors) will precipitate and phase segregation will take place within the aerosol droplet. In some cases, this is a desirable outcome if the objective is to make core shell or other granular materials within the particle. One common problem in SP is the formation of hollow shell like particles. Typically, this occurs when a solute

concentration gradient is developed during the evaporation of the solvent, leading to supersaturation near the droplet surface and precipitation of one or more of the solute components near the outer edge of the droplet. A resulting crust, if sufficiently impermeable to the solvent, will result in a pressure built up upon subsequent heating and thus explosion of particles happens. Mitigation of this requires adjustment of precursor concentration, and typically a pre-drying stage at low or moderate temperature. In general, high-solubility precursors, low solution concentrations, small droplet sizes, and long residence times promote dense particle formation.

Figure 3 summarizes the general steps in SP.[53] One aspect of the process should be noted in Figure 3, and that is the lack of any discussion of aggregation between particles. If one considers the synthesis of nominal 100 nm particles, using conventional atomizers which generate droplets at a concentration of $\approx 10^6$ particles per cm^3, it is easy to compute that the characteristic coagulation time is ≈ 100 sec. This is typically 10 times longer than nominal residence times typically employed in SP, and thus one should not expect significant aggregation. Electron microscopy bears this out, as one typically sees uniform and highly spherical particles from SP.

A variety of SP is to directly deposit the droplets to a heated substrate prior to solvent evaporation, enabling the direct formation of thin films.[54] While heating is axiomatic in SP, in some cases, no pyrolysis (i.e., thermal decomposition) and only solvent evaporation is required, resulting in collection of solid products of the precursor materials but in particulate form. This process is often called spray drying and is a common method employed in the food industry. Considering the similarity between SP and spray drying, we will treat spray drying as SP in the following text.

wileyonlinelibrary.com
© 2016 WILEY-VCH Verlag GmbH & Co. KGaA, Weinheim

**ADVANCED
SCIENCE NEWS**
www.advancedsciencenews.com

**ADVANCED
ENERGY
MATERIALS**
www.advenergymat.de

REVIEW

Production rate and droplet size distribution, and thus final product particle size distribution, are highly dependent on the characteristics of atomizer and properties of the precursor solutions.[37] Three types of atomization techniques are often used in SP, namely ultrasonic atomization, pneumatic atomization, and electrohydrodynamic atomization. The working principles and characteristics of these three types of atomization methods are discussed in the following text.

2.1. Ultrasonic Atomization

The discovery of ultrasonic atomization can be traced back to 1927 when Wood and Loomis first observed the formation of mist from an ultrasonic fountain,[55] and it has found widespread application in household humidifiers. It was revealed that the capillary surface waves play a major role during the ultrasonic atomization and the working principle of ultrasonic atomization mainly involves momentum transfer.[52] When ultrasound is propagated perpendicular to a liquid film, capillary surface waves will be generated. These capillary waves contain peaks and troughs, whose amplitude depends on the intensity of the underlying source. When the exciting vibration is sufficiently strong, a critical amplitude is achieved so that the peaks of the surface capillary waves become unstable and break off from the bulk of the liquid, ejecting fine droplets. Then, ultrasound plays a role in isolating one droplet from another. **Figure 4** shows ultrasonic SP apparatus with dual furnaces and the digital image of an ultrasonic fountain and mist produced at 1.7 MHz.[56] The aerosol droplet size was correlated to the capillary wavelength by Lang in 1962.[57] Lang experimentally showed that the median droplet diameter was a constant fraction of the capillary wavelength. Since the capillary wavelength is related to the ultrasonic frequency, the aerosol droplet size can be regulated by changing the ultrasonic frequency. The relationship between ultrasonic frequency and aerosol droplet size was described by the Lang equation:[57]

$$D_{droplet} = 0.34 \left(\frac{8\pi\gamma}{\rho f^2} \right)^{1/3} \tag{1}$$

where $D_{droplet}$ is the mean diameter of the droplets, γ is the surface tension of the solution, ρ is the density of the precursor solution, and f is the frequency of the ultrasound. Equation (1) indicates that, to obtain droplets with smaller diameters, higher frequency is needed. Frequencies higher than 1 MHz are generally used to synthesize nanomaterials.[52] Equation (1) also suggests that besides frequency, the droplet size is also determined by the properties of the precursor solution, i.e., surface tension and density of the solution. Precursor solutions with low surface tension and high mass density will facilitate small droplet generation.

Compared with other atomization techniques, ultrasonic atomization has the advantages of energy-efficiency, affordability, and low velocity of initial droplets. However, ultrasonic atomization has limitations on generating droplets from solution with high viscosity.

2.2. Pneumatic Atomization

Pneumatic atomization refers to the processes to generate aerosol droplets by applying a high relative velocity between a gas and a liquid stream. Since two fluid streams are involved in this process, it is often called two-fluid atomization.[58] Pneumatic atomization is a common method, employed widely, for example atomization of fuel in combustion engines and fluidized bed coating.[58] The fundamental mechanism of pneumatic atomization is that a high relative velocity between a gas and a liquid creates strong shear force over liquid surfaces, and subsequently causes the liquid to disintegrate into aerosol droplets. Despite the various designs of pneumatic atomizers, two steps generally occurred in pneumatic atomization (**Figure 5**).[59]

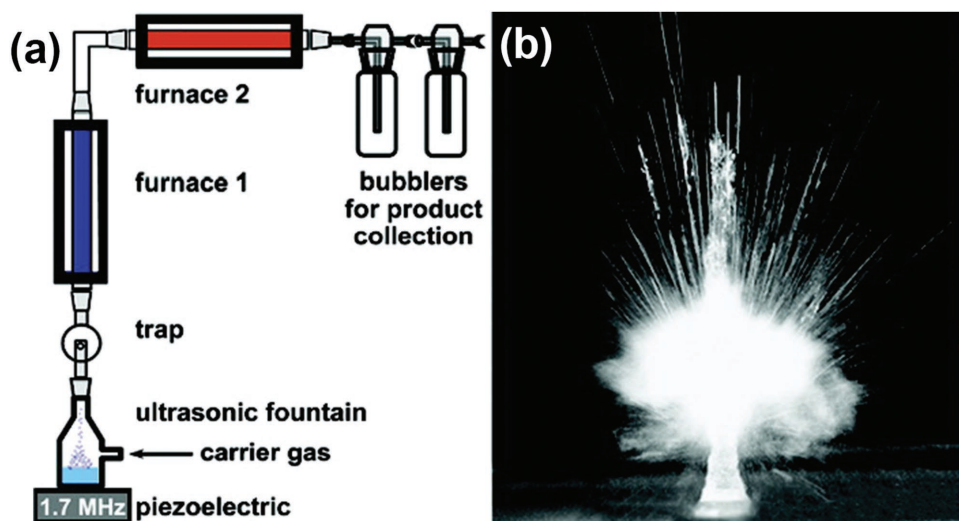First, the liquid is disintegrated into filaments and large droplets, which are secondarily further shattered into

Figure 4. a) Ultrasonic spray pyrolysis apparatus with dual furnaces. b) The digital image of an ultrasonic fountain and mist produced at 1.7 MHz. Reproduced with permission.[56] Copyright 2005, American Chemical Society.
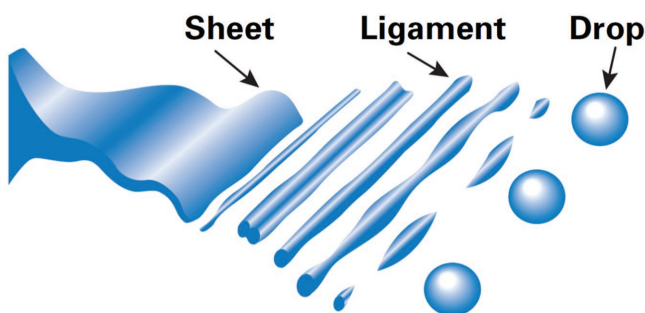
ADVANCED
ENERGY
MATERIALS
www.advenergymat.de

ADVANCED
SCIENCE NEWS
www.advancedsciencenews.com

REVIEW

Figure 5. Schematic illustration of working principles of pneumatic atomization. Image provided courtesy of Spraying Systems Co. Wheaton, IL USA, www.spray.com. Reproduced with permission.[59] Copyright 2006, Spraying System Co.

smaller droplets by the action of the kinetic energy of the gas jet. This entire atomization process is accomplished by a high relative velocity between the gas and the liquid creating strong shear force over the liquid surface. In general, the mean aerosol droplet size can be reduced by increasing the relative velocity between the gas and the liquid. The droplet size is also affected by the properties of liquid and gas, such as surface tension, density, and viscosity of liquid, and velocity and density of gas flow. The metric used to characterize this class of atomization is the non-dimensional Weber number:

$$We = \frac{\rho \delta v^2}{\gamma} \qquad (2)$$

where ρ is the density of the liquid, δ is the characteristic liquid sheet thickness, v is its relative velocity to the gas phase, and γ is the surface tension. Essentially the Weber number expresses the ratio of kinetic energy to surface energy.

The resultant average drop diameter, d can be nominally expressed as:

$$d \sim \frac{\delta}{We^{0.5}} \qquad (3)$$

2.3. Electrohydrodynamic Atomization

Electrohydrodynamic atomization, also commonly called electrospray, utilizes electrostatic forces to generate fine aerosol droplets. An intense electric field is applied between the surface of a liquid at a capillary nozzle outlet and a grounded surface. When the applied voltage is above a certain threshold, the liquid is drawn into a cone. The equilibrium shape of the cone was theoretically modelled by Geoffrey Ingram Taylor, and this characteristic shape is often called "Taylor cone" (**Figure 6**a). When the applied voltage is high enough, electrostatic force exerted on the liquid overcomes the surface tension of liquid, and micro-jet will be extracted from the Taylor cone. This micro-jet elongates to a fine filament and disperses into small aerosol droplets (Figure 6a).

There are several different modes of electrostatic atomization (Figure 6b), depending on the form of the meniscus, the motion pattern of the jet, and the way the jet disintegrates into droplets.[60] The aforementioned Taylor cone-jet mode is the most frequently used because it can stably generate monodisperse particles. The precursor solution, which can be sprayed in a cone-jet mode, usually has a conductivity ranging from 10^{-8}–10^{-4} S m^{-1}.[61] The droplet size is mainly determined by three main factors: electric field strength, liquid flow rate, and properties of fluid, such as viscosity, surface tension, conductivity and relative permittivity. The droplet size is usually correlated with these parameters by following equation:[60]

$$d = \alpha \frac{Q^a \varepsilon_0^b \rho^c}{\sigma^d \gamma^e} \qquad (4)$$

where d is the diameter of the droplet, α is a constant which is determined by the permittivity of the liquid, Q is the flow rate of
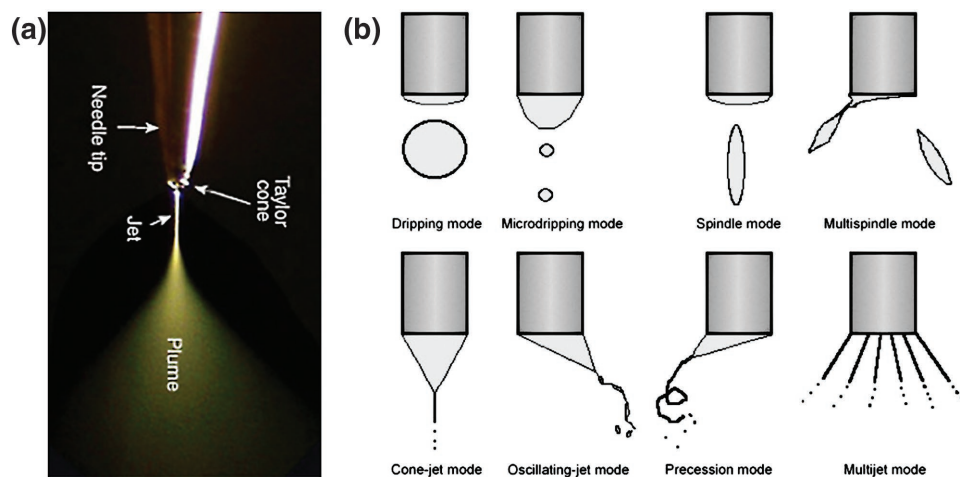

Figure 6. a) The digital image of electrohydrodynamic atomization under a cone-jet mode. Image provided courtesy of New Objective, Inc. Wobrun, MA USA · http://www.newobjective.com. Copyright 1997, New Objective, Inc. b) Various modes of electrohydrodynamic atomization. Reproduced with permission.[60] Copyright 2008, Elsevier Ltd.

the liquid, ε_0 is the vacuum permittivity, ρ is the liquid density, σ is the liquid conductivity, and γ is the surface tension of the liquid. The exponents a, b, c, d, and e in Equation (4) are constants, which vary slightly depending on different authors.[60]

The droplet generated by electrohydrodynamic atomization is usually much smaller than that produced by pneumatic atomization and ultrasonic atomization. Furthermore, because the droplets are unipolar charged, they are essentially self-dispersing, and thus do not nominally aggregate. The result is a much narrower size distribution than that can be achieved by other atomization methods. The primary requirement is that the precursor solution has to be electrically conductive, which is not usually a concern for the type of material nominally employed (metal salts), and the use of high voltage sources (2–10 kV). The major limitation of the method is the relatively low productivity, which for practical application implies massive parallelization of nozzles.

3. High Capacity Anode Materials for LIBs Designed by SP

High capacity anode materials are attractive candidates to replace current graphite anodes for LIBs. During lithiation-delithiation of these high capacity materials, large volume changes often occur (except some carbonaceous materials), which destroy electrode integrity and cause instability of the solid electrolyte interphase (SEI), resulting in capacity degradation and cell failure. To achieve satisfactory electrochemical performance for high capacity anode materials, electrodes must have the ability to accommodate the volume changes and mitigate the volume change-induced devastating effects on the electrochemical performance. SP has been employed frequently to produce high capacity anode materials with desired nanostructures, which can alleviate the volume changes and lead to stable cycling performance and fast rate capability. In the following text, we will summarize the recent progress on

high capacity anode materials for LIBs prepared by SP. The unique nanostructures generated by SP along with the formation mechanisms will be discussed and the roles these nanostructures played on the electrochemical performance of anode materials will be discussed and emphasized.

3.1. Carbonaceous Anode Materials Prepared by SP

Various forms of carbon, for instance, carbon nanotubes,[62] porous carbon nanospheres,[63,64] carbon nanofibers,[65] etc., have been prepared through SP. Some SP-generated carbonaceous anode materials presented superior lithium storage capacities over graphite anode.[66,67]

Doi et al.[65] prepared graphited carbon nanofibers as an anode for LIBs by using electrostatic SP at a temperature as low as 673 K. Carbon nanofibers with diameters in the range of 100–300 nm were obtained. Layered structure parallel to the fiber axis was found at the surface of the fibers. It was quite surprising that graphited carbon can be synthesized at such a low temperature. The authors speculated that graphitization was enhanced by the fine droplets generated by electrospray. These carbon fibers demonstrated comparable reversible lithium storage capacity as graphite but a larger irreversible capacity during the 1st cycle.

Recently, hollow carbon cages (HCCs) were developed by a spray drying process followed by catalytic graphitization and KOH activation as anodes for high power LIBs.[66] The HCCs had a porous structure with nickel nanoparticles embedded in the cage walls (**Figure 7**a–d). These nickel nanoparticles played a role of catalysis for low-temperature graphitization and also improved the electrical conductivity. The HCCs anode was shown to deliver a high reversible capacity of 1135 mA h g^{-1} at 50 mA g^{-1} and exhibited no capacity decay over 100 cycles at 500 mA g^{-1}. Under a high current density of 15 A g^{-1}, the HCCs anode still provided a capacity of 163 mA h g^{-1}, indicating its fast rate capability. The excellent electrochemical performance
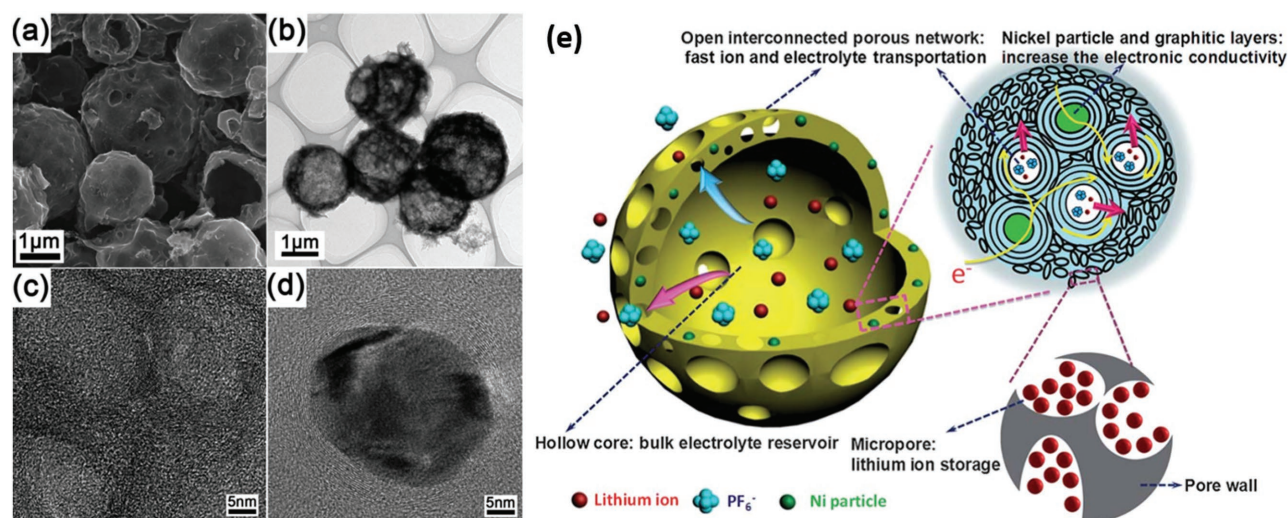

Figure 7. a) SEM and b) TEM images of hollow carbon cages (HCCs) produced from 20 wt% KOH solution. HRTEM images of c) graphitic mesoporous structure and d) nickel nanoparticle encapsulated by graphitic layers. e) A schematic illustration of one HCC, and electrolyte/electron/Li ions transport in the HCC. Reproduced with permission.[66] Copyright 2012, Royal Society of Chemistry.
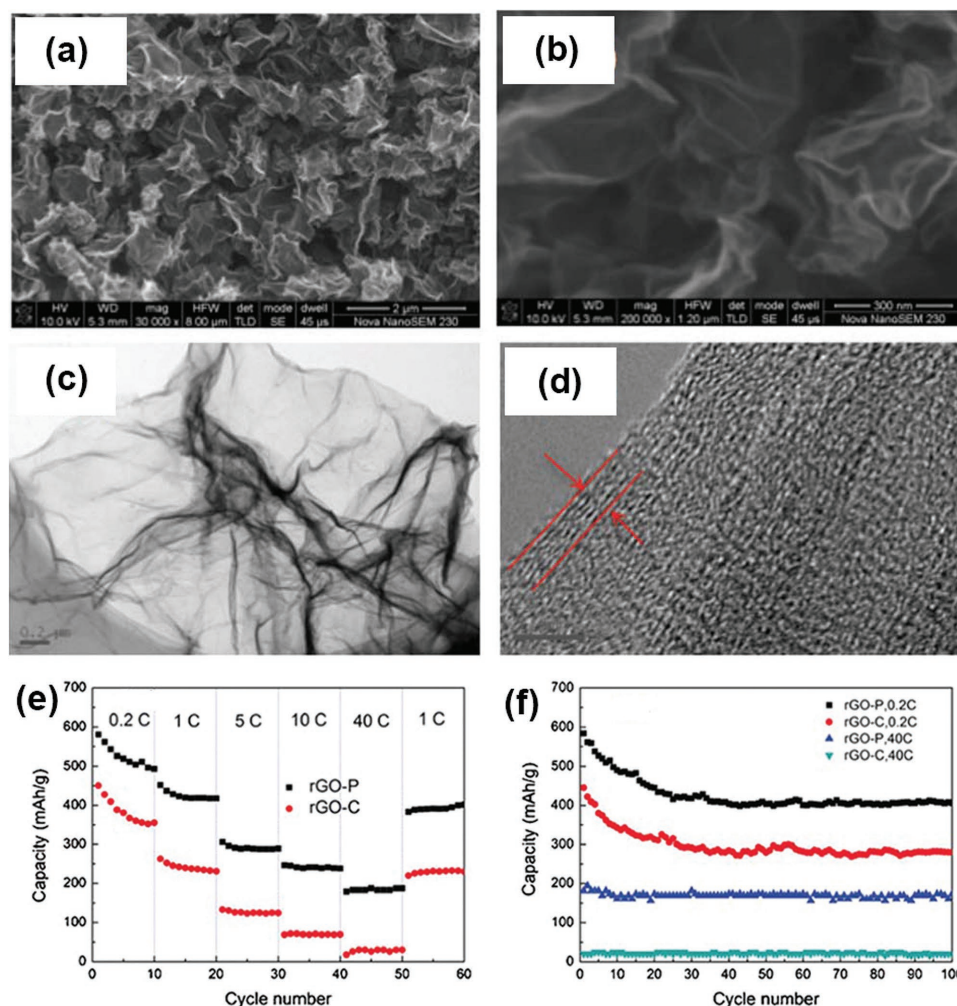
ADVANCED
ENERGY
MATERIALS
www.advenergymat.de

ADVANCED
SCIENCE NEWS
www.advancedsciencenews.com

REVIEW

Figure 8. a,b) SEM images of partially reduced graphene oxide prepared from SP at 500 °C (PrGO-500). c) TEM and d) HRTEM images of PrGO-500. e) Rate capability tests and f) cycling performance of reduced graphene oxide produced from annealing PrGO-500 at 1000 °C (rGO-P) and reduced graphene oxide produced from chemical reduction of PrGO-500 (rGO-C) anodes. Reproduced with permission.[67] Copyright 2013, Royal Society of Chemistry.

of the HCCs anode was ascribed to the hollow porous structure facilitating electrolyte wetting and the improved electrical conductivity by nickel nanoparticles and graphilitic layers (Figure 7e).

Due to its high surface area, excellent electronic conductivity, and large lithium storage capacity over graphite, graphene was frequently explored as anodes for LIBs.[68–73] Very recently, Yang et al.[67] reported a way to efficiently synthesize graphene-based powder for LIBs via in situ SP. Graphene oxide (GO) was first prepared according to a modified Hummer's method, and then partially reduced GO (PrGO) was produced by SP of GO aqueous dispersion, which prevented the aggregating and restacking of GO due to the rapid water evaporation in SP. It was found that the morphology of the PrGO was dependent on the processing temperature of SP. PrGO prepared from SP at 500 °C (PrGO-500) showed a spitball-like structures with the lowest aggregation degree (**Figure 8**a–d). The PrGO-500 was then annealed at 1000 °C to produce reduced graphene oxide (rGO) and the lithium storage ability of this rGO (rGO-P) was

tested and compared with rGO obtained from chemical reduction (rGO-C). Electrochemical tests showed that the reversible lithium storage capacity of rGO-P is much higher than rGO-C under the same C-rates (Figure 8e,f), and the rGO-P is able to deliver a reversible capacity of 180 mA h g^{-1} under a high current density of 40 C. The authors attributed the excellent high-rate capability and cyclability of rGO-P to its unique spitball-like structure, which contained nanometer-thick graphene sheets and flexible spaces, enhancing Li ions transport and ensuring structural integrity.

For carbonaceous anode materials prepared by SP, although higher lithium storage capacities can be achieved compared with graphite, the 1st cycle Coulombic efficiency is often low. This might be caused by the low temperature and insufficient thermal treatment time during pyrolysis, limiting the degree of crystallization and resulting in a large specific surface area of generated carbonaceous materials. Therefore, at current stage, these materials are commercially less competitive compared with graphite counterparts.

ADVANCED
SCIENCE NEWS
www.advancedsciencenews.com

ADVANCED
ENERGY
MATERIALS
www.advenergymat.de

REVIEW

3.2. Alloy Anode Materials Prepared by SP

Alloy anodes (Si, Sn, etc.) are considered as promising anode candidates to replace the current graphite anode mainly because of their very high lithium storage capacities. However, these materials usually undergo significant volume changes during charge-discharge reactions. The repeated volume changes can cause severe electrode structure rearrangements and generate thick, electronically-insulating SEI film between active materials and electrolyte, giving rise to degradation of battery performance. Nanostructured alloys and their composites have shown great potentials to accommodate these volume changes and address the capacity decay. As presented below, SP has found many applications in the preparation of high capacity alloy anodes with great electrochemical performances.

3.2.1. Si Prepared by SP

SP was first introduced by Liu et al. to prepare carbon-coated Si nanocomposites.[74] A precursor solution was prepared by dispersing Si nanoparticles into a citric acid/ethanol solution via ultrasonication. The Si-C nanocomposites were generated by SP of the precursor solution at 400 °C in an air atmosphere. A low temperature of 400 °C effectively prevented the oxidation of Si. A vertical-type SP reactor was used to avoid gravity-induced Si nanoparticles sinking, which was often observed in horizontal-type SP reactors, thus increasing the Si yield in the final composite. The reaction taking place during the pyrolysis can be expressed as following:[74]

$$\text{Si} + \frac{C_6}{H_8}O_7C_2H_6O \rightarrow \frac{Si}{C} + CO_2 \uparrow + H_2O \uparrow + energy \uparrow \qquad (5)$$
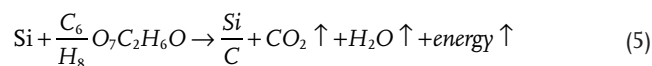
Carbon, generated by thermal decomposition of citric acid, was found to be coated on Si nanoparticles in the SP-generated Si-C nanocomposite. According to the authors, carbon provided a high electronic conductivity, buffered the volume changes, and prevented Si nanoparticles agglomeration.[74] Thus, the carbon-coated Si nanocomposites exhibited better electrochemical performance compared with uncoated nanocrystalline Si in terms of both capacity retention and the 1st cycle Coulombic efficiency. The authors also systematically investigated the effects of pyrolysis temperature[75] and carbon content[76] on the electrochemical performance of carbon-coated Si nanocomposites. Their results showed that composites generated at 400 °C with carbon content above 50 wt% exhibited the best lithium storage performance. Later, Lai et al.[77] introduced flake graphite to the precursor dispersion containing Si nanoparticles and glucose to produce a graphite/Si/carbon composite by spray drying and subsequent pyrolysis. The graphite/Si/carbon composite exhibited a high lithium storage capacity (≈600 mA h g^{-1}).

Lately, Jung et al. developed a spray drying method for large-scale production of high-performance Si-C composite anode (**Figure 9**a),[78] in which primary Si nanoparticles were embedded in porous carbon particles to form highly dense secondary particles. The synthetic method for the Si-C composite mainly involved four steps (Figure 9b). First, a mixed solid-liquid precursor solution consisting of Si nanoparticles

(average diameters ≈70 nm), silica nanoparticles (average diameters ≈10 nm), and sucrose was nebulized into droplets. Second, these droplets were directed into a drying reactor to evaporate water and generate solid-phase Si/silica/sucrose ternary powders with spherical shapes (Figure 9c). With a lab-scale ultrasonic atomizer, a composite productivity of ≈10 g h^{-1} can be achieved, indicating the high efficiency of this method. Third, these solid-phase powders were heated at 700 °C under nitrogen atmosphere to carbonize sucrose. Finally, the carbonized composite was chemically etched by HF acid to remove silica nanoparticles and generate pores (Figure 9d). It was showed that silica was very critical for production of this nanostructured Si-C composite. It functioned both as templates for pore generation and as colloidal seeds for formation of dense and uniform particles.

The porous structure not only accommodated the volume changes of Si nanoparticles but also provided great electronic and ionic conductivities through intimate contacts between Si nanoparticles and carbon matrix and efficient Li ions diffusion in continuous pores. Therefore, the Si-C composite demonstrated excellent capacity retention (≈91% capacity retention after 150 cycles at a current rate of 2 C = 4 A g^{-1}), high Coulombic efficiency (≈99%), and fast rate capability (≈1493 mA h g^{-1} achieved at 10 C = 20 A g^{-1}). It has to be notable that this synthetic method involved multiple steps and environmentally unfriendly HF etching, which could restrict its scale up. However, the current method can be greatly improved by combining the spray drying, carbonization, and HF etching in to a single step where carbonization can be completed during the spray drying step and precipitation agents, which can be decomposed during the heat treatment, can be integrated into the precursor solution.

Due to its unique physical and mechanical properties (e.g., high electronic conductivity and strong mechanical strength), graphene is often used as a carbon source to produce graphene-Si composite as anodes for LIBs. As reported by Luo et al.,[79] crumpled graphene-encapsulated Si nanoparticles were developed as LIB anodes by SP using a precursor solution containing Si nanoparticles (50–100 nm in diameters) dispersed in aqueous dispersion of graphene oxide. As the aerosol droplets passing through a preheated tube furnace, evaporation-induced capillary force caused graphene sheets (5–10 nm thickness corresponding to about 15–30 layers of graphene) to wrap around Si nanoparticles. The highly crumpled graphene shell accommodated the repeated volume changes of encapsulated Si nanoparticles and protected Si nanoparticles from forming SEI film on their surfaces. Compared with bare Si nanoparticles, the crumpled graphene-encapsulated Si nanoparticles showed much better electrochemical performance towards lithium storage in terms of Coulombic efficiency, cycling stability, and rate capability. However, due to the aggregation of Si nanoparticles during the SP process, some Si nanoparticles inside the graphene sheets may have poor electrical contact with graphene. As a result, the specific delithiation capacity provided solely by Si was only 1775 mA h g^{-1}, indicating a low utilization of Si (≈42.3%). To alleviate the aggregation of Si nanoparticles during the SP process, a similar graphene-wrapped Si nanoparticles composite was also developed by our group (**Figure 10**ab).[80] In contrast with Luo et al.'s work, in our work,

ADVANCED
ENERGY
MATERIALS
www.advenergymat.de

ADVANCED
SCIENCE NEWS
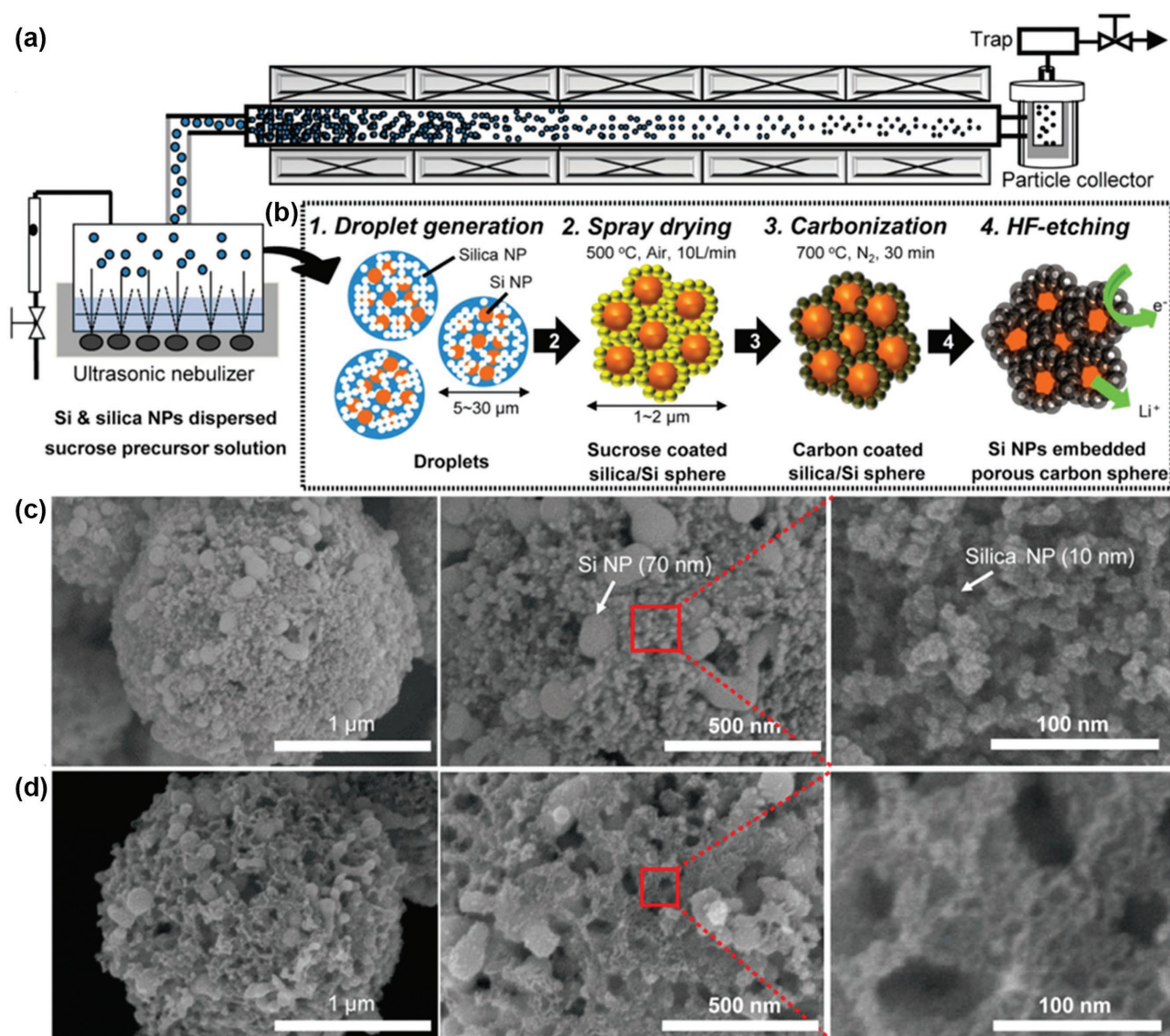www.advancedsciencenews.com

REVIEW

Figure 9. a) A schematic illustration of ultrasonic spray drying process. b) A schematic illustration of synthesis of Si nanoparticles embedded in porous carbon spheres. c) SEM images of sucrose/silica/Si composite spheres generated by the spray drying process. d) SEM images of the final Si-porous carbon composite spheres. Reproduced with permission.[78] Copyright 2013, American Chemical Society.

Si nanoparticles were functionalized by aminoprupyltrimethoxysilane (APS) which has a structure with a trimethoxysilane group on one end and an amino group on the other. The trimethoxysilane groups could react with SiO_2 on Si surface and amino groups were able to interact with the carboxylic group on graphene oxide to create strong bonds between Si nanoparticles and graphene oxides. The functional groups on APS provided steric hindrance between Si nanoparticles thus avoiding aggregation of Si nanoparticles, as demonstrated by the TEM images and energy dispersive X-ray spectroscopy (EDS) elemental mapping which showed that Si nanoparticles were separated from each other inside the graphene shell (Figure 10c–e). Therefore, for the APS functionalized Si-graphene composite, Si delivered a specific delithiation capacity of 2422 mA h g^{-1}, much higher than the one provided by unfunctionalized Si-graphene composite ($\approx$1775 mA h g^{-1}),[79] suggesting that the APS enhanced

the utilization of Si nanoparticles inside the graphene shell. Strictly speaking, the fabrication of aforementioned two graphene-Si composites should be termed as spray drying, since the spray process only involved physical processes rather than any chemical changes. Besides these Si-C composites, a core-shell composite consisting of Si and silicon oxycarbide (SiOC) was also recently reported.[81] The SiOC shell layer has some reactivity with lithium ions so that it expands to a certain level during lithiation and maintains the integration with the Si core during the volume expansion, leading to the conspicuously improved electrochemical performance compared with a carbon-coated Si control sample.

In contrast with the studies discussed thus far which used solid crystalline Si nanoparticles as Si sources and organic compounds as carbon sources, Yang et al.[82] applied a single component, i.e., organo silane ($\approx$dimthyldivinylsilane), to

ADVANCED
SCIENCE NEWS
www.advancedsciencenews.com

ADVANCED
ENERGY
MATERIALS
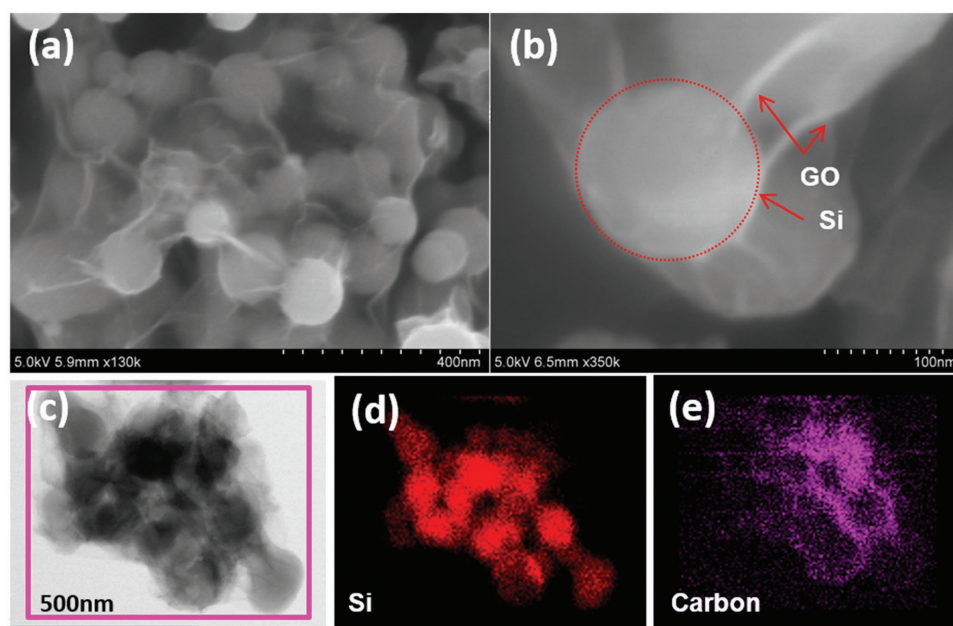www.advenergymat.de

REVIEW

Figure 10. a,b) SEM images of aminoprupyltrimethoxysilane (APS) functionalized Si-graphene composite. c) Bright field TEM image of APS functionalized Si-graphene composite. EDS elemental mapping for d) Si and e) carbon in (c). Reproduced with permission.[80] Copyright 2013, Wiley-VCH.

simultaneously generate both carbon and Si by SP. This approach allowed a very homogeneous dispersion of Si in carbon. The synthesized Si was amorphous nanoparticles uniformly embedded in the carbon matrix to a scale of 2–3 nm. Compared to crystalline Si, amorphous Si possesses higher fracture strength and experiences isotropic stresses/strains during volume changes, which could lead to enhanced electrochemical performance. This amorphous Si-C composite demonstrated stable cycling performance over 150 cycles with excellent Coulombic efficiency.

On the whole, Si composites prepared by SP generally possess structures in which Si nanoparticles embedded in or wrapped by electrically conductive materials. These composites exhibit enhanced lithium storage performances over pristine Si nanoparticles. One challenge of preparing Si composites by SP is that appropriate precursor solutions, in which low-cost Si-containing salts and solvent can be mixed at the atomic-scale, are very scarce. The precursor solutions used for SP process usually are aqueous suspensions consisting of dispersed crystalline Si nanoparticles and dissolved/dispersed carbon sources. During SP process, Si nanoparticles may agglomerate, and as a result, some nanoparticles may have limited electrical contact with conductive materials. Another issue caused by Si nanoparticles aggregation is that spray nozzles may be clogged after long processing time, lowering the production efficiency. One possible solution to alleviate the aggregation issue is to use functionalized Si nanoparticles as demonstrated in our previous work.[80]

3.2.2. Sn Prepared by SP

Sn anodes face the similar volume change problem as Si anodes. Sn anodes are usually prepared as composites in which

fine Sn particles are uniformly dispersed in a conductive matrix. Small Sn particles can reduce the mechanical stress generated from large absolute volume changes.[83] The matrix can buffer the volume fluctuation during charge-discharge and function as a barrier against Sn aggregation to form large clusters. Different from Si, the low melting point of Sn restricts application of many high temperature synthetic methods in fabricating Sn and Sn composites since Sn easily aggregates into large grains during high temperature heat treatment. SP is an ideal method to overcome this limitation due to the very short residence time (less than few seconds) of aerosol droplets in the hot zone (i.e., tube furnace) and subsequent rapid cooling, which allows rapid formation of small Sn particles and freezes the structure.

Nanosized Sn and Sn-Co alloy with uniform particle size distributions were prepared by Valvo et al.[84] through a so-called electrostatic spray reductive precipitation technique, which combined electrostatic spray with reductive precipitation method. Sn was obtained by reducing sprayed droplets containing $SnCl_2 \cdot 2H_2O$ with $NaBH_4$ in organic solvents. The electrochemical tests showed that lithium storage in Sn-Co alloy exhibited a fast capacity fading, which was ascribed to the oxidation of nanoparticles during post washing and collection procedures. Again, this electrostatic spray reductive precipitation method cannot be considered as SP in a real sense since no pyrolysis was involved in the process. A Sn-Ni composite was also prepared as an anode for LIBs by SP.[85] Similar to the Sn-Co composite, the Sn-Ni composite also exhibited fast capacity fading.

Compared with the heavy metal matrix (e.g., Co,[84] Ni[85]) which lowers the overall storage capacity of composites, carbon is a better choice as the matrix, because it is lighter and can simultaneously enhance the mechanical properties and electronic conductivity of the composites. The first SP-generated Sn-C composite was prepared by Zheng et al.[86] A series of
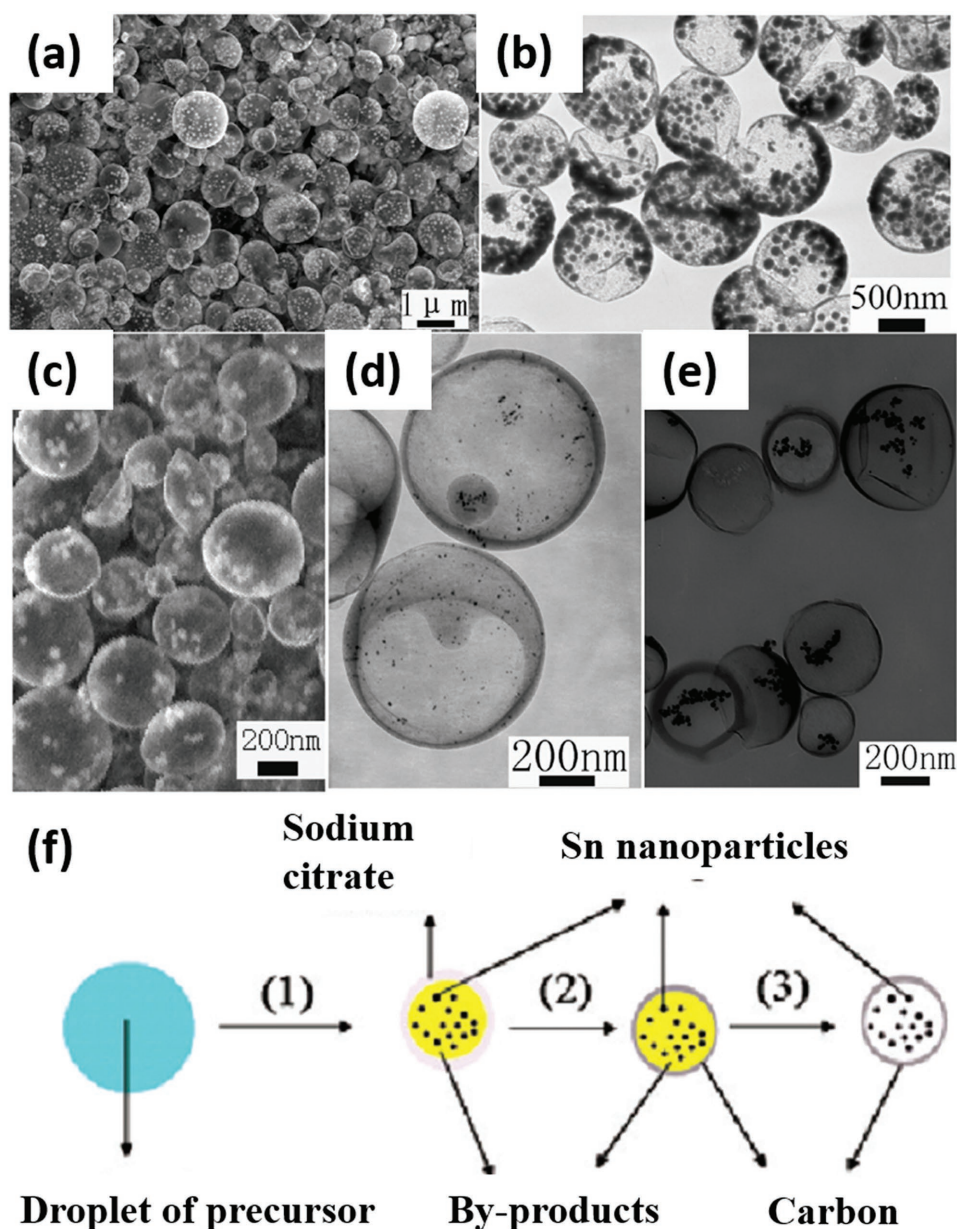
ADVANCED
ENERGY
MATERIALS
www.advenergymat.de

ADVANCED
SCIENCE NEWS
www.advancedsciencenews.com

Figure 11. SEM and TEM images a,b)of Sn@carbon, c) Fe-FeO@carbon, d) Pt@carbon, and e) Ag@carbon obtained from SP. f) A schematic illustration of formation mechanisms for metal@carbon obtained from SP of aqueous solutions containing metal salts and sodium citrate. Reproduced with permission.[86] Copyright 2009, American Chemical Society.

rattle-type hollow carbon spheres (i.e., carbon shell with a solid particle core and empty space in between), including Sn@carbon, Pt@carbon, Ag@carbon, and Fe-FeO@carbon (**Figure 11**a–e), were synthesized by ultrasonic SP employing aqueous solutions consisting of corresponding metal salts and sodium citrate.[86] The mechanism involved in the synthesis procedure is illustrated in Figure 11f. As the droplets passed through the tube furnace, metal nanoparticles were first produced from the reduction of metal salts by sodium citrate. Then, sodium citrate migrated to the periphery of the liquid droplets and was carbonized to form the carbon shell. Finally, after removing the water-soluble byproducts (e.g., NaCl, Na_2CO_3, etc.), rattle-type metal@carbon was formed. Benefiting

from the unique nanostructure of rattle-type Sn@C which provided hollow space to accommodate the volume changes and prevented Sn nanoparticles aggregation in different Sn@C particles, the composite exhibited excellent cycling performance towards Li ions storage ($\approx$460 mA h g^{-1} after 95 cycles at a current density of 0.55 mA cm^{-2}). However, the large hollow space inside carbon shell inevitably reduced the volumetric capacity.

Recently, our group reported a nano-Sn/C composite by SP using a precursor solution containing $SnCl_2$ and polyvinylpyrrolidone (PVP) dissolved in ethanol.[87] Thermal decomposition of $SnCl_2$ and carbonization of PVP yielded a nano-Sn/C composite, in which fine Sn particles with a diameter of 10 nm were uniformly dispersed in spherical carbon matrix
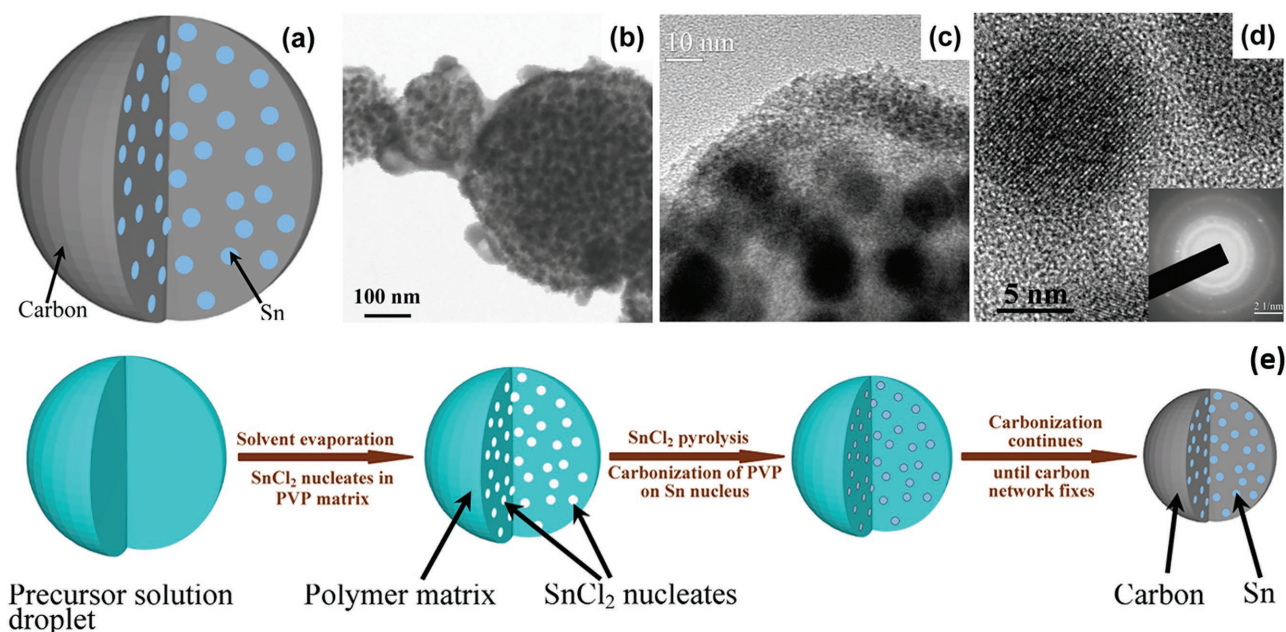
ADVANCED
SCIENCE NEWS
www.advancedsciencenews.com

ADVANCED
ENERGY
MATERIALS
www.advenergymat.de

REVIEW

Figure 12. a) Schematic diagram, b) TEM image, and c,d) HRTEM images of the ultrasmall nano-Sn/C composite particles. e) A schematic illustration of formation process of ultrasmall nano-Sn dispersed in carbon sphere. Inset of (d) is the selected area electron diffraction pattern. Reproduced with permission.[87] Copyright 2013, American Chemical Society.

(**Figure 12**a–d). The formation mechanism of nano-Sn/C composite is schematically illustrated in Figure 12e. During the pyrolysis process under a reductive atmosphere, $SnCl_2$ was first decomposed to Sn grains, which then functioned as catalysts to promote the formation of carbon. Although carbonization of PVP required a higher temperature than the melting point of Sn, the pyrolysis-generated carbon along with the short residence time ($\approx$1s) in the hot zone limited the growth of Sn grains, producing ultra-small Sn particles. Density measurements by the tandem differential mobility-aerosol particle mass analysis (DMA-APM) suggested that the nano-Sn/C composite possessed a porous structure, providing free space to accommodate the volume changes during lithiation-delithiation. Electrochemical tests demonstrated that the nano-Sn/C composite could deliver a reversible capacity of 710 mA h g^{-1} with no capacity fading for 130 lithiation-delithiation cycles. More importantly, excellent rate capability was achieved by the composite which can stand a delithiation rate as high as 20 C ($\approx$15 A g^{-1}) without significant capacity loss. The exceptional electrochemical performance of the nano-Sn/C composite should be attributed to three unique features of the composite, which were exclusive outcomes of SP. First, the ultra-small Sn nanoparticles reduced the absolute strain during lithiation-delithiation. Second, the porous carbon frame effectively accommodated the volume changes and prevented Sn aggregation during cycling. Finally, the uniformity of Sn in the carbon matrix guaranteed a balanced stress over the whole composite particles and maintained the mechanical integrity of the composite electrode. A similar Sn/C composite was also prepared by Guo et al. through SP.[88] A tri-block copolymer of poly(ethylene glycol)-block-poly(propylene glycol)-block-poly(ethylene glycol) (Pluronic F127, PEO106-PPO70-PEO106) was added to the precursor solution to function as a regulating agent for producing small particles. With the help of the polymetric surfactant, a Sn/C composite with a hierarchical structure was obtained. However, thermal decomposition of PEO106-PPO70-PEO106 caused Sn oxidation. Due to the existence of SnO_2, the 1st cycle Coulombic efficiency of the hierarchical Sn/C composite was only 30%, limiting the practical application of this composite.

To sum up, SP is a good technique to produce Sn-C composites anode materials with nanosized Sn uniformly dispersed in carbon buffering matrix because the short residence time of Sn in the hot zone and fast cooling step prevent melting and coalescence of Sn. In addition, the concurrently formed carbon along with Sn nanoparticles further restricts growth of Sn grains.

3.3. Metal Oxides Anode Materials Prepared by SP

Metal oxides were considered as anodes for LIBs mainly due to their high capacities (except $Li_4Ti_5O_{12}$), low cost, natural abundance, and environmental benignity. However, pristine metal oxides usually have a low electronic conductivity and thus electronically-conductive additives (for example carbon) were often required to enhance the electrochemical performances. Due to the reduction of metal oxides by carbon at high temperatures, high temperature carbon coating methods cannot typically be employed. SP has been found as an efficient synthetic method to produce metal oxides-carbon composites due to the very short reaction time for carbon formation during the pyrolysis, effectively avoiding the reduction of metal oxides to metals. As presented in the following text, a large number of articles regarding SP and metal oxides anodes for LIBs can be found in the literature.

ADVANCED
ENERGY
MATERIALS

www.advenergymat.de

ADVANCED
SCIENCE NEWS

www.advancedsciencenews.com

REVIEW

3.3.1. $Li_4Ti_5O_{12}$ Prepared by SP

$Li_4Ti_5O_{12}$ was used as anodes for LIBs due to its compatibility with the electrolyte (i.e., no SEI formation), excellent cycling performance, and safety advantage over graphite anode. However, pristine $Li_4Ti_5O_{12}$ often showed poor high rate performance because of its low electronic conductivity ($\approx 10^{-13}$ S cm^{-1}) and lithium ion diffusivity (10^{-9}–10^{-16} cm^2 s^{-1}).[89] $Li_4Ti_5O_{12}$ was usually prepared as nanosized particles with doping or surface coating to increase its electronic conductivity.

SP was first introduced by Doi et al.[90] to prepare nanosized $Li_4Ti_5O_{12}$. $Li_4Ti_5O_{12}$ nanoparticles with a fairly uniform diameter of 12 nm (**Figure 13**a,b) were deposited on Pt by electrospray pyrolysis of a precursor solution of 2-propanol containing $Ti(OC_3H_7)_4$ and $Li(CH_3COO)$. The excellent uniformity of $Li_4Ti_5O_{12}$ was benefited from the narrow size distribution of droplets created by electrostatic atomization. Cyclic voltammetry test of $Li_4Ti_5O_{12}$ in lithium batteries presented very sharp and symmetrical redox peaks with small peak separation between cathodic peak and anodic peak, indicating enhanced diffusion process by using uniform nanosized particles.[90] Ju et al. prepared $Li_4Ti_5O_{12}$ by post annealing the precursor powders synthesized by ultrasonic SP.[91–93] Since the as-sprayed powders did not consist of any crystalline $Li_4Ti_5O_{12}$ because of the short residence time of the droplets inside the hot wall furnace, post-treatment was required to achieve crystalline $Li_4Ti_5O_{12}$. Galvanostatic charge-discharge tests of $Li_4Ti_5O_{12}$ in lithium cells indicated that $Li_4Ti_5O_{12}$ obtained at the post-treatment temperature of 800 °C demonstrated the highest initial lithium storage capacity.[91] The authors also systematically investigated the effect of preparation conditions (e.g., tube furnace temperature, carrier gas flow rate, precursor concentration, etc.) on the morphology and electrochemical performance of $Li_4Ti_5O_{12}$.[92] The results suggested that tube furnace with an intermediate temperature (≈ 800 °C) and precursor solution with a high salt concentration (above 0.5 M) would result in $Li_4Ti_5O_{12}$ with the best cycling performance. The carrier gas flow rate was found not to impact the electrochemical performance of $Li_4Ti_5O_{12}$ prepared by SP. Later, a drying control additive (Dimethylacetamide, DMA) and ethylene glycol (EG) were introduced into the aqueous precursor solution to control the morphology of as-sprayed powders.[93] The obtained $Li_4Ti_5O_{12}$ from precursor solutions with organic additives demonstrated a higher lithium storage capacity than the one prepared from the additive-free precursor solutions.

Due to its low electronic conductivity ($\approx 10^{-13}$ S cm^{-1}), $Li_4Ti_5O_{12}$ was often mixed with carbonaceous materials to improve its electrochemical properties. Recently, a $Li_4Ti_5O_{12}$/reduced graphene oxide composite was synthesized by spray-drying and annealing processes as high rate anodes for LIBs.[94] First, aqueous dispersion containing $Li_4Ti_5O_{12}$ and graphene oxide was spray-dried to obtain a $Li_4Ti_5O_{12}$/graphene oxide (GO) composite. Then, post-annealing process was applied to remove the residue groups on GO thus increasing the conductivity of 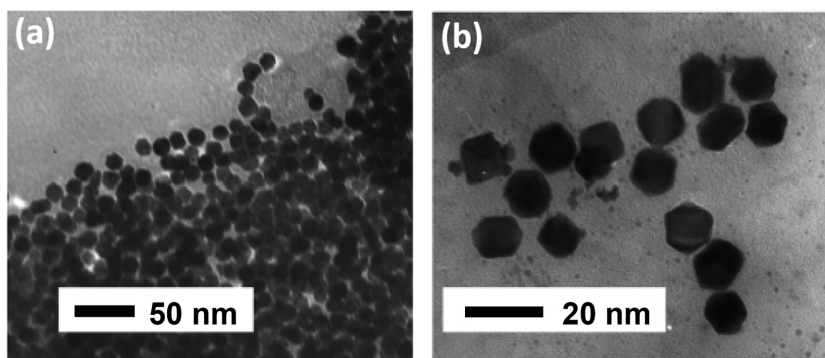the composite. The composite possessed a structure with submicron $Li_4Ti_5O_{12}$ particles covered by reduced GO sheets. The $Li_4Ti_5O_{12}$/reduced GO composite demonstrated a much-improved rate capacity compared with pristine $Li_4Ti_5O_{12}$, due to the enhanced electrical conductivity by reduced GO.

Figure 13. a,b) TEM images of nanosized $Li_4Ti_5O_{12}$ prepared at 673 K by electrospray pyrolysis. Reproduced with permission.[90] Copyright 2005, American Chemical Society.

3.3.2. Iron Oxides Prepared by SP

Iron oxides (Fe_2O_3 and Fe_3O_4) have been proposed as potential anode candidates due to their high lithium storage capacities, low cost, natural abundance, and environmental benignity. The theoretical lithium storage capacity can reach 1007 mA h g^{-1} for Fe_2O_3 and 926 mA h g^{-1} for Fe_3O_4. However, the cycling performance of pristine iron oxides was usually very poor mainly because of their low conductivity, large volume changes ($\approx 92.8\%$ for Fe_2O_3 and 88.1% for Fe_3O_4 upon full lithiation) during charge-discharge, and Fe^0 particle aggregation upon cycling. To circumvent these limits, conductive additives were often added into iron oxides to improve their conductivity and hollow-/nano-structures were designed to accommodate the volume changes and reduce the ions transport length.

A hollow-structured α-Fe_2O_3/carbon (HIOC) nanocomposite was fabricated by SP in one step.[95] An organic iron salt, iron lactate, was chosen as the iron precursor due to its large weight loss upon decomposition ($\approx 76\%$), which could result into much more porous structures than the samples prepared from other inorganic iron salts precursors. As a result, this HIOC nanocomposite possessed a very high specific surface area of 260 m^2 g^{-1} with a hierarchical hollow sphere-like structure in which α-Fe_2O_3 nanocrystals (≈ 10 nm in diameter) were surrounded by amorphous carbon. By changing the SP parameters, both the α-Fe_2O_3 crystal size and specific area of the nanocomposite can be easily tuned (**Figure 14**a). The electrochemical characterizations indicated that HIOC exhibited a more stable cycling performance than hollow-structured α-Fe_2O_3 (HIO) (Figure 14c), suggesting that carbon played a critical role in stabilizing lithium storage in α-Fe_2O_3. Owing to its hollow structure and high specific surface area, HIOC with 14.7 wt% carbon showed a high capacity (≈ 1210 mA h g^{-1} at 0.1 C) and good cycling stability (720 mA h g^{-1} up to 220 cycles at a current density of 2 C) towards lithium storage. However, the tap density of the HIOC was only 0.1 g cm^{-3} which would result in a very low volumetric capacity. To improve the tap density, a
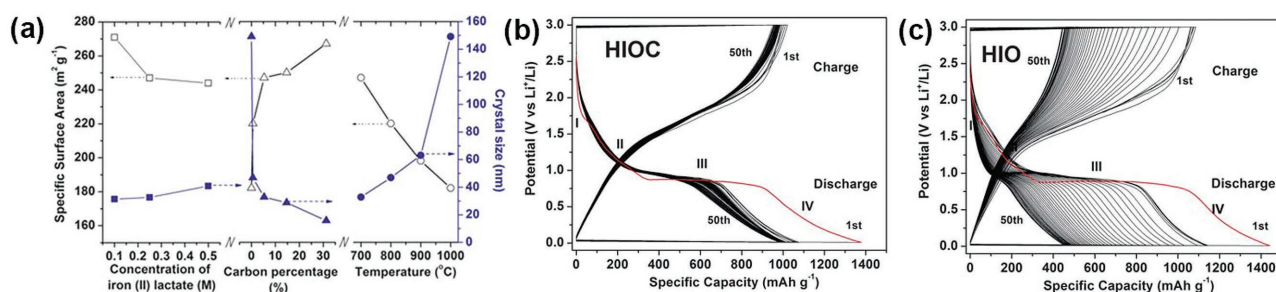
Figure 14. a) The surface areas and crystal sizes as functions of the concentration of iron lactate, the carbon percentage, and the SP temperature. Lithiation-delithiation curves of b) hollow-structured α-Fe$_2$O$_3$/carbon (HIOC) and c) hollow-structured α-Fe$_2$O$_3$ (HIO). The current densities were 50 mA g^{-1} for the first five cycles. Reproduced with permission.[95] Copyright 2010, Royal Society of Chemistry.

hollow α-Fe$_2$O$_3$ nanosphere/carbon nanotube (CNT) composite was prepared via SP by the same group.[96] Nanosized droplets were formed on the surface of CNTs due to the super-hydrophobicity of CNT surface. These nanosized droplets were further dried and decomposed to form hollow α-Fe$_2$O$_3$ nanospheres. Owing to the enhanced electrical conductivity by CNTs, the hollow α-Fe$_2$O$_3$ nanosphere/CNT composite presented a good high-rate capability in lithium cells with a capacity of 350 mA h g^{-1} can be reached under a current density of 6.4 A g^{-1}.

A nanostructured Fe$_2$O$_3$ composite electrode was prepared by electrostatic SP using a precursor solution containing iron salt and polyvinylidene fluoride (PVdF) dissolved in N-methylpyrrolidone (NMP).[97] The electrode was directly fabricated by combining material synthesis and electrode preparation into a single step. However, the cycling performance of Fe$_2$O$_3$ composite electrode was unsatisfactory, which needs further improvement.

Recently, yolk-shell structured Fe$_2$O$_3$ particles were synthesized from continuous SP of an aqueous precursor solution consisting of iron nitrate and sucrose.[98] The number of shell was found to be dependent on the pyrolysis temperature, higher temperatures leading to Fe$_2$O$_3$ yolk-shell particles with less layer of shell. The Fe$_2$O$_3$ yolk-shell particles synthesized at 600 °C, 800 °C, and 1000 °C possessed four, three, and two shells, respectively (**Figure 15**a–i). It was revealed that sucrose played a key role in the formation of the yolk-shell structure since the Fe$_2$O$_3$ prepared without sucrose in the precursor solution exhibited a dense and nonporous structure. Since the void space in the yolk-shell structured Fe$_2$O$_3$ accommodated volume changes of Fe$_2$O$_3$ during lithiation-delithiation, the Fe$_2$O$_3$ yolk-shell particles presented a higher capacity and faster rate capability than dense Fe$_2$O$_3$ particles (Figure 15j,k).

Our group has reported mesoporous Fe$_2$O$_3$ prepared by SP as anodes for LIBs.[99] Although the same precursor solution was used by Son et al.[98] and by us, instead of the yolk-shell structure, we obtained Fe$_2$O$_3$ particles with a mesoporous structure. This might be due to the shorter residence time used in our study (1 s in our study vs 7 s in Ref. [98]). Quick thermal decomposition of iron nitrate and sucrose generated gases, resulting in the porous structure. By changing the pyrolysis temperature, both crystalline Fe$_2$O$_3$ (C-Fe$_2$O$_3$) and amorphous Fe$_2$O$_3$ (A-Fe$_2$O$_3$) were achieved (**Figure 16**a–d). Post mortem TEM studies showed that the mesoporous structure was converted to nano-crystallite structure for both C-Fe$_2$O$_3$ and A-Fe$_2$O$_3$. Both C-Fe$_2$O$_3$ and A-Fe$_2$O$_3$ exhibited better electrochemical

performances towards lithium storage than commercial Fe$_2$O$_3$ (Figure 16e). The C-Fe$_2$O$_3$ demonstrated stable cyclability over 300 lithiation-delithiation cycles (Figure 16f), which was ascribed to the interior voids buffering volume changes of Fe$_2$O$_3$ and small size of Fe$_2$O$_3$ reducing Li-ion diffusion distance.

Besides Fe$_2$O$_3$, Fe$_3$O$_4$ was also reported as anodes for LIBs. Recently, Choi et al. applied SP to prepare Fe$_3$O$_4$-decorated hollow graphene balls as anodes for LIBs.[100] The precursor solution was prepared by dissolving FeCl$_3$ into a stable graphene oxide colloidal solution. In the Fe$_3$O$_4$-decorated hollow graphene balls, graphene formed a hollow ball-like particle with ultrafine Fe$_3$O$_4$ particles (less than 15 nm in diameter) uniformly distributed on the inner surface of wrinkled graphene shell (**Figure 17**a–g). Thanks to the unique structure of Fe$_3$O$_4$-decorated hollow graphene balls, this composite could withstand 1000 lithiation-delithiation cycles with a lithiation capacity of 690 mA h g^{-1} retained after the 1000th cycle (Figure 17h). Even under a current density of 30 A g^{-1}, Fe$_3$O$_4$-decorated hollow graphene balls still delivered a lithiation capacity of 540 mA h g^{-1}. Indeed, the Fe$_3$O$_4$-decorated graphene balls obtained from SP demonstrated superior cyclability and rate capability than Fe$_3$O$_4$-graphene composites prepared by any other synthetic methods,[100] indicating the powerfulness of SP on fabrication of iron oxides-graphene composites.

3.3.3. Cobalt Oxides Prepared by SP

In this section, we will review the recent progress on cobalt oxides anodes prepared by SP. Needham et al. first used SP method to synthesize a Co$_3$O$_4$-C composite as anode materials for LIBs.[101] The Co$_3$O$_4$-C composite was prepared via spraying aqueous solution containing cobalt nitrate and sucrose under an air atmosphere in a preheated tube furnace. Crystalline Co$_3$O$_4$ with cubic structure was obtained after the SP. The composite consisted of both partially and fully developed hollow spheres, and a majority of them were less than 5 μm in diameter and had an average wall thickness of 0.5–2 μm. TEM analyses showed that each hollow particle was composed of few aggregated sub-micrometer Co$_3$O$_4$-C particles, in which disordered carbon and crystalline Co$_3$O$_4$ domains were finely distributed, coated by a carbon sheath with a thickness of 2–5 nm. Electrochemical tests showed that Co$_3$O$_4$-C composite exhibited better capacity retention than bare Co$_3$O$_4$ with a specific capacity >800 mA h g^{-1} obtained after 50 cycles. It was explained by the
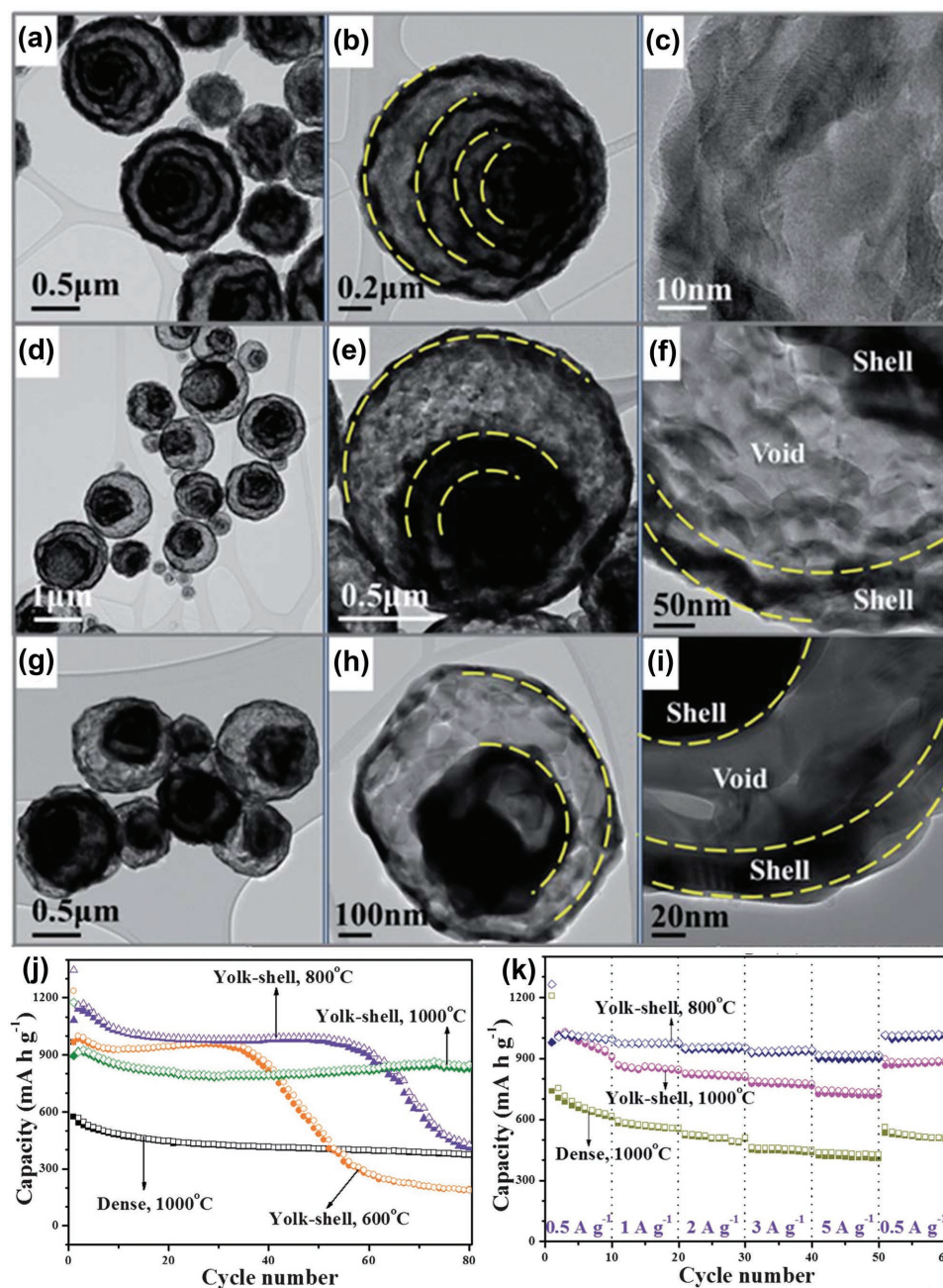
Figure 15. TEM images of Fe$_2$O$_3$ particles prepared by SP at various temperatures: a–c) 600 °C, d–f) 800 °C, and g–i) 1000 °C. j) Cycling performance of various Fe$_2$O$_3$ at 300 mA g^{-1}. k) Rate performance of various forms of Fe$_2$O$_3$. Reproduced with permission.[98] Copyright 2013, Royal Society of Chemistry.

authors that carbon coating avoided the continuous decomposition of electrolyte, improved the electrical conductivity, and buffered the volume changes during cycling.

Very recently, mesoporous Co$_3$O$_4$ nanosheets were reported as anodes for LIBs by Son et al.[102] The Co$_3$O$_4$ nanosheets were prepared by spray drying aqueous solution comprising cobalt nitrate and citric acid followed by a post heat treatment process (**Figure 18**). Citric acid functioned as a chelating agent which chelated Co salts during the drying process. The as-prepared Co$_3$O$_4$ was amorphous, and post-treatment was

applied to crystallize the materials. If the post-treatment temperature was lower than 600 °C, the obtained Co$_3$O$_4$ presented as a mesoporous nanosheet morphology in which nanoparticles were connected with each other to form a sheet-like aggregate (Figure 18). Further increasing the post-treatment temperature to above 600 °C, the nanosheet morphology was destroyed and particle growth was observed (Figure 18). Electrochemical characterizations showed that Co$_3$O$_4$ nanosheets prepared under low post-treatment temperatures demonstrated an enhanced lithium storage capacity than Co$_3$O$_4$ nanoparticles synthesized
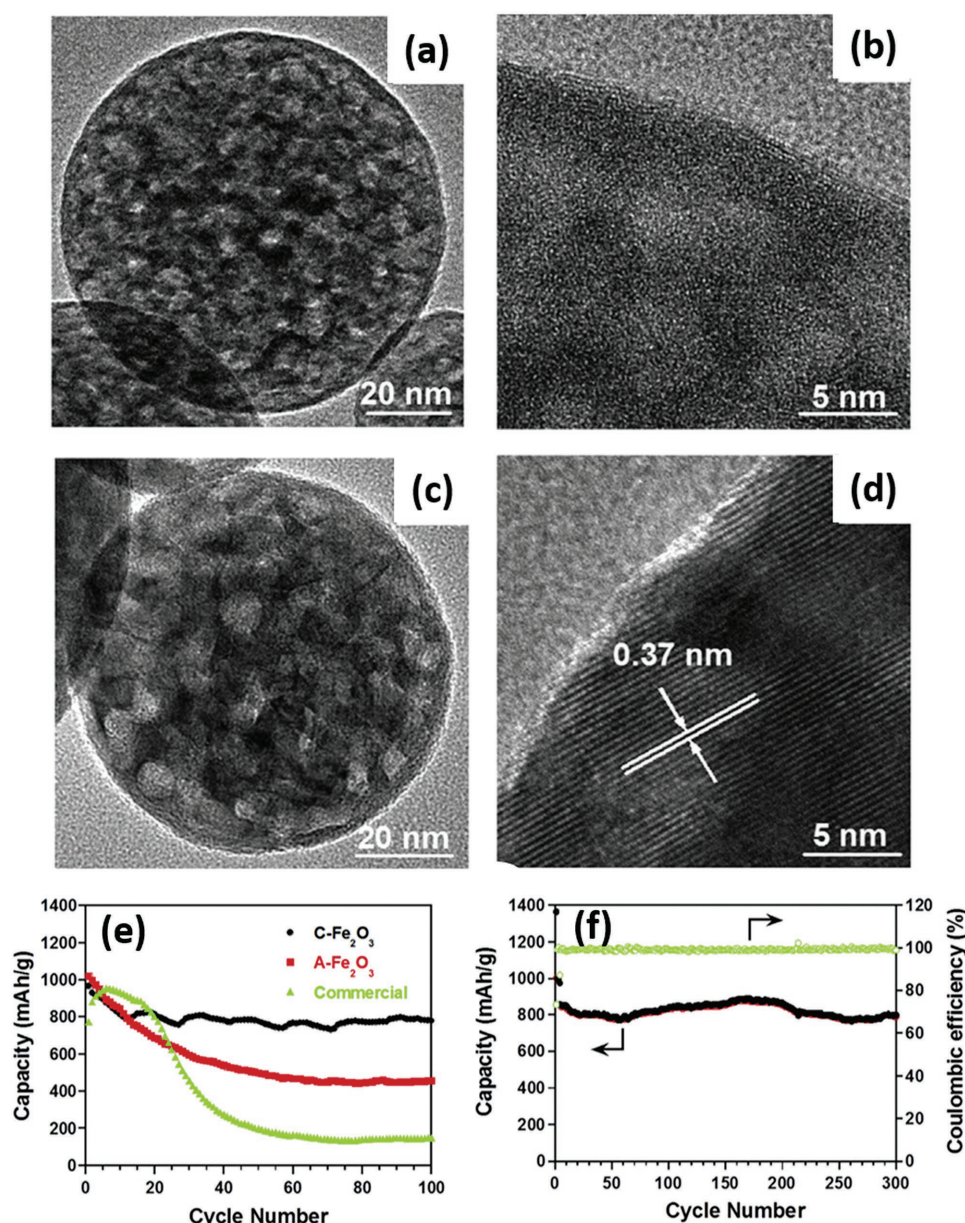
**ADVANCED
SCIENCE NEWS**

www.advancedsciencenews.com

**ADVANCED
ENERGY
MATERIALS**

www.advenergymat.de

REVIEW

Figure 16. TEM and HRTEM images for a,b) amorphous Fe_2O_3 (A-Fe_2O_3), and c,d) crystalline Fe_2O_3 (C-Fe_2O_3). e) Comparison of cycling performance of C-Fe_2O_3, A-Fe_2O_3 and commercial Fe_2O_3 nanoparticles at 500 mA g^{-1}. f) Cycling performance of C-Fe_2O_3 at 500 mA g^{-1} after first three cycles at 100 mA g^{-1}. Reproduced with permission.[99] Copyright 2014, Elsevier Ltd.

at high post-treatment temperatures, which was due to the increased contact area between active materials and electrolyte, and the shortened transport distance for lithium ions and electrons in the Co_3O_4 nanosheets. As stated by the authors, the synthesized Co_3O_4 nanosheets indeed demonstrated the best electrochemical performance towards lithium storage among all reported Co_3O_4 samples.[102]

3.3.4. Nickel Oxides Prepared by SP

Liu's group prepared hollow spherical NiO particles and NiO-C nanocomposite as anodes for LIBs by applying SP

method.[103,104] For the hollow spherical NiO particles, it was found that the wall of the spherical hollow balls was composed of NiO nanospheres with sizes of 20–50 nm. The NiO-C nanocomposite also exhibited as spherical hollow shape with nanosized NiO particles surrounded by amorphous carbon forming the shell. Owing to the enhanced electrical conductivity and structural stability provided by carbon, the NiO-C nanocomposite demonstrated better electrochemical performance than bare NiO.

Choi et al. for the first time synthesized a yolk-shell structured NiO anode (**Figure 19**a–c) for LIBs by a one-step SP using a precursor solution containing nickel nitrate hexahydrate and sucrose.[105] The yolk-shell structured NiO possessed
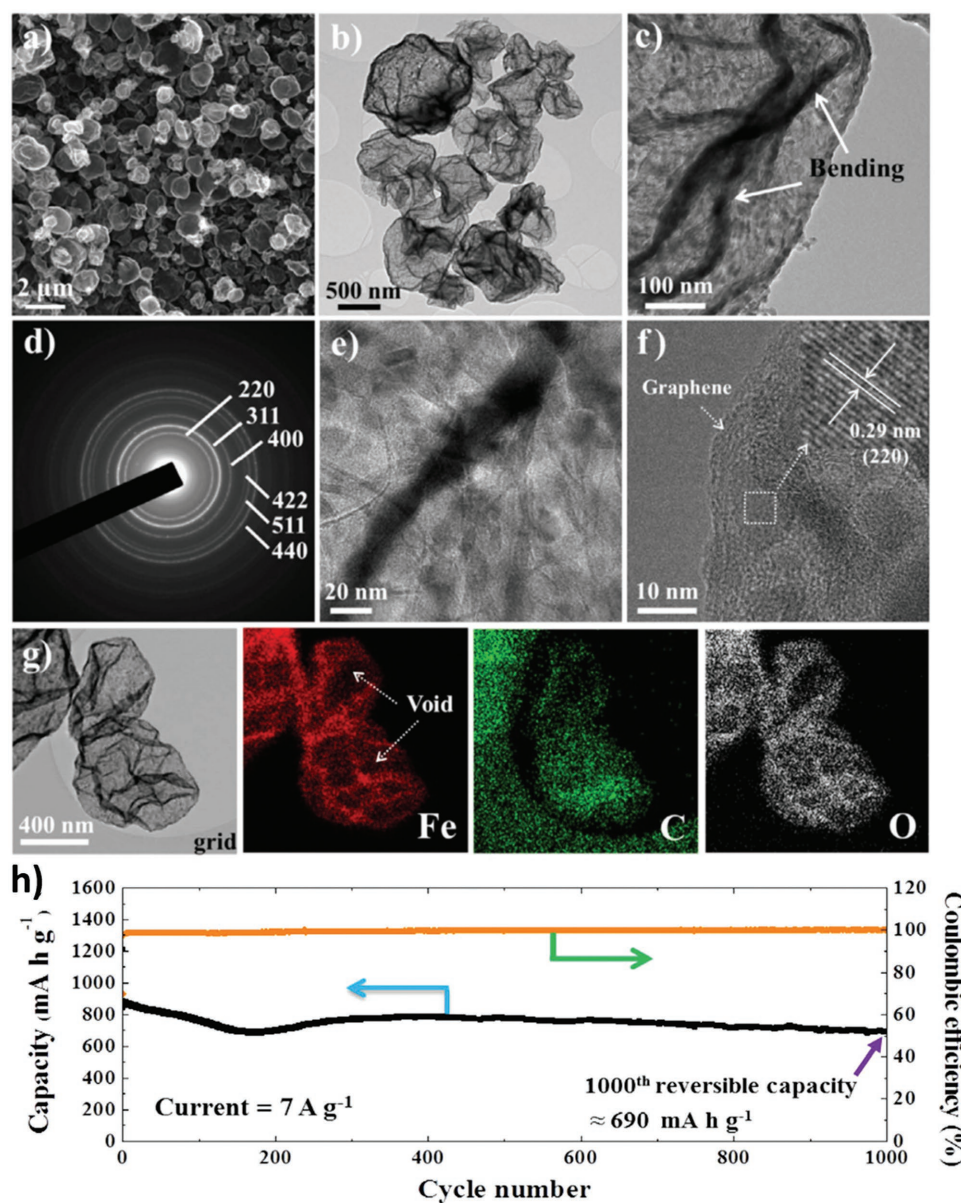
**ADVANCED
ENERGY
MATERIALS**

www.advenergymat.de

**ADVANCED
SCIENCE NEWS**

www.advancedsciencenews.com

REVIEW

Figure 17. a) SEM, b,c) TEM images, d) SAED pattern, e,f) HRTEM images, and g) EDS elemental mapping for Fe, C, O of Fe$_3$O$_4$-decorated hollow graphene balls. h) Long-term cycling performance of Fe$_3$O$_4$-decorated hollow graphene balls at 7 A g^{-1}. Reproduced with permission.[100] Copyright 2014, Elsevier Ltd.

a distinctive NiO@void@NiO structure, which was a result of repeated combustion and contraction of the NiO-C composite during the pyrolysis. For comparison, single-crystalline nano-cubic NiO was also prepared via flame SP at temperature >2500 °C. Electrochemical characterizations in lithium cells showed that the yolk-shell structured NiO demonstrated higher capacity retention and faster rate capability over the single-crystalline nano-cubic NiO (Figure 19d), which was attributed to the improved structural stability and enhanced lithium diffusion by the yolk-shell structured NiO over the single-crystalline nano-cubic NiO. Recently, the same group also reported a core-shell-structured Ni/NiO decorated graphene composite (Ni/NiO-graphene).[106] The composite was prepared by a two-step method. First, precursor solution containing nickel nitrate and

graphene oxide sheets was spray-pyrolyzed to form spherical graphene particles with Ni nanoclusters uniformly distributed all over graphene. Then, the composite was annealed in air under a low temperature of 300 °C to partially oxidize Ni to generate a Ni@NiO core-shell structure. In the Ni/NiO-graphene composite, graphene could accommodate the volume changes of NiO during lithiation-delithiation and prevent Ni crystal growth during electrochemical cycling. The existence of Ni not only improved the electrical conductivity but also facilitated the decomposition of Li$_2$O during the delithiation process. As a result, the Ni/NiO-graphene composite presented a higher lithium storage capacity and more stable cycling performance than hollow structured Ni-NiO composite and bare NiO sample.
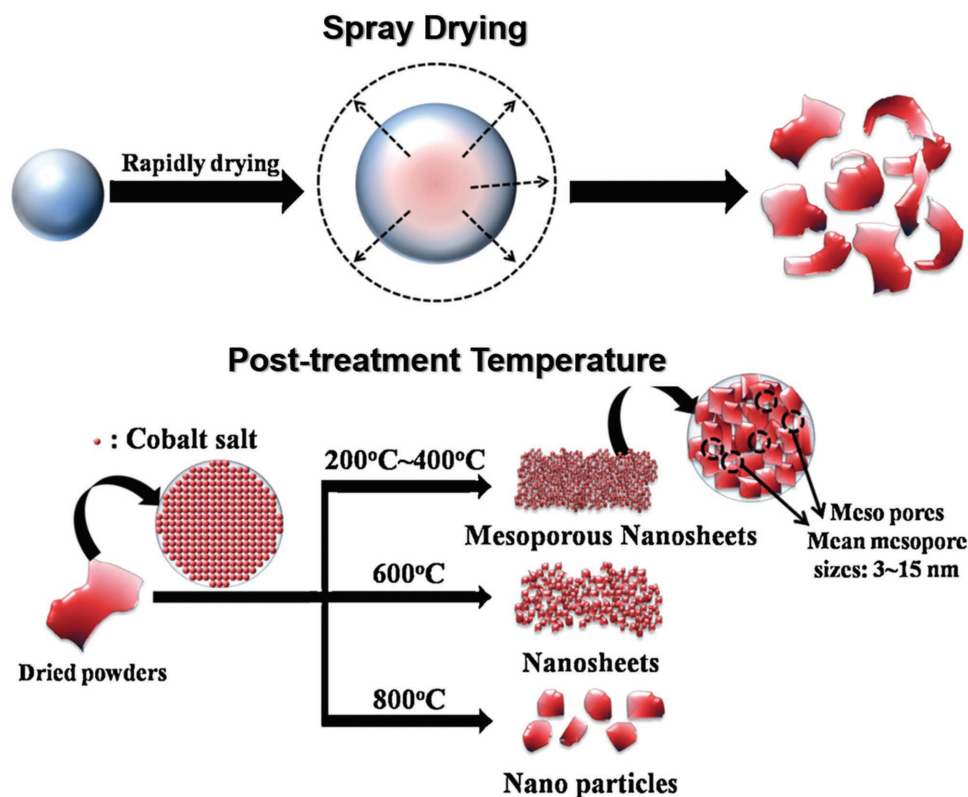
**ADVANCED
SCIENCE NEWS**
www.advancedsciencenews.com

**ADVANCED
ENERGY
MATERIALS**
www.advenergymat.de

REVIEW

Figure 18. A schematic illustration for the formation mechanisms of the nanosheet and nanoparticles. Reproduced with permission.[102] Copyright 2014, Elsevier Ltd.

3.3.5. Tin Oxides Prepared by SP

Different from iron oxides, cobalt oxides, and nickel oxides, which reversibly react with lithium ions through conversion reactions, tin oxides (e.g., SnO_2) react with lithium ions by first undergoing an irreversible conversion reaction to generate Sn and Li_2O. Then, the generated Sn can reversibly react with lithium ions via alloying/de-alloying reactions.[107]

A tin oxide composite, consisting of tin oxide doped with Si and SiO_2, was synthesized by flame-assisted ultrasonic SP.[108] The precursor solution was composed of $SnCl_4$, $SnCl_2$, $Si(OMe)_4$, and nitric acid dissolved in ethanol. In the composite, amorphous SiO_2 was found to be highly dispersed in a crystalline solid solution $Sn_{1-x}Si_xO_2$, as confirmed by X-ray diffraction (XRD) and Fourier transform infrared spectroscopy (FTIR). The addition of Si into tin oxide could reduce the oxidation state of tin, thus decreasing the first cycle irreversible capacity of the composite. After the 1st lithiation, the composite became metallic tin with highly dispersed amorphous SiO_2, Li_2SiO_3, and Li_2O. Based on lithium diffusivities calculated from the galvanostatic intermittent titration technique (GITT) results, it was speculated by the authors that these amorphous phases would enhance the interfacial lithium ion diffusion.

Ayouchi et al. prepared amorphous tin-oxide films by SP based on $SnCl_2 \cdot 2H_2O$ mixed with CH_3-COOH.[109] Compared with other film preparation methods, such as chemical vapor deposition (CVD) and electron-beam evaporation, SP method is an inexpensive and simple way to fabricate films. During the SP process, the precursor was deposited as separate droplets of regular size on the stainless steels, which were directly used as electrodes for cells assembly. X-ray photoelectron spectroscopy (XPS) analysis indicated that the amorphous tin-oxide film comprised a mixture of SnO_2 and SnO, which completely covered the substrate surface. Electrochemical tests showed that the films exhibited stable cycling performance for 100 cycles in lithium batteries. Later, a similar amorphous tin oxide film was fabricated by Mohamedi et al. via electrostatic SP followed by a post-annealing treatment.[110] Fine amorphous SnO_2 particles with a diameter less than 1 µm were uniformly deposited on Ni-substrate (**Figure 20**a). Galvanostatic cycling tests were done under two different cut-off voltage ranges (0.0–1.0 V vs Li/Li⁺ and 0.05–2.5 V vs Li/Li⁺), and the results showed that a stable cycling performance over 100 cycles could be obtained under the narrow testing voltage range (0.0–1.0 V vs Li/Li⁺) (Figure 20b). Based on the in-situ conductivity measurements, the authors suggested that insulating stoichiometric tin oxide was generated when the charging voltage was higher than 1.5 V (vs Li/Li⁺), which caused the instability of Li_2O matrix, leading to Sn aggregation and capacity decay.

Yuan et al. fabricated spherical porous SnO_2 by SP using an ethanol solution containing $SnCl_2 \cdot 2H_2O$.[111,112] It was found that the porous SnO_2 particles were composed of SnO_2 nanocrystals of about 5–10 nm. Due to the small size of SnO_2 and three-dimensional porous framework in the particles, the as-prepared spherical porous SnO_2 demonstrated better electrochemical cycling performances than commercial SnO_2.[111,112]
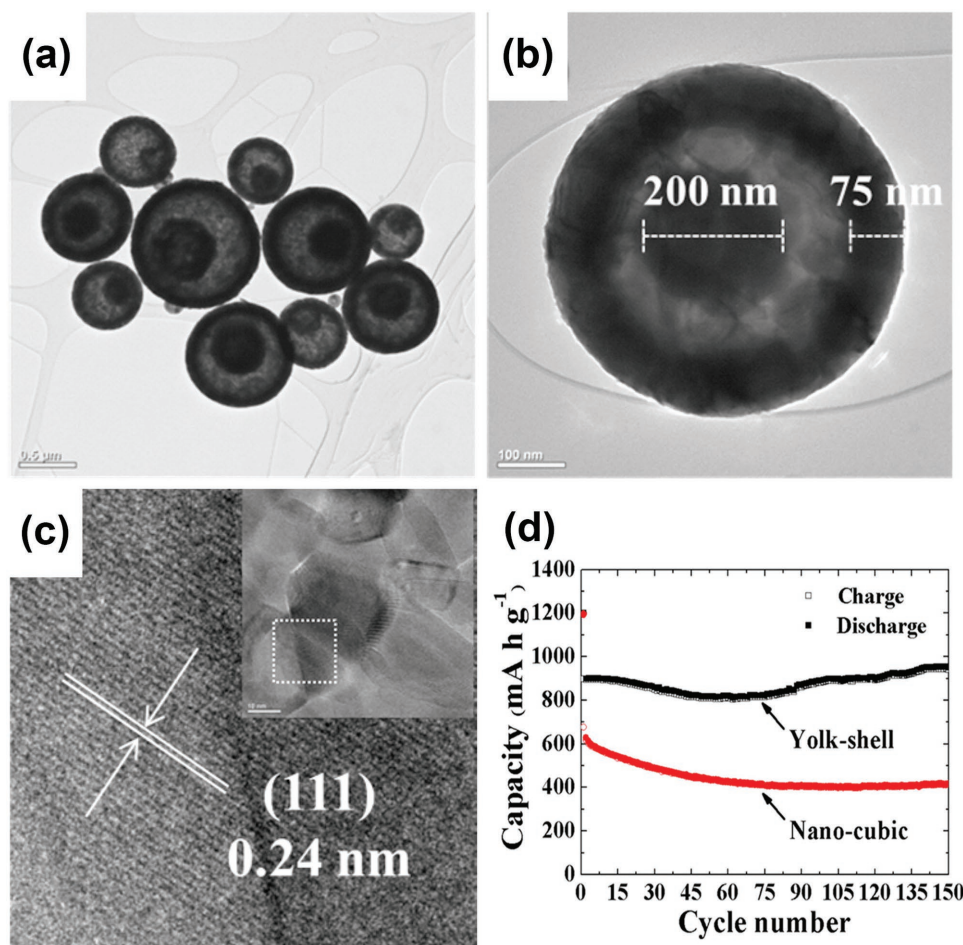
Figure 19. a,b) TEM and c) HRTEM images of yolk-shell NiO. d) Comparison of electrochemical performance between yolk-shell NiO and nano-cubic NiO. Reproduced with permission.[105] Copyright 2014, American Chemical Society.

The as-prepared spherical porous SnO_2 was further coated with conductive polyrole (PPy) to buffer the volume changes of SnO_2 during lithiation-delithiation.[113]

Recently, Kang et al. applied SP method to prepare a double-shelled SnO_2 yolk-shell-structured anode for LIBs (**Figure 21**a–c).[114] An aqueous solution composed of tin oxalate and sucrose was nebulized and air was used as the carrier gas

for the SP process. It was discovered that sucrose played a key role in the formation of the yolk-shell structure since the SnO_2 particles prepared from sucrose-free precursor solution displayed a filled spherical morphology. The formation mechanism of the double-shelled yolk-shell structure was schematically described in Figure 21d. Initially, micro-sized dense SnO_2-C composite particles with spherical shape were generated from
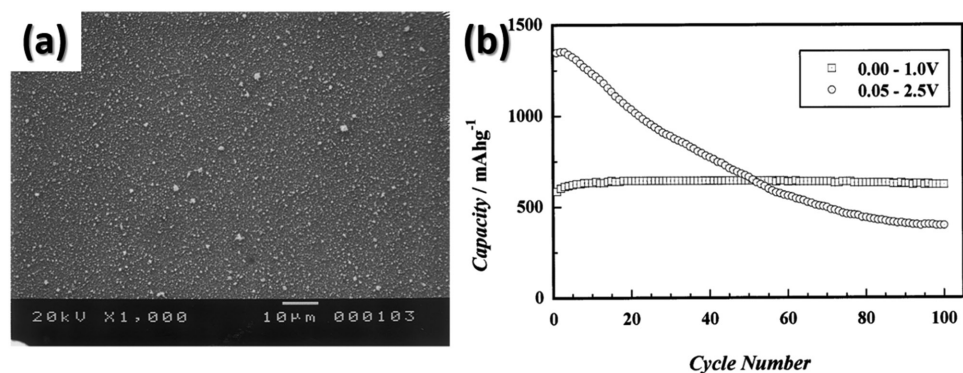

Figure 20. a) SEM image of tin oxide film prepared by electrostatic SP. b) Cycling performance of tin oxide film between different voltage ranges at 0.2 mA cm^{-2}. Reproduced with permission.[110] Copyright 2001, Elsevier Ltd.

ADVANCED
SCIENCE NEWS

www.advancedsciencenews.com
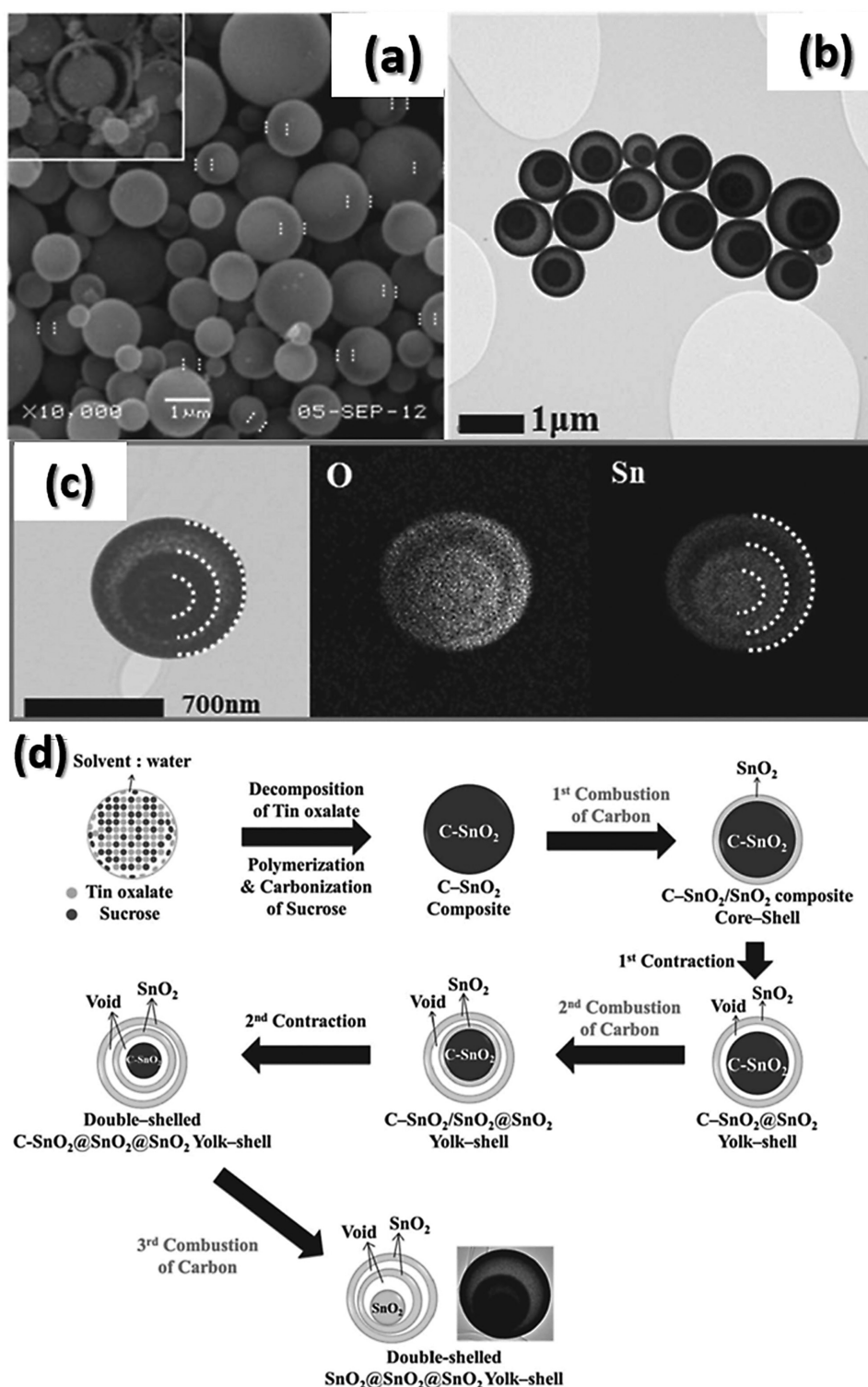
ADVANCED
ENERGY
MATERIALS

www.advenergymat.de

REVIEW

Figure 21. a) SEM, b) TEM, and c) elemental mapping of O and Sn for yolk-shell SnO_2 directly prepared using SP. d) Formation mechanism of double-shelled SnO_2 yolk-shell-structured powders. Reproduced with permission.[114] Copyright 2013, Wiley-VCH.

the fast decomposition of tin oxalate and polymerization/ carbonization of sucrose. Then, carbon on the outside of the particles was combusted and a core-shell-structured C-SnO_2/ SnO_2 composite was formed. However, combustion of carbon on the inside of the particles did not occur because the densely structured SnO_2-C prevented the sufficient supply of oxygen to the inside of the particles. Next, due to the different shrinking characteristics between crystalline SnO_2 shell and C-SnO_2 core,

ADVANCED
ENERGY
MATERIALS
www.advenergymat.de

ADVANCED
SCIENCE NEWS
www.advancedsciencenews.com

REVIEW

further heating leaded to the contraction of C-SnO$_2$ core and the formation of C-SnO$_2$@SnO$_2$ yolk-shell-structured particles. Then, oxygen was able to enter the voids to cause the combustion and contraction of C-SnO$_2$ core. By repeating above combustion and contraction process, the final double-shelled yolk-shell structured SnO$_2$ particles were produced. In a word, the double shelled yolk-shell structure was generated due to the step-by-step combustion of carbon in the dense SnO$_2$-C composite. Electrochemical characterizations showed that the yolk-shell structured SnO$_2$ exhibited a higher lithium storage capacity and better cycling performance than the densely structured SnO$_2$. Later, the same group also prepared a Janus-structured SnO$_2$-CuO composite, in which SnO$_2$ nanorods were attached on the spherical CuO nanoparticles.[115] The composite was produced through flame SP using an aqueous precursor solution containing SnSO$_4$, Cu(NO$_3$)$_2$·3H$_2$O, and citric acid. The formation mechanisms of the Janus-structured SnO$_2$-CuO involved evaporation, nucleation, crystallization, and phase separation of SnO$_2$ and CuO in the high temperature flame. When tested as anodes for LIBs, the SnO$_2$-CuO composite showed better capacity retention than pure SnO$_2$ electrode, which was attributed by the authors to the enhanced electron conduction and charge transfer by the rod-like SnO$_2$ and metallic Cu generated during the lithiation process.

3.3.6. Other Metal Oxides Prepared by SP

Besides the aforementioned iron oxides, cobalt oxides, nickel oxides, and tin oxides, a variety of other metal oxides and their composites, including copper oxides,[116] zinc oxides,[117] lead oxides,[118–120] manganese oxides,[121–124] and molybdenum oxides,[125,126] etc., were also prepared through SP for applications as anodes of LIBs. For example, our group has prepared an amorphous MnO$_x$-C nanocomposite as an anode for LIBs via SP using an aqueous solution consisting of manganese (ǁ) nitrate hydrate and sucrose in an argon atmosphere.[123] Thermal decomposition of manganese (ǁ) nitrate hydrate yielded MnO$_x$, and due to the very short residence time of aerosol droplets in the tube furnace, MnO$_x$ did not have sufficient time to crystalize but stayed amorphous. The value of x in the amorphous MnO$_x$-C nanocomposite was estimated to be around 1.37 from the XPS analysis. In the amorphous MnO$_x$-C nanocomposite particles, carbon was uniformly inter-dispersed among amorphous MnO$_x$ nanoparticles with a diameter around 5 nm, as implied by the TEM images of the composite particles before and after carbon removal (**Figure 22**a,b). It could improve the electrical conductivity, buffer the volume changes, and prevent Mn grains aggregation. Thanks to the unique structure of the amorphous MnO$_x$-C nanocomposite, the composite exhibited much-improved lithium storage capability than crystalline MnO$_x$ (Figure 22c).

In summary, for the preparation of metal oxides using SP, aqueous solutions containing inexpensive and water-soluble metal nitrates or chlorides were generally used. Compressed air is served as the carrier gas. Under air atmosphere, decomposition and oxidation of metal salts will generate the corresponding metal oxides. Organic materials, sucrose or citric acid, were often added in the precursor solutions. Most of organic materials will be burnt out to become CO$_2$ and H$_2$O. However, due to the instantaneous nature of SP, decomposition of organic materials can also occur to produce carbon. Depending on the processing parameters (e.g., residence time and pyrolysis temperature, etc.), carbon may or may not be preserved in the final products. The combustion of carbon will lead to hollow structures. As a result of decomposition and combustion processes, SP-prepared metal oxides often feature porous or hollow structures. Although these porous or hollow structures can accommodate the volume changes of metal oxides during cycling, giving rise to decent electrochemical cycling performances, they inevitably lower the 1st cycle Coulombic efficiency and volumetric energy density of metal oxides. From a practical point of view, future efforts are demanded to precisely control the properties of these porous/hollow structures, for example size and distribution of empty spaces, and to develop innovative electrode architectures.

4. Cathode Materials for LIBs Designed by SP

The current LIBs adopt transition metal (TM)-based oxides and phosphates as cathodes. The main research effort in this area is to increase the specific capacity and operation voltage while achieving long-term cycling performance. To reach this grand goal, the TM choice, impurity-free synthesis, and surface protection from side reactions are most critical. In this direction, SP can be a useful synthetic process because it allows for homogeneous TMs mixing and spontaneous formation of surface coating layer. Focusing on these aspects, the beneficial outcomes of SP for various LIB cathodes are presented for representative cases from this section.

4.1. LiCoO$_2$ Prepared by SP

As addressed above, LiCoO$_2$ has long been used for commercial LIB products based on various synthetic processes. SP uses precursor solutions where Li and Co are uniformly dissolved and therefore allows for homogeneous mixing between Li and Co in the atomic scale, leading to final compounds with high purity and designated compositions. The SP is usually followed by a heat treatment to improve the crystallinity. SP can also control the morphology of LiCoO$_2$ ranging from film, nano-powder, micro-powder, and hollow sphere.[127–132] Chen et al. reported LiCoO$_2$ film by SP in which amorphous phase was first produced at 280 °C.[127] The produced compound underwent an additional heat treatment at 340 °C to generate the hexagonal phase with high crystallinity. Li et al. produced ultrafine LiCoO$_2$ precursor particles by reacting lithium acetate, cobalt acetate, and poly ethylene glycol at a low temperature using pilot scale SP.[128] These precursor particles were heat-treated at 800 °C to obtain high crystalline LiCoO$_2$ powder. Although the designated alfa-NaFeO$_2$ structure was confirmed, the high temperature heat treatment causes agglomeration of particles, which is attributed to the hygroscopic nature of the precursor powder after the SP process. This powder exhibited a reversible capacity of 148 mA h g^{-1} when measured at 0.5 mA cm^{-2} in the range of 3.0–4.3 V vs Li/Li$^+$.

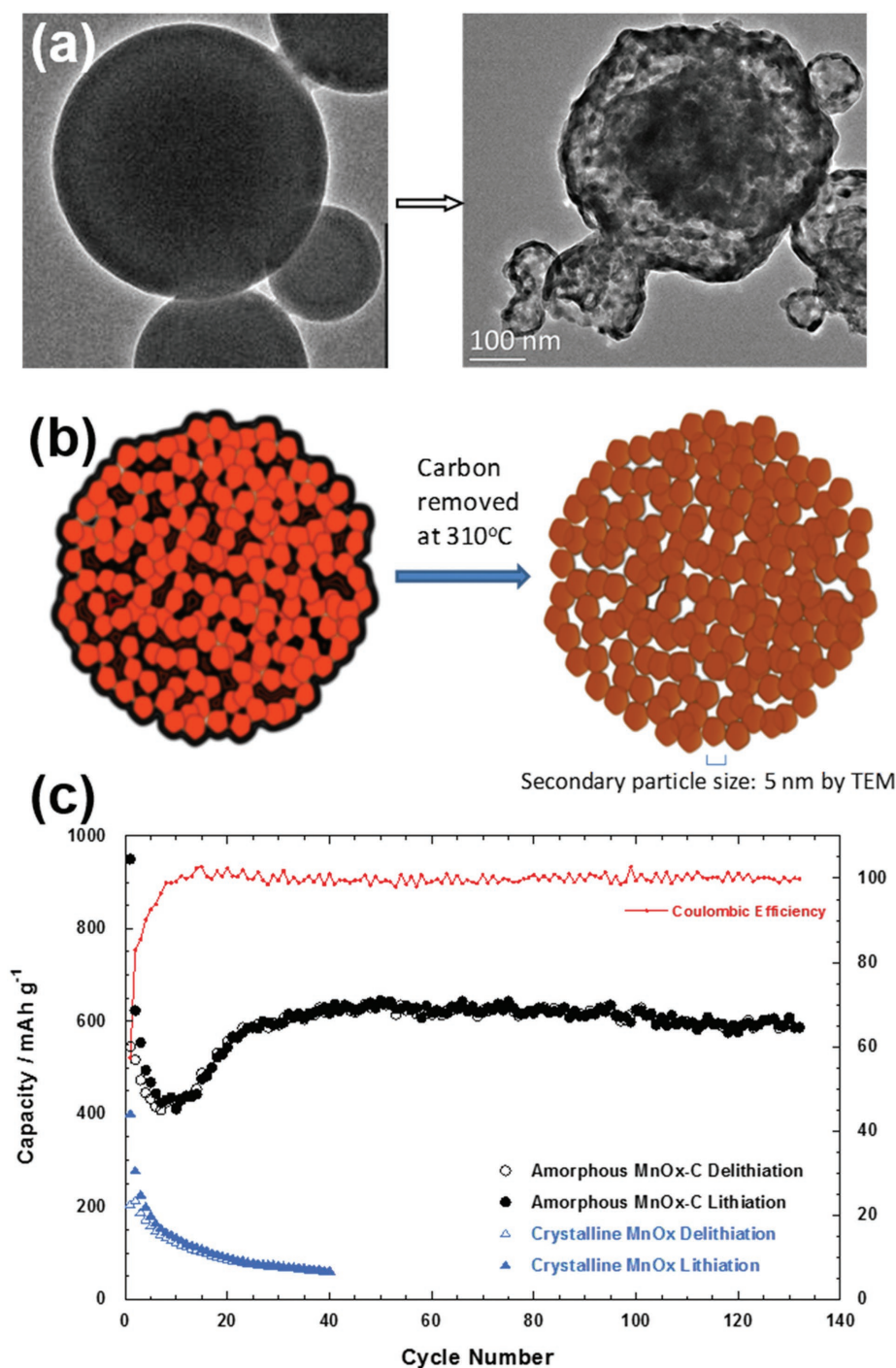www.advancedsciencenews.com

ADVANCED
ENERGY
MATERIALS
www.advenergymat.de

REVIEW

Figure 22. a) TEM image of the amorphous MnO_xC nanoparticles before and after carbon removal at 310 °C. b) A schematic illustration of MnO_x-C before and after carbon removal. c) Comparison of cycling performance between amorphous MnO_x-C and crystalline MnO_x. Reproduced with permission.[123] Copyright 2012, Wiley-VCH.

Zr-doping was also achieved by including a Zr-containing precursor, $ZrO(NO_3)_2 \cdot xH_2O$ in the SP precursor solution.[129] The solubility limit of Zr in $Li(Co_{1-x}Zr_x)O_2$ was $x = 0.01$. Above this concentration, a secondary phase, Li_2ZrO_3, was formed. The Zr doping at $x = 0.01$ increased the lattice distance by 0.8% and 0.6% in the a- and c-directions, respectively, as compared to the pristine phase. With the doping contents at $x = 0$, 0.005, 0.01, and 0.05, the initial discharging capacity changes from 144 mA h g^{-1} to 143 mA h g^{-1} to 139 mA h g^{-1} to 135 mA h g^{-1}, indicating that the Zr-doping decreases the specific capacity. However, at the same doping contents, the specific capacity after 50 cycles was 23, 62, 108 and 104 mA h g^{-1}, respectively, confirming that the capacity retention can be improved significantly with the optimal Zr-doping content. The Zr-doping also

ADVANCED
ENERGY
MATERIALS
www.advenergymat.de

ADVANCED
SCIENCE NEWS
www.advancedsciencenews.com

REVIEW

improves the rate performance. The enhanced performance is ascribed to the increased interlayer distance that facilitates Li-ion diffusion in the crystal structure with greater stability.

LiCoO$_2$ nano-powder coated with lithium borate glass (Li$_2$O-2B$_2$O$_3$) was also synthesized via ultrasonic flame SP.[130] Lithium boron oxide (LBO) glass holds high Li-ion conductivity and simultaneously protects the core active material from surface side reactions. For this synthesis, lithium nitrate, cobalt nitrate, and boric acid were dissolved in distilled water at the stoichiometric ratio. The droplets generated from an ultrasonic humidifier were fed into a flame at 2500 °C and each droplet passes through this flame for only several seconds. During this short process, the precursors are dried and decomposed, followed by nucleation, leading to the formation of LiCoO$_2$-LBO composite. Interestingly, even during such short period, this composite is produced spontaneously in a core-shell configuration, because the glass phase with relatively lower crystallinity naturally migrates to the outer regime of each droplet, while the LiCoO$_2$ core with higher crystallinity migrates in the opposite direction to the core of the droplet. From XPS analysis, the presence of boron was verified, and the LiCoO$_2$ samples with and without the LBO glass layer have diameters of 42 and 54 nm, respectively, according to TEM analysis. As in other SP syntheses for layered materials, the produced powder by SP was heat treated at a higher temperature (600 °C) for high crystallinity. In the electrochemical measurements, the specific capacity of the LiCoO$_2$ without the LBO glass coating started at 119 mA h g^{-1} but decayed to 85 mA h g^{-1} after 50 cycles, leading to 71% capacity retention. By contrast, the specific capacity of the LBO-coated sample started at 122 mA h g^{-1} and ended at 109 mA h g^{-1} after the same number of cycles, corresponding to 89% capacity retention, thus confirming the positive role of the LBO glass coating toward improved cycling performance. This study also demonstrates the usefulness of SP that can control the segregated composite structure depending on the crystallinity or density of components.

4.2. Layered Ni-Rich Cathode Materials Prepared by SP

Most of Ni-rich cathode materials suffer from insufficient cycle life because of the presence of unstable Ni^{4+}.[133,134] SP has turned out to be useful in stabilizing Ni-rich compounds by spontaneous core-shell composite formation including

protecting shell layer as well as uniform TM mixing.[135–137] Song et al. reported amorphous ZrO$_2$-coated LiNi$_{0.8}$Co$_{0.2}$O$_2$ created by a one-step modified flame SP.[135] They used a water-in-oil emulsion precursor solution to induce a core-shell structure; in the water region, the Li, Ni, and Co precursor components are confined, and in the oil region, the Zr precursor component is positioned. The precursor salts are decomposed at the flame to form LiNi$_{0.8}$Co$_{0.2}$O$_2$ and ZrO$_2$, respectively, in the core and shell regions. The charging specific capacity (157 mA h g^{-1}) of the ZrO$_2$-coated sample was higher than that (142 mA h g^{-1}) of the bare LiNi$_{0.8}$Co$_{0.2}$O$_2$ counterpart. The ZrO$_2$-coated sample also exhibited enhanced cycling performance (91% vs 75% capacity retention after 10 cycles) once again due to the ZrO$_2$ shell layer that protects Ni dissolution into the electrolyte, although these values leave more room for further improvement.

Ju et al. reported a combined SP and solid-state reaction process to synthesize LiNi$_{0.8}$Co$_{0.15}$Al$_{0.05}$O$_2$.[136] In the SP step, ethylene glycol, citric acid, and N-N-dimethlyformamide (a drying control chemical additive (DCCA)) were added to the precursor solution to generate Ni–Co–Al–O precursor powder, which was then reacted with LiOH via solid-state reaction. The addition of the DCCA promotes the densification of the LiCoO$_2$ powder in the hot reactor. The produced electrode showed 200 mA h g^{-1} in the first cycle at 0.1 C and this value decayed to 158 mA h g^{-1} after 40 cycles.

4.3. Ternary Transition Metal (TM) Layered Cathode Materials Prepared by SP

Other layered materials with relatively lower compositions of Ni synthesized by SP were also reported.[138–145] Obviously, LiNi$_{1/3}$Co$_{1/3}$Mn$_{1/3}$O$_2$ is the most well-known phase among them and has been used for commercial products for a while. Oh et al. produced layered Li[Ni$_{0.5}$Mn$_{0.5}$]$_{1-x}$Co$_x$O$_2$ (0<x<0.33) powder via SP.[138] The starting solution including nickel nitrate hexahydrate, cobalt nitrate hexahydrate, and manganese nitrate tetrahydrate was used to generate droplets, which were then introduced into a vertical quartz reactor at 500 °C. The generated powder was reacted with LiOH·H$_2$O at 900 °C to complete Li[Ni$_{0.4}$Mn$_{0.4}$Co$_{0.2}$]O$_2$ with high purity and crystallinity. The prepared particles have spherical morphology with diameters of 0.5–3 µm. According to XRD spectra (see **Figure 23**a), regardless of Co content, the compounds have consistent
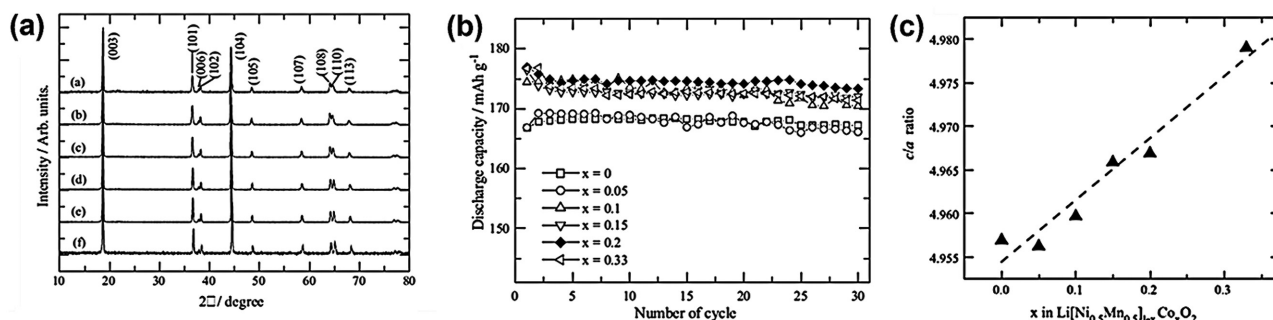

Figure 23. a) XRD patterns for Li[Ni$_{0.5}$Mn$_{0.5}$]$_{1-x}$Co$_x$O$_2$ powder prepared at various cobalt contents: a) x = 0, b) x = 0.05, c) x = 0.1, d) x = 0.15, e) x = 0.2, and f) x = 0.33. b) Cycle performance for various cobalt contents of Li/Li[Ni$_{0.5}$Mn$_{0.5}$]$_{1-x}$Co$_x$O$_2$ cells. c) c/a lattice parameter ratios at different Co contents. Reproduced with permission.[138] Copyright 2004, Elsevier Ltd.
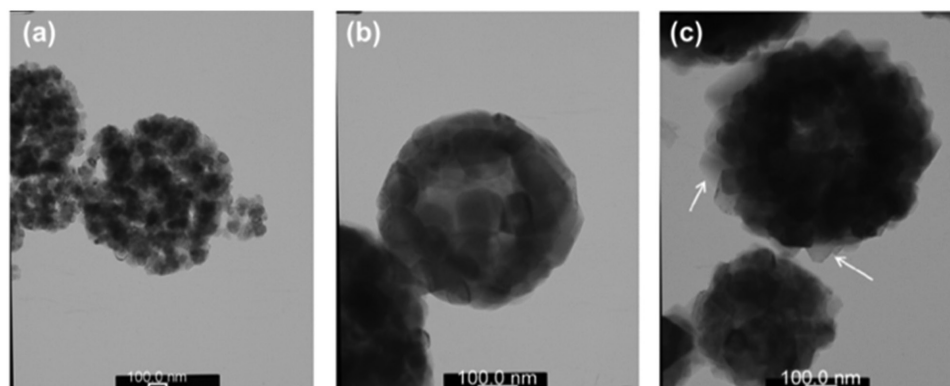
ADVANCED
SCIENCE NEWS
www.advancedsciencenews.com

ADVANCED
ENERGY
MATERIALS
www.advenergymat.de

REVIEW

Figure 24. TEM images of the $Li_2O-2B_2O_3$ (LBO)-glass modified $LiMn_2O_4$ powder prepared by spray pyrolysis. a) 0 wt% LBO, b) 1 wt% LBO, c) 5 wt% LBO. Reproduced with permission.[148] Copyright 2012, Elsevier Ltd.

hexagonal α-NaFeO$_2$ structure with the space group of R3m. By taking advantage of SP that can tune the composition in a sophisticated manner, the TM composition was varied to see its impact on the electrochemical performance. It was found that the discharging capacity increases linearly with the Co content (Figure 23b), which was explained by the increased c/a lattice parameter ratio that is known to be directly correlated with enhanced Li-ion diffusion (Figure 23c). Regardless of the Co-content, the samples show consistently good cycling performance (Figure 23b). The main sample, $Li[Ni_{0.4}Mn_{0.4}Co_{0.2}]O_2$, exhibited a high discharging capacity of 173 mA h g^{-1} with 98% capacity retention after 30 cycles at a constant current of 0.2 mA cm^{-2} (20 mA g^{-1}).

The same group used the aforementioned sequential process consisting of SP and solid-state reaction with LiOH, focusing on the $Li[Ni_{1/3}Co_{1/3}Mn_{1/3}]O_2$ composition.[139] This powder showed initial discharging capacities of 170 and 185 mA h g^{-1} at 30 and 55 °C, respectively, which decreased to 163 and 173 mA h g^{-1} after 50 cycles, corresponding to 96% and 94% capacity retentions. The three different categories of layered LIB cathode materials have experienced the benefits of SP, mostly based on well-controlled TM composition, homogeneous TMs mixing, and advanced core-shell structure.

4.4. Spinel $LiMn_2O_4$ Prepared by SP

Spinel $LiMn_2O_4$ was synthesized by both SP and spray drying processes.[146–151] Spinel $LiMn_2O_4$ can have good crystallinity by heat treatments at relatively lower temperatures, and can also have different nano-morphologies. Matsuda et al. demonstrated dense hollow spheres of $LiMn_2O_4$ using SP.[146] They studied the effect of specific surface area and particle morphology on the battery performance and concluded that the sample with higher crystallinity and smaller specific surface area exhibited better performance, which is presumably attributed to increased Mn^{2+} dissolution of the samples with higher specific surface areas. Sim et al. recently reported a core@void@shell structure.[147] This well-defined nanostructures allow impressive rate performance such that the discharging capacity changed from 134 mA h g^{-1} to 132 mA h g^{-1} to 123 mA h g^{-1} to 116 mA h g^{-1} when the

C-rate was increased from 1C to 3C to 5C to 10C. The SP's unique capability of creating core-shell structures was also used for spinel $LiMn_2O_4$. Choi et al. reported $Li_2O-2B_2O_3$ (LBO) glass containing $LiMn_2O_4$ prepared by one-pot SP.[148] The ionic conductivity of LBO facilitates Li-ion diffusion while the glass layer protects the $LiMn_2O_4$ powder from Mn^{2+} dissolution in the acidic electrolytes. **Figure 24**a–c display the TEM images of the LBO modified $LiMn_2O_4$ at LBO contents of 0, 1, and 5 wt%. With the increasing LBO content, it was observed that the $LiMn_2O_4$ powder becomes densified, which was also evidenced by Brunauer-Emmett-Teller (BET) surface area analyses. The initial reversible capacities at 0, 1, and 5 wt% of the LBO content were 117, 131, and 124 mA h g^{-1}, respectively. These values dropped to 93, 119, and 99 mA h g^{-1} after 100 cycles, indicating that the optimal LBO content is 1 wt%.

A SP process was also employed to achieve core-shell structures in combination with solid-sate reaction. Lee et al. reported a sequential synthesis of both processes; $LiMn_2O_4$ was first synthesized by solid-state reaction.[149] Next, this powder was added to a precursor solution containing Li, Ni, and Mn salts. A spray drying process at 200 °C gives rise to a core-shell structure where $LiMn_2O_4$ is coated uniformly with Li, Ni, and Mn elements. This powder then went through a heat treatment at 750 °C to complete the final $LiMn_2O_4$-$LiNi_{0.5}Mn_{0.5}O_2$ spinel-layered structure in a core-shell configuration. Overall synthetic scheme is graphically illustrated in **Figure 25**. High-angle annular dark-field (HAADF) STEM image confirms this core-shell structure, as the 'A' and 'B' regions in **Figure 26**a show the corresponding atomic arrangements. The role of the shell layer was clarified by the electrochemical tests at 60 °C. In the first cycles, the bare $LiMn_2O_4$ electrode exhibited a reversible capacity of 131 mA h g^{-1} with Coulombic efficiency of 99%, whereas the coated sample showed a lower capacity of 123 mA h g^{-1} but with increased Coulombic efficiency of 100% (Figure 26b). The smaller capacity of the heterostructure sample is attributed to the fact that during the synthesis, a certain portion of Li and Ni migrated into the core region on the expense of the decrease in the Mn^{3+} content. After 100 cycles at 60 °C, the heterostructure $LiMn_2O_4$ retained 85% of its initial capacity, while the bare $LiMn_2O_4$ sample retained only 56% (Figure 26c). The superior cyclability of the heterostructure
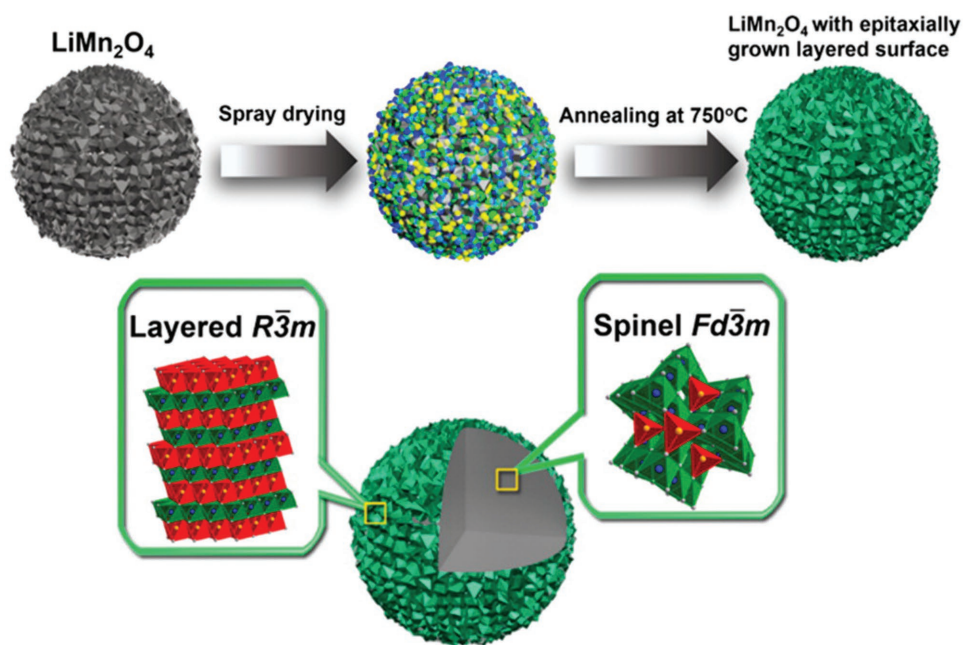
ADVANCED
ENERGY
MATERIALS
www.advenergymat.de

ADVANCED
SCIENCE NEWS
www.advancedsciencenews.com

REVIEW

Figure 25. A schematic illustration of synthetic process for core-shell $LiMn_2O_4$–$LiMn_{0.5}Ni_{0.5}O_2$ powder. Reproduced with permission.[149] Copyright 2014, American Chemical Society.

sample originates from the shell protective layer that mitigates Mn^{2+} dissolution. This investigation conveys a message that when integrated properly with other synthetic processes, SP or spray drying processes can develop advanced structural designs that can address critical issues of key battery active materials.

4.5. Metal Doped-$LiMn_2O_4$ Prepared by SP

There have been numerous works involving the substitution of Mn with other TMs such as Ni, Co, Al, Fe, and Cr in order to enhance the electrochemical performance of $LiMn_2O_4$.[152–158] SP has also been involved in such investigations. For example,
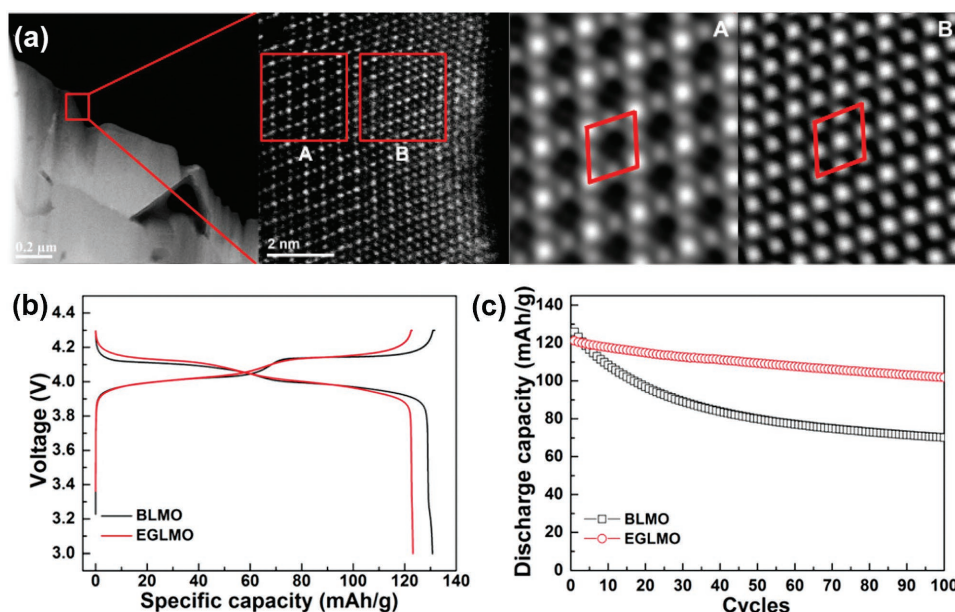

Figure 26. a) High-angle annular dark-field (HAADF) STEM images of surface of a cross-sectioned $LiMn_2O_4$–$LiMn_{0.5}Ni_{0.5}O_2$ particle and Fourier filtered images of region A and B marked by red squares. b) Initial charge/discharge profiles of the bare and heterostructure $LiMn_2O_4$ at 60 °C, and c) their cycling performance. Reproduced with permission.[149] Copyright 2014, American Chemical Society.
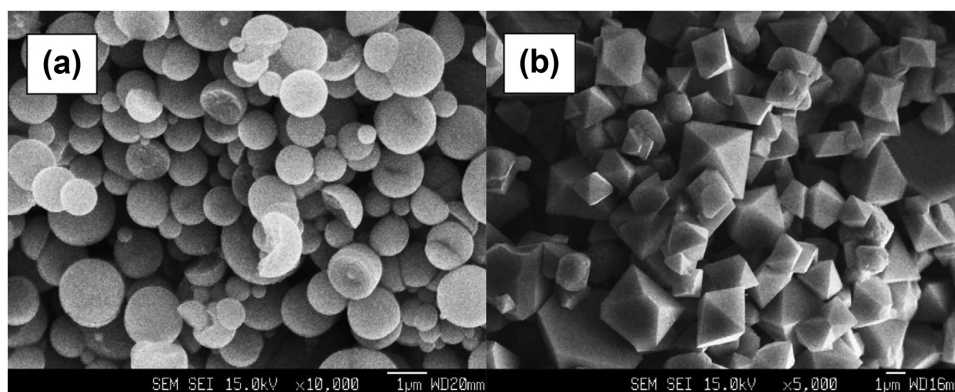
Figure 27. SEM images for a) as-prepared $LiNi_{0.5}Mn_{1.5}O_4$ and b) annealed $LiNi_{0.5}Mn_{1.5}O_4$ powder. Reproduced with permission.[152] Copyright 2004, Elsevier Ltd.

Taniguchi et al. reported the synthesis of materials such as $LiM_{1/6}Mn_{11/6}O_4$ (M = Mn, Co, Al, and Ni) and $LiM_{0.2}Mn_{1.8}O_4$ (M = Al, Cr, Fe, and Co) using SP and examined the electrochemical performance of these materials with different amounts of dopants.[154,155] Upon doping with different TMs, a notable change in the operating voltage was observed due to the dopant's active participation in the redox reactions that occur during charge/discharge. Moreover, the notorious dissolution of Mn^{2+} ions due to Jahn-Teller distortion is suppressed by increasing the average oxidation state of the Mn ions. From this work, it can be concluded that $LiMn_2O_4$ powder was successfully doped with other TMs via SP, leading to superior electrochemical performance.

As for $LiNi_{0.5}Mn_{1.5}O_4$ that operates at a high voltage of 4.7 V vs Li/Li+, Park et al. were the first to report its synthesis via SP.[152] The precursor solution was prepared with stoichiometric ratio of Li: Ni: Mn = 1.06: 0.5: 1.5. The aerosol stream was carried into a vertically positioned quartz reactor heated to 600 °C with a carrier gas (air) flowing at a rate of 10 L min^{-1}. The resultant powder was annealed sequentially for 24 h at 900 °C and 12 h at 700 °C afterwards for crystallization. **Figure 27** shows SEM images of the as-prepared $LiNi_{0.5}Mn_{1.5}O_4$ and annealed $LiNi_{0.5}Mn_{1.5}O_4$ powder. The as-prepared $LiNi_{0.5}Mn_{1.5}O_4$ powder before sintering has spherically-shaped particles, but shows a change in morphology to octahedral shapes after sintering. This phenomenon can be attributed to the short residence time in the reactor; the residence time is not enough for the particles to crystallize into thermodynamically stable forms. The XRD pattern of $LiNi_{0.5}Mn_{1.5}O_4$ powder confirmed the pure cubic spinel structure without any impurities such as NiO and $Li_xNi_{1-x}O$. This material delivers an initial discharge capacity of 140 mA h g^{-1} and shows excellent cycling behavior. The capacity retentions at 30 °C and 55 °C exceeded 99% and 97% of the initial capacities, respectively, after 50 cycles.

Choi et al. reported yolk-shell $LiNi_{0.5}Mn_{1.5}O_4$ powder prepared by continuous SP without a template for the first time.[153] Most cathode materials including $LiNi_{0.5}Mn_{1.5}O_4$ must go through a heat treatment process, but this usually results in the destruction of their respective particle structures. However, Choi et al. resolved this issue by synthesizing yolk-shell structured $LiNi_{0.5}Mn_{1.5}O_4$ powder that has relatively low crystallinity in a high temperature reactor during a short period

of time. The precursor solution is composed of stoichiometric amounts of Li, Ni, and Mn with excess sucrose. The excess sucrose plays a key role in creating the yolk-shell structure through carbonization in the reactor. In the upper part of the reactor, the aerosol droplets generated by an ultrasonic nebulizer create a composite of mixed metal oxides (Li, Mn, and Ni) and carbon from drying, decomposition, and carbonization. In the lower part, a combustion reaction between carbon and oxygen progressively occurs to result in a yolk-shell structure with a single or double shell. Single or double-shelled yolk-shell powder was prepared directly by SP with a short residence time of 4 s inside the hot wall reactor. **Figure 28** shows TEM images of yolk-shell $LiNi_{0.5}Mn_{1.5}O_4$ powder after heat treatments at 600 (Figure 28a,b), 700 (Figure 28c,d), and 750 °C (Figure 28e–g). These images show that the yolk-shell structure is maintained quite well at all heat treatment temperatures. HRTEM images (Figure 28d,f) also showed (111) interlayer distances of 0.47 nm, confirming the appropriate synthesis of $LiNi_{0.5}Mn_{1.5}O_4$. In addition, it can also be observed that the degree of crystallinity increased with temperature. When tested at different C-rates from 2 C to 40 C (Figure 28h), the powder annealed at 750 °C exhibited superior rate performance than the other two cases. Significantly, the sample annealed at 750 °C maintained 106 mA h g^{-1} even at 40 C, in comparison with those at 600 °C and 700 °C that preserved only 8 and 83 mA h g^{-1}, respectively. The better rate performance of the sample annealed at the higher temperature is attributed to the high crystallinity and phase homogeneity that facilitate Li-ion diffusion, in addition to the well-defined yolk-shell structure. This sample also showed stable cycling performance (89% retention after 1000 cycles) as displayed in Figure 28i.

4.6. LiFePO$_4$ Prepared by SP

$LiFePO_4$ is an attractive cathode material with high thermal stability and electrochemical performance with a potential of 3.45 V vs Li/Li+.[159–170] However, due to its inherently poor electronic and ionic conductivity, many attempts to enhance its performance have been made. Compared to other cathode materials, $LiFePO_4$ particles are synthesized in an oxygen-absent atmosphere of Ar, N_2, or H_2+Ar in order to form Fe^{2+}. In
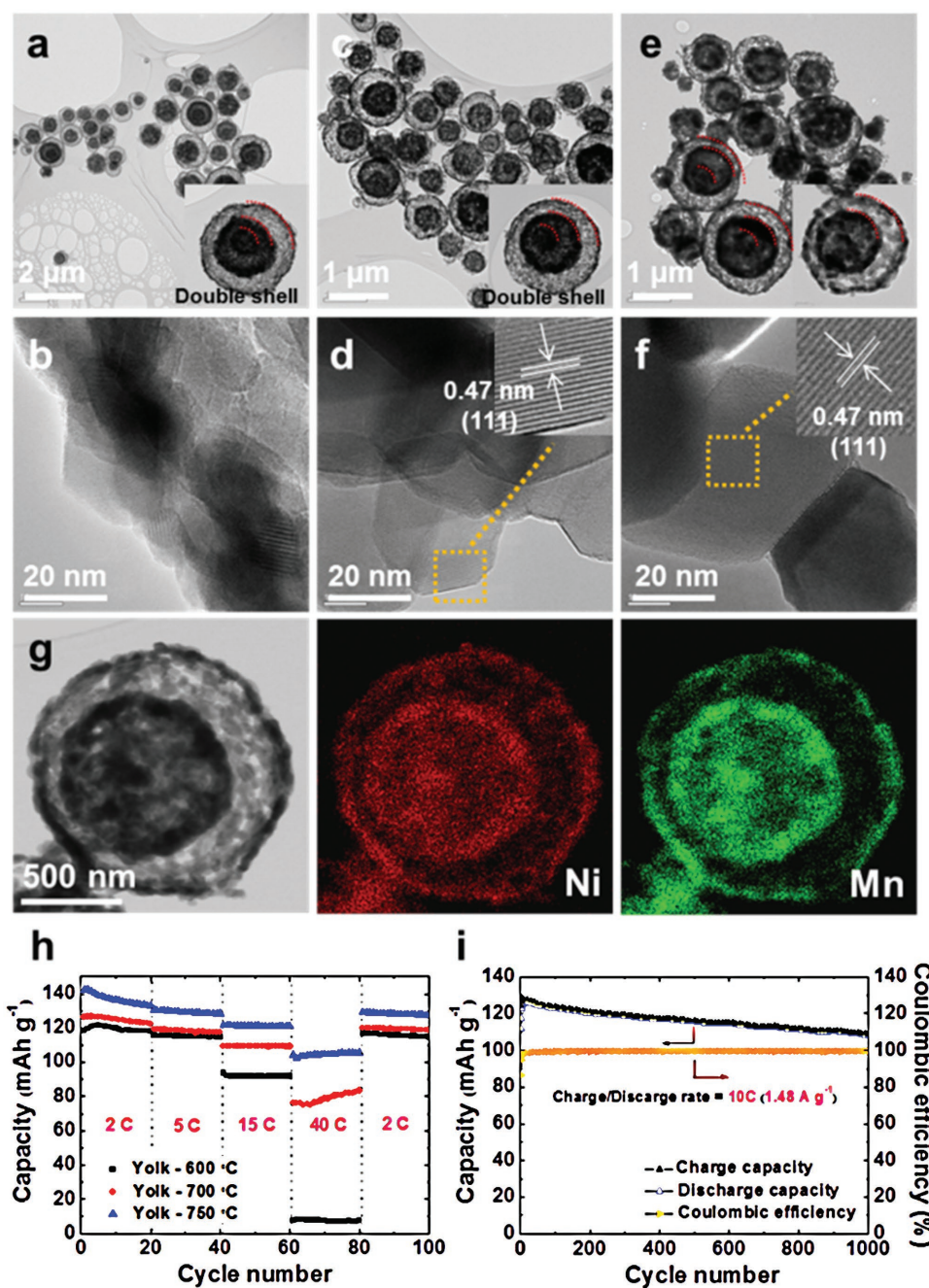
Figure 28. TEM and elemental-mapping images of the LiNi$_{0.5}$Mn$_{1.5}$O$_4$ yolk–shell powder. Post-treatment at a,b) 600 °C, c,d) 700 °C, and e–g) 750 °C. h) Rate performance for the samples heat-treated at the three different temperatures. i) Cyclability and Coulombic efficiencies of the sample treated at 750 °C. Reproduced with permission.[153] Copyright 2013, Royal Society of Chemistry.

order to overcome the poor conductivity, there have been many investigations into conductive carbon-derived composites with LiFePO$_4$.[159–170] In particular, publications that report LiFePO$_4$-related research using SP show two main directions. One approach involves synthesizing LiFePO$_4$/carbon composites by employing carbon precursors such as sucrose or citric acid in precursor solutions that already contain Li, Fe, and P.[159–165] For instance, Liu et al. reported micron-scale, three dimensional, nanoporous spherical LiFePO$_4$/carbon synthesized by

SP that showed excellent cyclability and superior rate capability.[159] **Figure 29**a is a schematic illustration of the synthesis of LiFePO$_4$/carbon composite powder. The spray solution contains Li, Fe, P ions along with sucrose. The metal salts inside the aerosol droplet are thermally decomposed at 700 °C in the reactor while sucrose is carbonized to amorphous carbon and coats the surface of LiFePO$_4$. During the post-treatment process, LiFePO$_4$ is crystallized while the amorphous carbon on the surface converts to conductive carbon. The final product
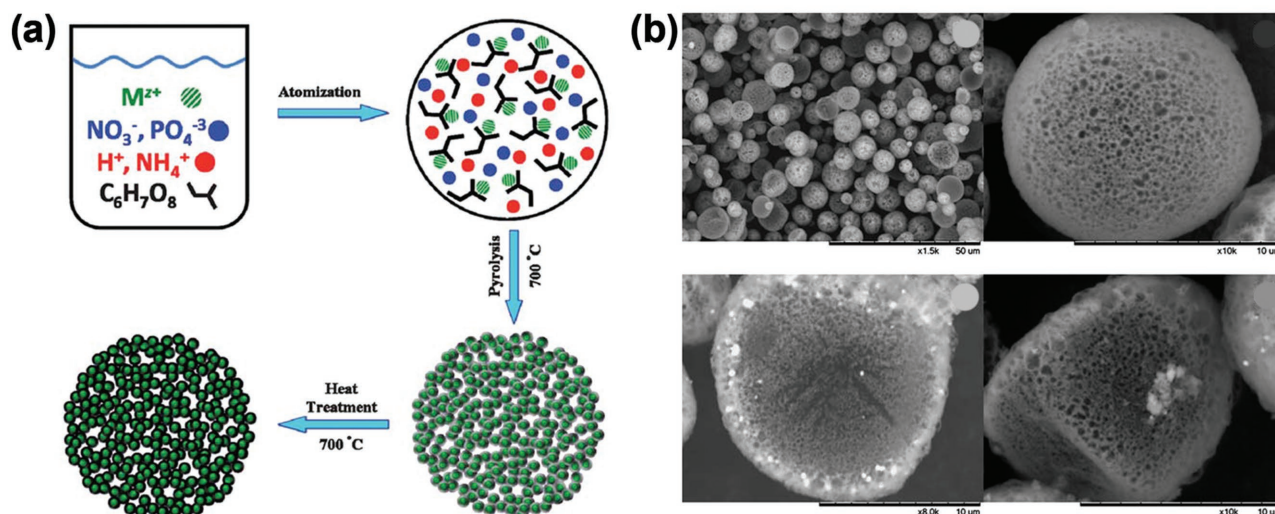
ADVANCED
SCIENCE NEWS
www.advancedsciencenews.com

ADVANCED
ENERGY
MATERIALS
www.advenergymat.de

REVIEW

Figure 29. a) A schematic illustration of the synthesis process and b) SEM images of LiFePO$_4$/carbon composite powder. Reproduced with permission.[159] Copyright 2011, Royal Society of Chemistry.

contains approximately 7.2 wt% of carbon, and the amount of carbon can be easily tuned by the amount of sucrose in the spray solution. The SEM images of LiFePO$_4$/carbon composite powder show spherical morphology with nanopores formed at the surface (Figure 29b). In electrochemical tests, at a low current density of 20 mA g^{-1}, the composite electrode delivers 153 mA h g^{-1} (corresponding to 165 mA h g^{-1} of LiFePO$_4$, very close to its theoretical capacity of 170 mA h g^{-1}), with 100% capacity retention over 100 cycles. Reversible capacities as high as 123 mA h g^{-1} and 106 mA h g^{-1} were achieved at 10 C and 20 C, respectively. The 3D conductive carbon coating and interconnected pore networks facilitate the kinetics of both electron transport and lithium ion diffusion within the particles.

The second approach involves synthesizing LiFePO$_4$ via SP and mechanically milling the resulting powder with conductive carbon in order to create LiFePO$_4$/carbon composites at the nano-scale.[166–170] The aforementioned milling process facilitates the coating of carbon on the surface of LiFePO$_4$ particles, leading to enhanced electrical conductivity. This method allows the economic and large-scale production of LiFePO$_4$/carbon composite powder. Konarova et al. reported the synthesis of such carbon-coated LiFePO$_4$ nanoparticles.[166] The milling process is easily modulated by changing the ratio between LiFePO$_4$ and carbon material to obtain the desired amount of carbon in the composite powder. Ultimately, the LiFePO$_4$/carbon composites showed significantly enhanced electrochemical performance in terms of reversible capacity, rate capability, and cycle life.

Moreover, other carbon sources than sucrose, such as graphene and carbon nanotubes, were integrated with LiFePO$_4$ to fabricate LiFePO$_4$/carbon composites.[167,168] Zhou et al. also reported the synthesis of graphene-modified LiFePO$_4$ via spray-drying and annealing (**Figure 30**a).[167] The precursor solution was prepared with uniformly dispersed LiFePO$_4$ nanoparticles and graphene oxide. The aerosol droplets formed from this solution are heat-treated to reduce graphene oxide. The SEM image in Figure 30b shows that the particles are approximately 3–5 µm in size. High-resolution SEM image (Figure 30c) shows

that LiFePO$_4$ nanoparticles are uniformly enveloped by graphene. The LiFePO$_4$ nanoparticles embedded in micro-sized spherical secondary particles were wrapped homogeneously with a graphene 3D network. The prepared LiFePO$_4$/graphene composite powder with controlled microstructure exhibited excellent rate performance and cycling stability. The 3D network of graphene offers a considerable benefit over conventional carbon coating in terms of enhanced electronic conductivity within the secondary particles.

Micro-dimensions of active particles are beneficial in achieving high performance LIB cathodes. Chen et al. compared the electrochemical performances of LiFe$_{0.6}$Mn$_{0.4}$PO$_4$/carbon nanoparticles and microspheres.[170] Through a spray drying process, the as-prepared nanoparticles were aggregated to the micron-scale, and the mean particle size of the microspheres was 13.5 µm. **Figure 31** shows the electrochemical results of conventional nanoparticles and spray-dried microspheres. Their specific discharge capacities were similar; carbon-coated LiFe$_{0.6}$Mn$_{0.4}$PO$_4$ nanoparticles delivered 164 mA h g^{-1}, while carbon-coated LiFe$_{0.6}$Mn$_{0.4}$PO$_4$ microspheres yielded 160 mA h g^{-1}. However, their volumetric capacities were quite different. The nanoparticles delivered 135 mA h cm^{-3}, while the microspheres delivered 222 mA h cm^{-3}. These values are translated to volumetric energy densities of 482.3 W h L^{-1} and 801.5 W h L^{-1}, respectively. Not only is the production of microsphere particles through spray drying cheap, fast, and scalable, but such powder can also maintain the merits of nanopowder while considerably raising the volumetric energy density.

4.7. LiMPO$_4$ (M = Mn, Co, Ni) Prepared by SP

In addition to LiFePO$_4$, other olivine-type LiMPO$_4$ (M = Mn, Co, and Ni) compounds have received much attention from the battery community due to their similar traits such as low cost, excellent cycle life, and thermal stability.[171–176] Oh et al. reported carbon-LiMnPO$_4$ nanocomposite synthesized
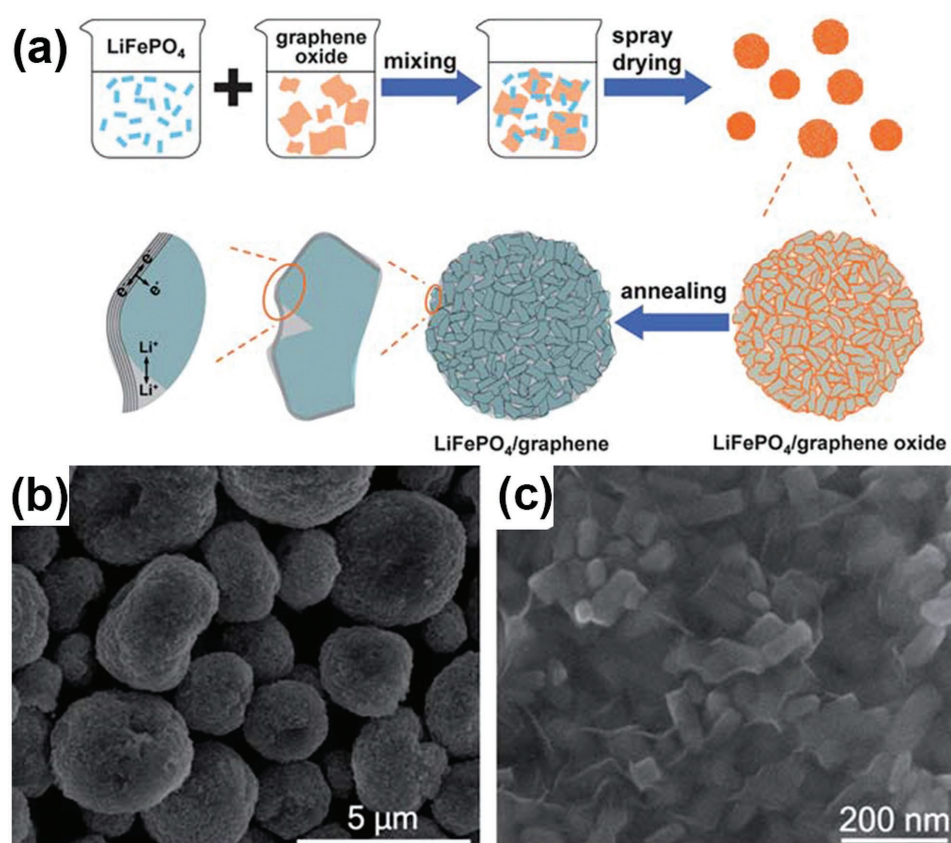
**ADVANCED
ENERGY
MATERIALS**

www.advenergymat.de

**ADVANCED
SCIENCE NEWS**

www.advancedsciencenews.com

Figure 30. a) Schematic diagram of the synthesis mechanism of LiFePO$_4$/graphene prepared by spray drying process and b,c) SEM images of the generated powder. Reproduced with permission.[167] Copyright 2011, Royal Society of Chemistry.

via ultrasonic SP followed by ball-milling.[171] Stoichiometric amounts of lithium dihydrogen phosphate acid (LiH$_2$PO$_4$) and manganese nitrate tetrahydrate [Mn(NO$_3$)$_2$·4H$_2$O] were dissolved in distilled water. This spray solution was then added to a solution containing citric acid and sucrose. The LiMnPO$_4$ powder prepared via SP was combined with acetylene black by ball milling. **Figure 32**a,b show TEM images of samples with 10 wt% and 30 wt% acetylene black. This series of TEM images confirm that the given amounts of carbon and LiMnPO$_4$ are mixed well. From the electrochemical evaluation (Figure 32c,d), it is apparent that the 30 wt% case shows superior electrochemical performance, implying that homogeneous mixing with carbon nanopowder can effectively overcome the inherent drawback of the olivine type materials, that is inferior electronic conductivity. In addition to the work addressed here, there have been several other reports observing similar composite effect by adopting SP processes.

LiCoPO$_4$, a compound that operates at a high potential of 4.8 V vs Li/Li$^+$, potentially offers a higher energy density than LiFePO$_4$.[172] However, like other olivine-type materials, LiCoPO$_4$ suffers from low electrical conductivity, resulting in poor electrochemical performance. Accordingly, there have been numerous attempts to address this issue. A promising approach has been using the SP process to synthesize LiCoPO$_4$/carbon composites. In essence, these materials displayed improved cycle life while preserving high operating voltage of ≈4.8 V vs Li/Li$^+$. Taniguichi et al.'s work on

LiCo$_x$Mn$_{1-x}$PO$_4$/carbon and LiCo$_{1/3}$Mn$_{1/3}$Fe$_{1/3}$PO$_4$/carbon nanocomposites is a good case in this point.[177,178] They were able to successfully synthesize pure multi-component, olivine-type materials based on the unique SP's advantage of being able to easily adjust the TM stoichiometry of the target materials without forming impurities. As a result, these multi-component, olivine-type materials demonstrated extended cycle life and good rate capability, concluding that a multi-component combination in the 'M' position of LiMPO$_4$ could improve the electrochemical performances than a single-component counterpart.

4.8. Lithium/Manganese-Rich Cathode Materials Prepared by SP

The performance of Li/Mn-rich cathodes is greatly affected by their synthesis. SP is one mode of synthesis that produces pure lithium/Mn-rich phases.[179–184] For example, Lengyel et al. also reported the electrochemical properties of the layered xLi$_2$MnO$_3$·(1–x)Li(Ni$_{1/3}$Mn$_{1/3}$Co$_{1/3}$)O$_2$ (x = 0.3, 0.5, 0.7) synthesized via SP.[179] The precursor solution was prepared by using stoichiometric amounts of metal ion precursors. The resulting powder was calcinated at 900 °C to obtain high crystallinity. Particles synthesized by this process show excellent uniformity and high purity at the nanoscale, with less voltage fading compared with similar materials synthesized by co-precipitation. In electrochemical tests, a decrease in the
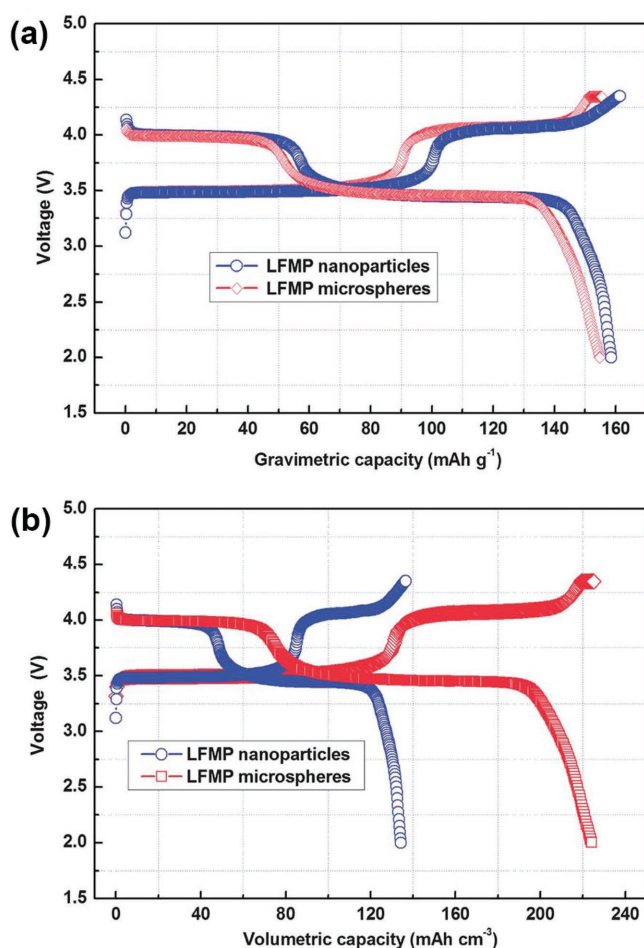
ADVANCED
SCIENCE NEWS
www.advancedsciencenews.com

ADVANCED
ENERGY
MATERIALS
www.advenergymat.de

REVIEW

Figure 31. Comparison of initial charge–discharge curves for $LiFe_{0.6}Mn_{0.4}PO_4$ (LFMP)/carbon nanoparticles and microspheres in terms of a) gravimetric capacity and b) volumetric capacity. Reproduced with permission.[170] Copyright 2013, Royal Society of Chemistry.

Li_2MnO_3 content led to mitigated voltage fading, meaning that $x = 0.3$ (or $0.3Li_2MnO_3 \cdot 0.7Li(Ni_{1/3}Mn_{1/3}Co_{1/3})O_2$) showed the best structural stability over repeated cycling. Furthermore, the samples prepared from SP and those from co-precipitation methods were compared for $x = 0.3$. Electrochemical performance data revealed that while the initial and 16th charge capacities of materials prepared by SP were 367 and 278 mA h g^{-1}, respectively, those of materials prepared by co-precipitation were 302 and 232 mA h g^{-1}, respectively. Such superior results for samples from SP suggest that SP offers higher purity and uniformity of active powder.

Recently, Oh et al. introduced a surface modification technique using spray drying to coat reduced graphene oxide (rGO) on materials.[180] They selected $0.4Li_2MnO_3 \cdot 0.6LiNi_{1/3}Co_{1/3}Mn_{1/3}O_2$ to apply this technique. The precursor solution was prepared with lithium-rich cathode material powder and graphene oxide colloids in an aqueous medium. **Figure 33**a,b are schematic illustrations of the anticipated effects of using conventional oxide coatings and rGO coatings. The rGO coating is more suitable for wrapping the entire surface of the particles and thus for preventing direct interaction between

the surface of the cathode material and the electrolyte while forming a good electron pathway at the surface. The SEM image in Figure 33c portrays that rGO with a crumpled morphology coats the active powder uniformly. The HR-TEM image (Figure 33d) indicates that the rGO coating consists of several graphene layers. Figure 33e,f show the rate capability and cycle performance of the pristine (denoted as PS) and rGO-coated $0.4Li_2MnO_3 \cdot 0.6LiNi_{1/3}Co_{1/3}Mn_{1/3}O_2$ (denoted as PGO) powder. The excellent electrical conductivity of graphene and its protection against direct contact with the electrolyte operate in synergy toward enhancing the electrochemical performance, such as improved cycle life and rate capability.

In a similar manner, Lim et al. reported their work on the electrochemical performance of rGO-wrapped Li-rich cathode material by self-assembly.[181] This involved synthesizing Li-rich powder by SP, followed by wrapping it with rGO sheets. For the effective wrapping, electrostatic interaction between rGO and Li-rich active powder was utilized. To this end, rGO was functionalized with polydiallyldimethylammonium chloride (PDDA). The PDDA-rGO sheets served as a protective layer and a conductive material, resulting in improved retention capacity from 56 to 81% after 90 cycles as compared with the bare active powder. Thus, it is generalized that uniform rGO surface modification of SP-synthesized cathode materials is a viable way to enhance electrochemical performance of the host active materials that suffer from moderate electronic conductivity and surface side reactions.

4.9. V_2O_5 and Vanadium-Based Cathode Materials Prepared by SP

Vanadium-based materials such as V_2O_5 and LiV_3O_8 offer high capacities as cathode materials and have been synthesized into various morphologies through SP. Dense particles,[185–187] yolk-shell structures,[188,189] graphene composites,[190] and CNT composites,[191] etc.,[192,193] are some examples that have been reported to improve electrochemical performance when combined with the vanadium-based active compounds. The temperature dependence of V_2O_5 morphology during SP has been previously reported along with a recent report on the economic and large-scale synthesis of yolk-shell V_2O_5 and LiV_3O_8.[188,189] Ko et al. introduced a new strategy for synthesizing yolk-shell V_2O_5 powder by using a simplified SP and post-treatment process.[188] First, the vanadium precursor and sucrose were dissolved in an aqueous spray solution, which was then converted to aerosols under a N_2 atmosphere to produce V_2O_3-carbon composites. Then, this powder was annealed at 400 °C under air to produce yolk-shell V_2O_5-carbon composite powder. The formation of yolk-shell structure was attributed to the fact that upon combustion of nanoscale composites distributed within carbon composites, the vanadium oxide converts to a yolk-shell structure due to a step-wise combustion of carbon. The rate performance of the yolk-shell and densely structured V_2O_5 powder was investigated from 100 mA g^{-1} to 1000 mA g^{-1}. The yolk-shell samples showed higher charge/discharge capacities than the dense ones. This result can be explained by the fact that the yolk-shell structure facilitates easier penetration of electrolyte within the particle, shortening the diffusion path of Li ions.
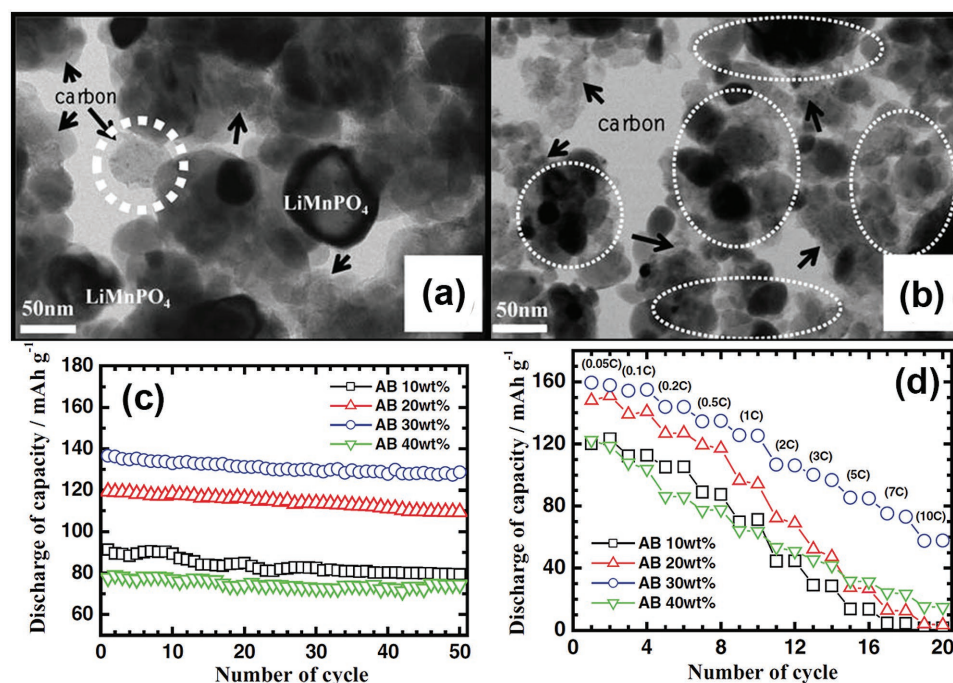
ADVANCED
ENERGY
MATERIALS
www.advenergymat.de

ADVANCED
SCIENCE NEWS
www.advancedsciencenews.com

REVIEW

Figure 32. SEM images of LiMnPO$_4$/carbon composite powder with different amounts of acetylene black: a) 10 wt% carbon, b) 30 wt% carbon (arrows indicate the carbon particles, white circles mark the LiMnPO$_4$ clusters). c) Cycle performance and d) rate performance at different acetylene black contents. Reproduced with permission.[171] Copyright 2010, Wiley-VCH.

Choi et al. reported the synthesis mechanism and electrochemical properties of V$_2$O$_5$ nanocrystals on reduced graphene oxide ball (RGB) by SP.[190] To improve the electronic conductivity of V$_2$O$_5$ and overcome its low Li-ion diffusivity, RGO-V$_2$O$_5$ composites were synthesized. **Figure 34**a describes the formation mechanism of the RGB-V$_2$O$_5$ composite powder. RGB-VO$_2$ composite powder was synthesized from a colloidal solution of vanadium ions and graphene oxide. The drying and decomposition of droplets produced the RGB-VO$_2$ in the front part of the tubular reactor maintained at 600 °C. At the same time, the graphene oxide sheets of the composite powder were reduced by thermal treatment and formed a RGB-VO$_2$ in the rear part of the reactor. The VO$_2$ in the RGB-VO$_2$ composite was converted to V$_2$O$_5$ through calcination at 300 °C under air. The SEM images show that the crumpled structure of the RGB-VO$_2$ composite was maintained after the post-treatment. The V$_2$O$_5$ powder made from a solution without graphene oxide has a porous structure. Figure 34b displays the cycling performances of the RGB-V$_2$O$_5$ composite and porous V$_2$O$_5$ (P-V$_2$O$_5$) powder at a current density of 1000 mA g^{-1}. The maximum discharge capacities of the RGB-V$_2$O$_5$ composite and P-V$_2$O$_5$powder obtained in the first and second cycles, respectively, were 282 and 218 mA h g^{-1}. The RGB-V$_2$O$_5$ composite and P-V$_2$O$_5$powder delivered discharge capacities of 214 and 152 mA h g^{-1} after 100 cycles, respectively, and the corresponding capacity retentions were 76% and 70%. The rate performances of the RGB-V$_2$O$_5$ composite and P-V$_2$O$_5$ powder are shown in Figure 34c, in which the current density was increased from 300 to 1500 mA g^{-1} in a stepwise manner. The RGB-V$_2$O$_5$ composite had discharge capacities of 249, 231, 218, 209, and 200 mA h g^{-1} at the 10th cycle for current

densities of 300, 600, 900, 1200, and 1500 mA g^{-1}, respectively. However, the P-V$_2$O$_5$powder showed discharge capacities of 197, 172, 155, 144, and 128 mA h g^{-1} at the 10th cycles. The authors offered the explanation that the reduced graphene ball substrate of the RGB-V$_2$O$_5$ composite improved the electrochemical performances because of the high electrical conductivity of graphene. Also, the nanosized V$_2$O$_5$ nanocrystals on the RGB enhanced the Li$^+$ diffusion and facilitated a fast charge/discharge process. Jia et al. took a similar approach by synthesizing spherical V$_2$O$_5$-MWCNT composites via spray drying.[191] The prepared samples consisted of uniformly mixed V$_2$O$_5$ nanoparticles and MWCNTs. Also, the MWCNTs embedded between V$_2$O$_5$ provided improved ion and electron transport pathways, leading to enhanced electrochemical performance.

Ko et al. synthesized Li$_3$V$_2$(PO$_4$)$_3$ and Li$_3$V$_2$(PO$_4$)$_3$/carbon composite powder by SP from spray solutions with and without sucrose.[194] Pure Li$_3$V$_2$(PO$_4$)$_3$ powder was synthesized by first preparing the precursor powder from a reactor at 1300 °C followed by heat treatment at 700 °C under a reducing atmosphere. The powder showed different hollow structures depending on the amount of sucrose used in the solution, and powder without any sucrose showed densely structured particles. According to XRD analyses, the mean crystallite sizes of Li$_3$V$_2$(PO$_4$)$_3$ with 0, 0.1, 0.3, and 0.5 M sucrose were 28, 29, 29, and 44 nm, respectively. Electrochemical performance tests revealed that Li$_3$V$_2$(PO$_4$)/carbon powder obtained by including sucrose showed better performance than their counterparts without sucrose. These results indicate that the carbon in the composites compensates for the low electrical conductivity of the bare Li$_3$V$_2$(PO$_4$)$_3$.

ADVANCED
SCIENCE NEWS
www.advancedsciencenews.com

ADVANCED
ENERGY
MATERIALS
www.advenergymat.de

REVIEW

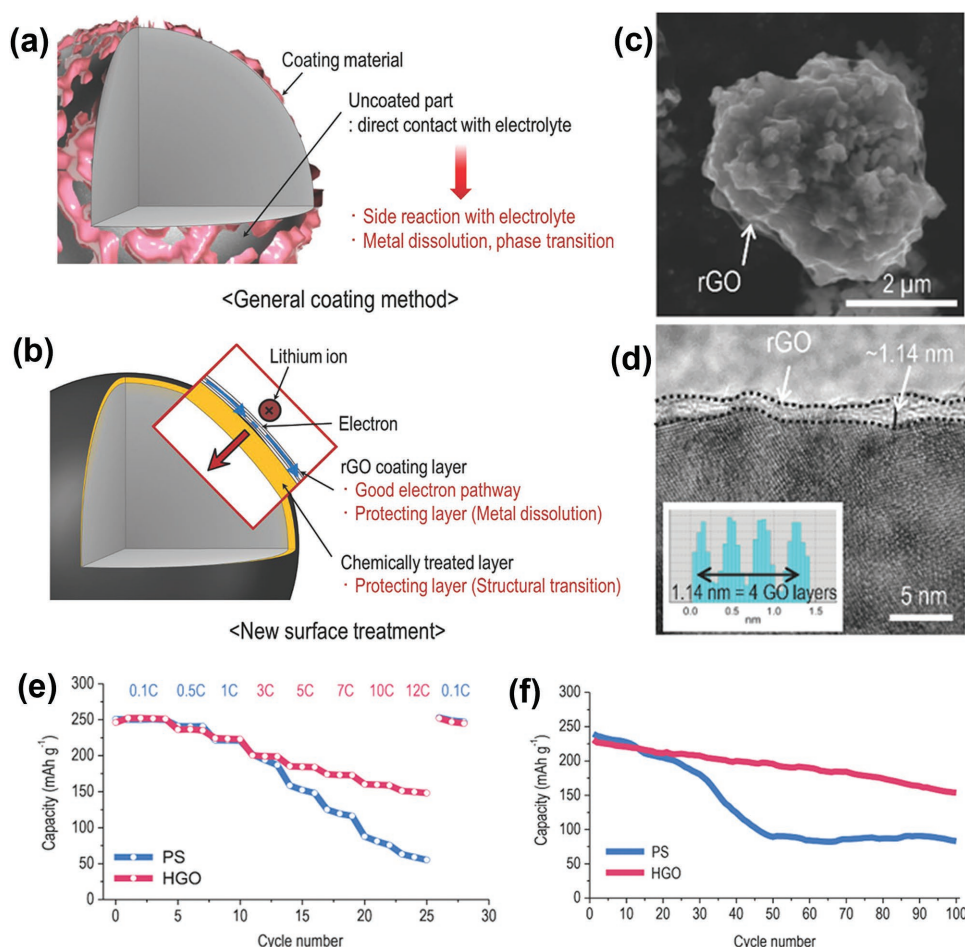**Figure 33.** Schematic view of a) conventional particle coating and b) reduced graphene oxide (rGO) coating. c) SEM image of rGO-coated $0.4Li_2MnO_3 \cdot 0.6LiNi_{1/3}Co_{1/3}Mn_{1/3}O_2$ and d) its HRTEM image showing the rGO coating consisting of several graphene layers. e) Rate and f) cycling performance of pristine (denoted as PS) and rGO-coated $0.4Li_2MnO_3 \cdot 0.6LiNi_{1/3}Co_{1/3}Mn_{1/3}O_2$ (denoted as PGO). Reproduced with permission.[180] Copyright 2014, Wiley-VCH.

Spherical $Li_3V_2(PO_4)_3$/carbon composites were also successfully synthesized via two different spray drying processes by Zhang et al.[195] Two different forms of $Li_3V_2(PO_4)_3$/carbon composites were synthesized depending on the order of adding sodium carboxymethyl cellulose (Na-CMC) in the spray drying process. Na-CMC was used as a carbon precursor, reducing agent, and a Na-containing dopant. **Figure 35** illustrates the formation mechanism of dense and hollow $Li_3V_2(PO_4)_3$/carbon composites with Na-CMC. If Na-CMC is added after pre-sintering, a dense structure is formed. On the other hand, adding Na-CMC before pre-sintering results in a hollow structure. Compared to hollow $Li_3V_2(PO_4)_3$/carbon (B), dense $Li_3V_2(PO_4)_3$/carbon (A) has higher tap density and better performance at all C-rates, implying that the order of adding Na-CMC in the spray drying process has a decisive impact on the tap density and electrochemical performance.

4.10. Other Polyanionic Cathode Materials Prepared by SP

Taniguchi et al. has employed SP for complicated compositions in addition to the aforementioned conventional cathode

materials. $Li_2MP_2O_7$ and Li_2MSiO_4 (M = Fe, Mn) are two good examples in this direction.[196,197] In particular, they reported the synthesis of $Li_2FeP_2O_7$/carbon and $Li_2MnP_2O_7$/composites using SP and wet ball milling followed by annealing. The XRD peaks of the final products were indexed to a monoclinic structure with the space group P2$_1$/c. Upon electrochemical evaluation, it appeared that the TM in the 'M' position was an active redox centre from which reversible capacity was attained. However, a low capacity of 70 mA h g^{-1} was quite short of its theoretical capacity of 220 mA h g^{-1}. While the reason for this remains unclear, its high theoretical capacity leaves much room for future research.

Lithium transition metal silicates (Li_2MSiO_4, M = Fe, Mn) are attractive candidates for cathode materials due to their low cost, thermal stability, and high theoretical capacity (334 mA h g^{-1}). However, Li_2MSiO_4 is not free from issues such as low lithium ion diffusivity and poor electronic conductivity. Shao et al. has conducted research related to these materials, particularly preparing composites containing conductive carbon powder and TM silicates through SP. At a rate of 0.05C, the Li_2FeSiO_4/carbon nanocomposites delivered a rather

ADVANCED
ENERGY
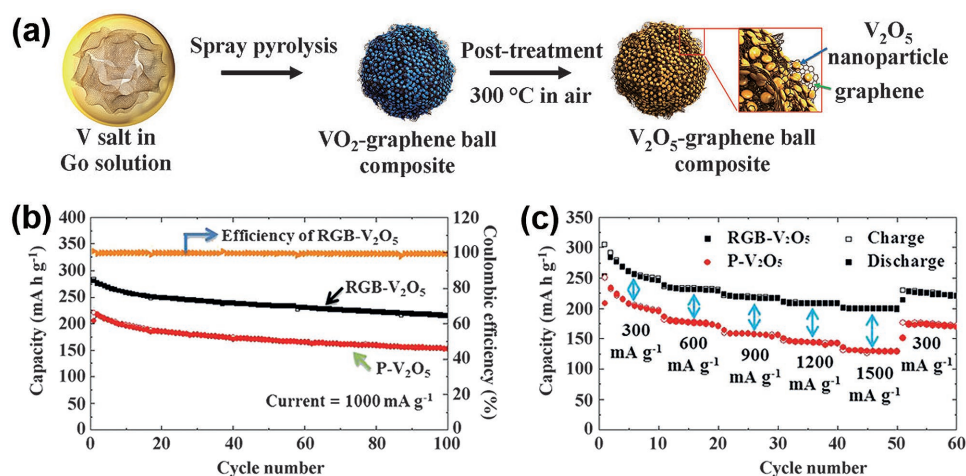MATERIALS
www.advenergymat.de

ADVANCED
SCIENCE NEWS
www.advancedsciencenews.com

REVIEW

Figure 34. a) Schematic diagram of formation mechanism of the reduced graphene oxide ball-V_2O_5 (RGB-V_2O_5) composite powder by spray pyrolysis, b) cycle performances and c) rate performances of RGB-V_2O_5composite and porous V_2O_5 (P-V_2O_5) powder. Reproduced with permission.[190] Copyright 2014, Wiley-VCH.

high first discharge capacity of 154 mA h g^{-1}.[196] In addition, Li_2MnSiO_4/carbon nanocomposites synthesized with the same procedure showed a first discharge capacity of 184 mA h g^{-1} at 0.05 C and 115 mA h g^{-1} at 1 C.[197] Furthermore, high temperature tests (60 °C) showed promising results: an initial discharge capacity of 225 mA h g^{-1} at 0.05 C. The same group also reported electrochemical performance results for different ratios of Fe and Mn in $Li_2Fe_xMn_{1-x}SiO_4$/carbon ($0 \leq x \leq 0.8$) nanocomposites.[198] Pure-phase $Li_2Fe_xMn_{1-x}SiO_4$ was prepared from a well-mixed precursor solution at the molecular level. The $Li_2Fe_{0.5}Mn_{0.5}SiO_4$/carbon nanocomposite cathode delivered a maximum discharge capacity of 149 mA h g^{-1} at 1C. The cyclability of the $Li_2Fe_xMn_{1-x}SiO_4$/carbon ($0 \leq x \leq 0.8$) nanocomposites was also enhanced by increasing the Fe content, indicating the importance of the TMs choice and their homogeneous distribution, for which SP was indeed beneficially adopted.

5. Electrode Materials for SIBs Prepared by SP

5.1. Anode Materials for SIBs Prepared by SP

Over the past few years, development of room temperature SIBs has regained battery community's attention mainly due to the lower cost of sodium compared with lithium.[47–51] Given the great similarity between LIBs and SIBs, many high capacity electrode materials for LIBs also found potential applications in SIBs, for example, Sn and some TM oxides. However, due to the larger atomic size of Na-ion compared with Li-ion (Shannon's ionic radius: 1.02 Å for Na$^+$ vs 0.76 Å for Li$^+$),[49] the charge-discharge induced volume changes are often much larger for the same materials used for sodium ion storage. Moreover, electrode materials of SIBs often exhibit poorer charge-discharge kinetics compared with LIBs. Thus, structural designs at electrode's particle-levelare more challenging and desired for high capacity electrode materials of SIBs to achieve satisfactory electrochemical performance. More robust structures, which can accommodate even larger volume fluctuation, form a

stable SEI film during cycling, and provide sufficient charge-discharge rate, should be developed for electrode materials of SIBs. SP has recently been utilized to prepare anode materials for SIBs.[199–201] For example, very recently, Chen's group has applied SP to synthesize Sn-C and CuO-C composites as anodes for SIBs. In both Sn-C and CuO-C composites,[200,201] nano-sized active materials (Sn and CuO, respectively) were finely embedded into the spherical carbon matrix, which can effectively alleviate the sodiation-desodiation induced stress, buffer the volume changes, and prevent aggregation of metals during electrochemical cycling. Consequently, both composites exhibited stable sodium storage behaviour for over 500 sodiation-desodiation cycles. With similar schemes, the decent cycling performance of Sb-C[202] and Fe_2O_3-C[203] were also reported. **Figure 36** displays the 3D porous structure (Figure 36a–f) and the sodium storage performance (Figure 36g,h) of the Fe_2O_3-C composite.[203] Besides these compounds, some sulfides and selenides also lately exhibited promising electrochemical performance as SIB anodes.[204–206]

5.2. Cathode Materials for SIBs Prepared by SP

In the status quo, SIBs cathode materials synthesized by SP are scarce due to the relative lack of research on SIBs compared with that of LIBs. However, several materials have been investigated, such as $Na_3V_2(PO_4)_3$/carbon, Na_2CoPO_4F, and $Na_{2/3}Fe_{1/3}Mn_{2/3}O_2$.[207–211] Our group recently introduced the scalable aerosol synthesis of $Na_3V_2(PO_4)_3$/carbon (NVP/C) porous hollow spheres as cathodes for SIBs. Stoichiometric amount of NH_4VO_3, $NH_4H_2PO_4$, Na_2CO_3, and citric acid were added in to a spray solution.[207] Citric acid has dual roles as a carbon precursor and a chelating agent within the aerosol droplet. For the aerosol spray process, the spray solution was loaded into a plastic syringe connected to a blunt-tip needle, which was connected to a syringe pump. The pyrolysis temperature was 600 °C, while the argon carrier gas flow rate was held constant at 3 mm L^{-1}. The as-collected particles were then annealed at
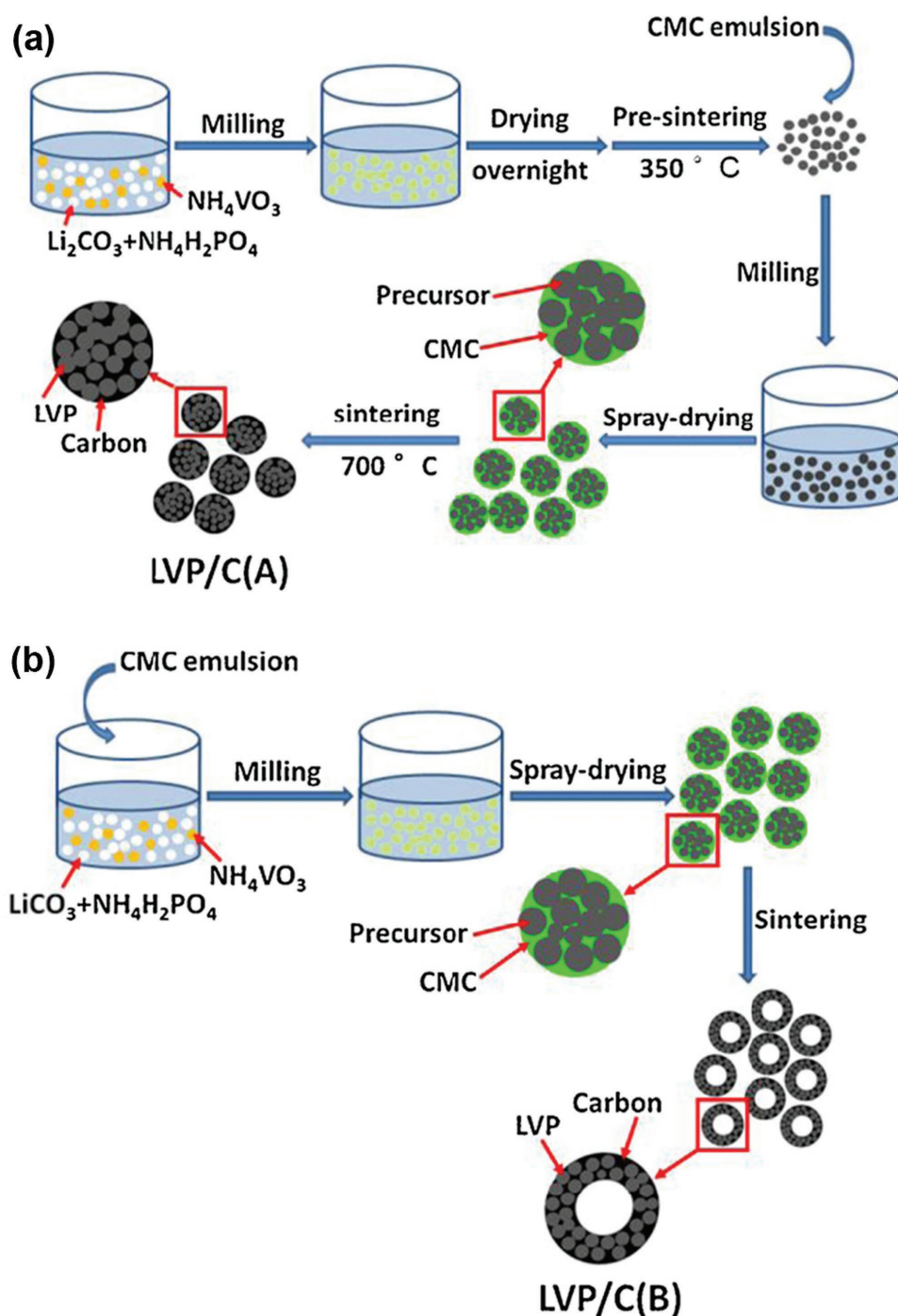
**ADVANCED
SCIENCE NEWS**

www.advancedsciencenews.com

**ADVANCED
ENERGY
MATERIALS**

www.advenergymat.de

REVIEW

Figure 35. A schematic illustration of synthesis process for a) dense structured $Li_3V_2(PO_4)_3$/carbon (LVP/C) (A) and b) hollow structured $Li_3V_2(PO_4)_3$/carbon (B). Reproduced with permission.[195] Copyright 2013, Elsevier Ltd.

800 °C for 3 h under argon atmosphere to obtain the crystalline NVP/C porous hollow spheres. The FE-SEM images in **Figure 37** show the non-aggregated, spherical NVP/C powder. Unfortunately, the mean particle size distribution is quite wide (2–10 µm), most likely due to the fact that the aerosol droplets are generated with random sizes from the needle. TEM characterization (Figure 37c,d) indicates that the NVP/C composites prepared via SP possess a porous structure. Also, HR-TEM

image (Figure 37d) confirms the existence of a 5 nm layer of amorphous carbon on the particle surface. The electrochemical performance tests of this material were conducted, the results of which are given in Figure 37e,f. For comparison, the same material prepared by sol-gel method was tested as well. Both samples have similar reversible capacities, but their cyclability differs significantly in the prolonged cycling period. The reversible capacities at the 300th cycle of NVP/C prepared by SP and
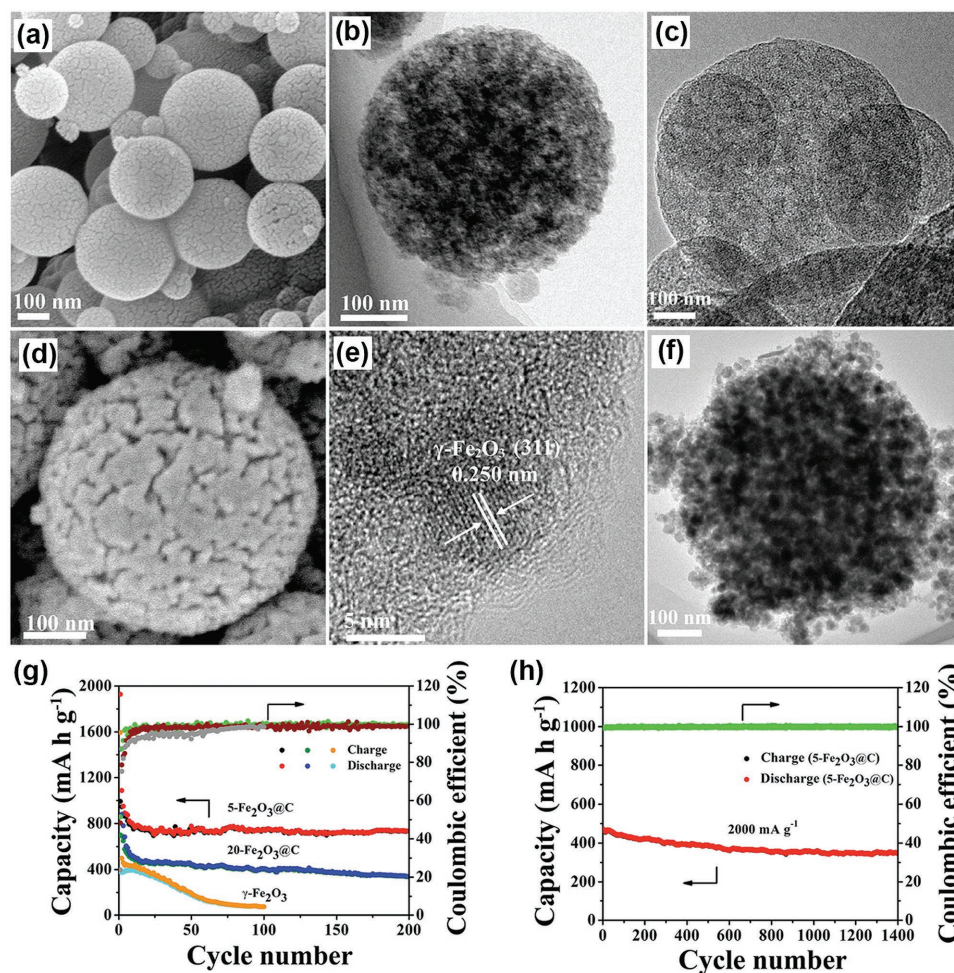
ADVANCED
ENERGY
MATERIALS
www.advenergymat.de

ADVANCED
SCIENCE NEWS
www.advancedsciencenews.com

REVIEW

Figure 36. 3D porous γ-Fe$_2$O$_3$@C nanocomposite for sodium ion batteries. a,b) SEM images, c–f) TEM images, g) cycle performances, and h) long-cycle performance. Reproduced with permission.[203] Copyright 2015, Wiley-VCH.

sol-gel method were 89.3 and 71.5 mA h g^{-1} at 20 mA g^{-1}, respectively (Figure 37e). The NVP/C prepared by SP also exhibited better rate capability (Figure 37f) compared to that prepared by sol-gel method. The distinct performance was elucidated by electrochemical impedance spectroscopy (EIS) measurements. It was found that before cycling, the charge transfer resistance (R_{ct}) of the aerosol cathode (264.5 Ω) is lower than that of the sol–gel cathode (310.8 Ω). The calculated sodium diffusion coefficient values for the aerosol and sol–gel cathodes are 2.79×10^{-16} and 2.35×10^{-16} cm^2 s^{-1}, respectively, indicating the faster Na$^+$ transport in the aerosol cathode. This work proved the merits of the SP process for facile synthesis of SIB electrode composites with better properties compared with those prepared by other processes. In addition to this investigation, carbon-coated hollow Na$_2$FePO$_4$F spheres and croconic acid disodium salt-reduced graphene oxide composites were successfully synthesized by SP and applied as SIB cathodes.[208,209]

Kodera et al. succeeded in synthesizing Na$_{2/3}$Fe$_{1/3}$Mn$_{2/3}$O$_2$ precursor powder via SP. This precursor powder was then annealed at temperatures of 700–1000 °C under air to enhance crystallinity.[210] The crystal phases of the calcined powder obtained from 800 to 1100 °C were P2-type

structures with the space group of P6$_3$/mmc. The discharge capacity of the P2-Na$_{2/3}$Fe$_{1/3}$Mn$_{2/3}$O$_2$ cathode was approximately 150 mA h g^{-1} at a rate of 0.1C in the voltage range from 1.5 to 4.0 V (vs Na/Na$^+$). The discharge capacity of the P2-Na$_{2/3}$Fe$_{1/3}$Mn$_{2/3}$O$_2$ cathode after 20 cycles was maintained at approximately 90% of the initial discharge capacity. In addition, a Na$_2$CoPO$_4$F/carbon composite was successfully synthesized by a spray-drying and high temperature sintering method for the first time by Zou et al.[211] Co(NO$_3$)$_2$·6H$_2$O ($\approx$0.02 mol) and citric acid ($\approx$0.02 mol) were first dissolved in 100 mL deionized water. Next, 0.04 mol of NaF and 0.02 mol of H$_3$PO$_4$ were added to the solution, followed by continuous stirring at 80 °C for another 16 h. By way of spray drying, precursor powder was synthesized, followed by heat treatment at 600 °C under a N$_2$ atmosphere. The final powder particles have particle sizes of approximately 20 μm. Na$_2$CoPO$_4$F in a Na half-cell can deliver a first discharge capacity of 107 mA h g^{-1} at a current density of 61 mA g^{-1}. Na$_2$CoPO$_4$F shows the highest working voltage at 4.3 V vs Na/Na$^+$, suggesting that Na$_2$CoPO$_4$F may be a good candidate for a high voltage SIB cathode.

Apparently, in contrast to the field of LIBs in which a wide variety of electrode materials were already fabricated via SP,
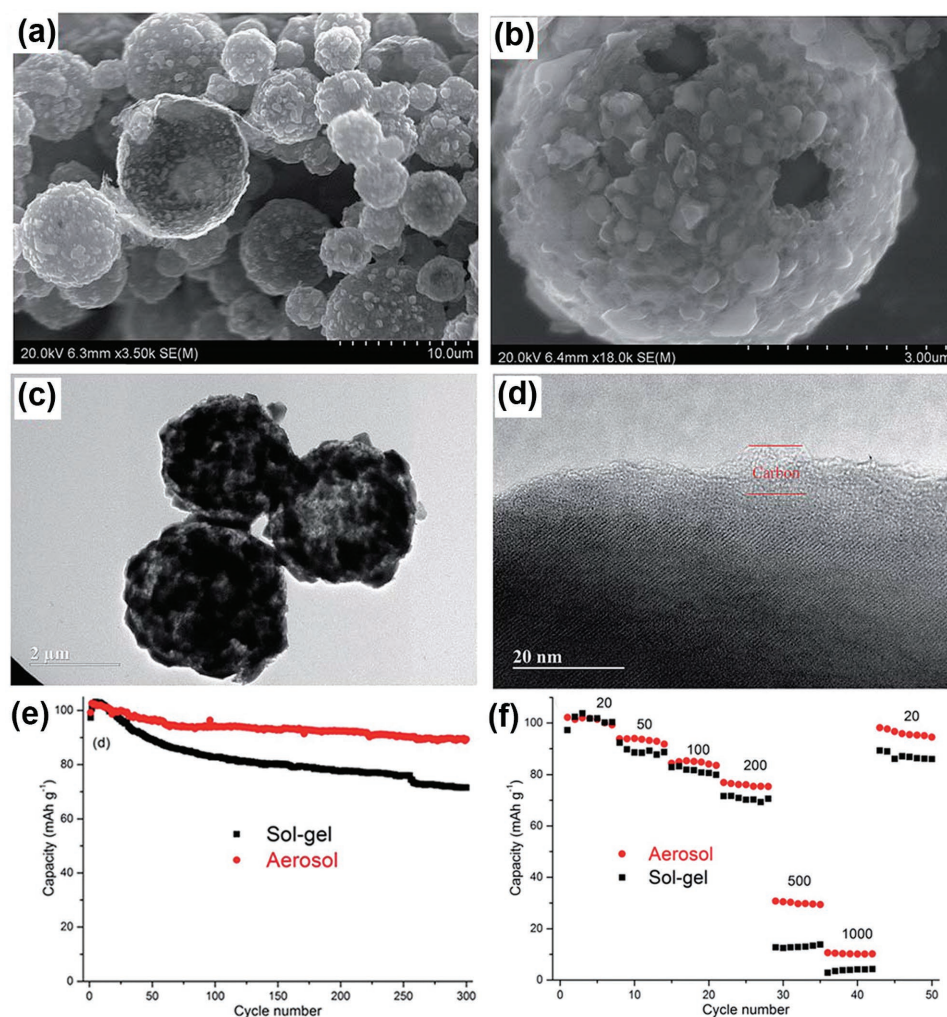
ADVANCED
SCIENCE NEWS
www.advancedsciencenews.com

ADVANCED
ENERGY
MATERIALS
www.advenergymat.de

REVIEW

Figure 37. a,b) SEM and c,d) TEM images of $Na_3V_2(PO_4)_3$/carbon composite prepared by SP. e) Cycle performances and f) rate performances of $Na_3V_2(PO_4)_3$/carbon composite prepared by SP and sol-gel processes. Reproduced with permission.[207] Copyright 2015, Royal Society of Chemistry.

the application of SP to prepare electrode materials for SIBs is just emerging. Therefore, there will be lots of opportunities to explore the powerfulness of SP in the field of SIBs.

6. Conclusions and Perspectives

In this review, we have introduced an industrially-viable synthetic method for electrode materials preparation, spray pyrolysis (SP), and summarized recent progress of advanced anode and cathode materials for LIBs and SIBs prepared via this method. We have summarized the composition, morphology, precursor solution, process parameters, and electrochemical performance for electrode materials of LIBs and SIBs prepared by using SP (Table S1 and S2, Supporting Information). As demonstrated above, SP is a powerful synthetic method and has the ability to generate a myriad of electrode materials with various structures. The main advantage of SP is that single or multicomponent particles can be formed rapidly, in a single step. One droplet = 1 particle. The rapid heating and cooling process associated with droplet formation and solvent evaporation can

"freeze" the precursor solid particles to create uniformly nanostructured particles. SP can generate microsized secondary particles by assembling uniform primary nanoparticles, thus allowing taking advantage of both dimensions within each particle. Moreover, the key parameters, including reactor temperature, residence time, droplet size distribution, and composition of the precursor solution, can be easily tuned to acquire desired properties (composition, morphology, porosity, particle size, stoichiometry, etc.) for electrode materials. Due to its flexibility and applicability, SP has been widely used to prepare high capacity anode and cathode materials for LIBs and SIBs, as presented above. The fast decomposition of organic and/or inorganic materials during SP will generate a large amount of gas, facilitating formation of materials with porous structures. These porous structures turned out to greatly benefit the electrochemical performance of high capacity electrode materials, especially anode materials, which usually undergo large volume changes during reactions with Li and Na ions. On the other hand, SP' unique feature, which is able to form homogenous TMs mixing and spontaneous core-shell formation, is exceptionally advantageous for cathode materials whose purity and
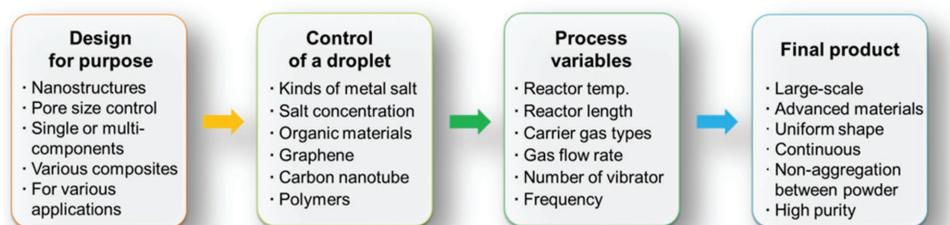
ADVANCED
ENERGY
MATERIALS
www.advenergymat.de

ADVANCED
SCIENCE NEWS
www.advancedsciencenews.com

REVIEW

Figure 38. Design procedures for large-scale synthesis via SP process.

crystallinity are critical for their performance. **Figure 38** shows the typical design procedures for SP. In principle, any electrode materials can be synthesized through SP if appropriate precursor solution and process parameters can be found. Besides the materials discussed herein, SP processes have been adopted for lithium-sulfur (Li-S) and metal-air batteries. In particular, SP's unique capability of generating hierarchical structures where key elements, such as sulfur active materials and oxygen evolution catalysts, are uniformly embedded in 3D porous frameworks can play a critical role in addressing the chronic issues of such emerging battery systems.[212–218]

SP or spray drying shows good compatibility which allows this method to be integrated into other synthetic methods to produce materials with unique structures, as recently demonstrated by our group that a high performance 3D Si-C fiber paper anode for LIBs was generated by combining electrospray and electrospinning techniques.[219] Also, SP is able to combine the material synthesis and electrode preparation into a single step, as reported by García-Tamayo et al.[97] who fabricated a Fe_2O_3 composite electrode through electrostatic SP.

All in all, SP and spray drying have found many applications for preparing electrode materials for LIBs and SIBs mainly due to its ability to rationally design structures of materials and to produce tons of materials per day. However, there are still some challenges and room for further improvement. First, it is difficult to precisely control some properties of final products of SP, for example the structure and distribution of empty space, which are critical for high capacity electrode materials undergoing large volume fluctuation upon cycling, since these properties can be affected by a number of factors, such as precursor solution, atomization techniques, temperature of pyrolysis, and residence time in heat source, etc. Furthermore, during pyrolysis, a series of complicated physical and chemical processes sequentially or simultaneously take place, which make the properties control even more difficult. Therefore, future efforts should be focused on investigating the reaction mechanisms during pyrolysis, both experimentally and theoretically. Ideal condition is that the empty space is just enough to accommodate the volume changes without sacrificing the volumetric energy density of batteries, and meanwhile for anode materials, under the premise of sufficient charge-discharge rate, it is important to keep the majority of pores inaccessible to electrolyte, thus providing a high 1st Coulombic efficiency. Second, some precursor solutions consist of costly salts and solvents, which are industrially unsuitable. Hence, for practical applications, it is necessary to explore more economical starting materials, gas and evaporated solvents generated by SP has to be

appropriately disposed of. For example, some SP processes particularly those starting with nitrate salts can lead to gas emissions (e.g., NO_x) that under some circumstances might require mitigation to fulfill emissions regulations. In future, a recycling system might be established to reuse the heat energy and materials in the exhaust gas.

Supporting Information

Supporting Information is available from the Wiley Online Library or from the author.

Acknowledgements

[1] K. Ozawa, *Solid State Ionics* **1994**, *69*, 212.
[2] S. G. Chalk, J. F. Miller, *J. Power Sources* **2006**, *159*, 73.
[3] J.-M. Tarascon, M. Armand, *Nature* **2001**, *414*, 359.
[4] M. S. Whittingham, *Chem. Rev.* **2014**, *114*, 11414.
[5] A. Manthiram, Y. Fu, S.-H. Chung, C. Zu, Y.-S. Su, *Chem. Rev.* **2014**, *114*, 11751.
[6] M. N. Obrovac, V. L. Chevrier, *Chem. Rev.* **2014**, *114*, 11444.
[7] X. Ji, K. T. Lee, L. F. Nazar, *Nat. Mater.* **2009**, *8*, 500.
[8] Y.-K. Sun, S.-T. Myung, B.-C. Park, J. Prakash, I. Belharouak, K. Amine, *Nat. Mater.* **2009**, *8*, 320.
[9] C. K. Chan, H. Peng, G. Liu, K. Mcilwrath, X. F. Zhang, R. A. Huggins, Y. Cui, *Nat. Nanotechnol.* **2008**, *3*, 31.
[10] J. Maier, *Angew. Chemie - Int. Ed.* **2013**, *52*, 4998.
[11] P. G. Bruce, B. Scrosati, J.-M. Tarascon, *Angew. Chemie Int. Ed.* **2008**, *47*, 2930.
[12] A. Magasinski, P. Dixon, B. Hertzberg, A. Kvit, J. Ayala, G. Yushin, *Nat. Mater.* **2010**, *9*, 353.
[13] N. Liu, Z. Lu, J. Zhao, M. T. McDowell, H.-W. Lee, W. Zhao, Y. Cui, *Nat. Nanotechnol.* **2014**, *9*, 187.

**ADVANCED
SCIENCE NEWS**

www.advancedsciencenews.com

**ADVANCED
ENERGY
MATERIALS**

www.advenergymat.de

REVIEW

[14] H. Wu, G. Chan, J. W. Choi, I. Ryu, Y. Yao, M. T. McDowell, S. W. Lee, A. Jackson, Y. Yang, L. Hu, Y. Cui, *Nat. Nanotechnol.* **2012**, *7*, 310.

[15] M. Winter, R. J. Brodd, *Chem. Rev.* **2004**, *104*, 4245.

[16] M. S. Whittingham, *Chem. Rev.* **2004**, *104*, 4271.

[17] J. Reed, G. Ceder, *Chem. Rev.* **2004**, *104*, 4513.

[18] J. W. Long, B. Dunn, D. R. Rolison, H. S. White, *Chem. Rev.* **2004**, *104*, 4463.

[19] A. S. Aricò, P. Bruce, B. Scrosati, J.-M. Tarascon, W. Van Schalkwijk, *Nat. Mater.* **2005**, *4*, 366.

[20] U. Kasavajjula, C. Wang, A. J. Appleby, *J. Power Sources* **2007**, *163*, 1003.

[21] Y. Wang, G. Cao, *Adv. Mater.* **2008**, *20*, 2251.

[22] H. Li, Z. Wang, L. Chen, X. Huang, *Adv. Mater.* **2009**, *21*, 4593.

[23] M. R. Palacín, *Chem. Soc. Rev.* **2009**, *38*, 2565.

[24] J. W. Fergus, *J. Power Sources* **2010**, *195*, 939.

[25] B. Scrosati, J. Garche, *J. Power Sources* **2010**, *195*, 2419.

[26] C. Liu, F. Li, L.-P. Ma, H.-M. Cheng, *Adv. Energy Mater.* **2010**, *22*, E28.

[27] L. Ji, Z. Lin, M. Alcoutlabi, X. Zhang, *Energy Environ. Sci.* **2011**, *4*, 2682.

[28] W.-J. Zhang, *J. Power Sources* **2011**, *196*, 13.

[29] J. B. Goodenough, K.-S. Park, *J. Am. Chem. Soc.* **2013**, *135*, 1167.

[30] J. Chen, *Recent Pat. Nanotechnol.* **2013**, *7*, 2.

[31] D. Larcher, J.-M. Tarascon, *Nat. Chem.* **2014**, *7*, 19.

[32] M. Ge, X. Fang, J. Rong, C. Zhou, *Nanotechnology* **2013**, *24*, 422001.

[33] C. Yuan, H. B. Wu, Y. Xie, X. W. Lou, *Angew. Chemie Int. Ed.* **2014**, *53*, 1488.

[34] H. Li, H. Zhou, *Chem. Commun.* **2012**, *48*, 1201.

[35] S. Balaji, D. Mutharasu, N. S. Subramanian, K. Ramanathan, *Ionics (Kiel).* **2009**, *15*, 765.

[36] D. Jugović, D. Uskoković, *J. Power Sources* **2009**, *190*, 538.

[37] P. S. Patil, *Mater. Chem. Phys.* **1999**, *59*, 185.

[38] A. B. D. Nandiyanto, K. Okuyama, *Adv. Powder Technol.* **2011**, *22*, 1.

[39] N. E. Motl, A. K. P. Mann, S. E. Skrabalak, *J. Mater. Chem. A* **2013**, *1*, 5193.

[40] D. S. Jung, S. B. Park, Y. C. Kang, *Korean J. Chem. Eng.* **2010**, *27*, 1621.

[41] D. Perednis, L. J. Gauckler, *Solid State Ionics* **2004**, *166*, 229.

[42] D. Li, H. Haneda, S. Hishita, N. Ohashi, N. K. Labhsetwar, *J. Fluor. Chem.* **2005**, *126*, 69.

[43] J. Hao, S. A. Studenikin, M. Cocivera, *J. Lumin.* **2001**, *93*, 313.

[44] V. R. Shinde, T. P. Gujar, C. D. Lokhande, *Sensors Actuators B* **2007**, *120*, 551.

[45] M. Honda, Y. Kawanobe, K. Ishii, T. Konishi, M. Mizumoto, N. Kanzawa, M. Matsumoto, M. Aizawa, *Mater. Sci. Eng. C* **2013**, *33*, 5008.

[46] D. S. Jung, Y. N. Ko, Y. C. Kang, S. Bin Park, *Adv. Powder Technol.* **2014**, *25*, 18.

[47] H. Pan, Y.-S. Hu, L. Chen, *Energy Environ. Sci.* **2013**, *6*, 2338.

[48] V. Palomares, P. Serras, I. Villaluenga, K. B. Hueso, J. Carretero-González, T. Rojo, *Energy Environ. Sci.* **2012**, *5*, 5884.

[49] N. Yabuuchi, K. Kubota, M. Dahbi, S. Komaba, *Chem. Rev.* **2014**, *114*, 11636.

[50] S.-W. Kim, D.-H. Seo, X. Ma, G. Ceder, K. Kang, *Adv. Energy Mater.* **2012**, *2*, 710.

[51] D. Kundu, E. Talaie, V. Duffort, L. F. Nazar, *Angew. Chemie Int. Ed.* **2015**, *54*, 2.

[52] J. H. Bang, K. S. Suslick, *Adv. Mater.* **2010**, *22*, 1039.

[53] T. T. Kodas, M. J. Hampden-Smith, *Aerosol Processing of Materials* **1998**.

[54] J. B. Mooney, S. B. Radding, *Annu. Rev. Mater. Sci.* **1982**, *12*, 81.

[55] R. W. Wood, A. L. Loomis, *Philos. Mag.* **1927**, *4*, 417.

[56] W. H. Suh, K. S. Suslick, *J. Am. Chem. Soc.* **2005**, *127*, 12007.

[57] R. J. Lang, *J. Acoust. Soc. Am.* **1962**, *34*, 6.

[58] P. D. Hede, P. Bach, A. D. Jensen, *Chem. Eng. Sci.* **2008**, *63*, 3821.

[59] R. J. Schick, *Spray Technology Reference Guide: Understanding Drop Size* **2006**.

[60] A. Jaworek, A. T. Sobczyk, *J. Electrostat.* **2008**, *66*, 197.

[61] A. Jaworek, *Powder Technol.* **2007**, *176*, 18.

[62] a. Aguilar-Elguézabal, W. Antúnez, G. Alonso, F. P. Delgado, F. Espinosa, M. Miki-Yoshida, *Diam. Relat. Mater.* **2006**, *15*, 1329.

[63] S. E. Skrabalak, K. S. Suslick, *J. Am. Chem. Soc.* **2006**, *128*, 12642.

[64] H. Xu, J. Guo, K. S. Suslick, *Adv. Mater.* **2012**, *24*, 6028.

[65] T. Doi, A. Fukuda, Y. Iriyama, T. Abe, Z. Ogumi, K. Nakagawa, T. Ando, *Electrochem. Commun.* **2005**, *7*, 10.

[66] G. Zhou, D.-W. Wang, X. Shan, N. Li, F. Li, H.-M. Cheng, *J. Mater. Chem.* **2012**, *22*, 11252.

[67] J. Yang, Q. Liao, X. Zhou, X. Liu, J. Tang, *RSC Adv.* **2013**, *3*, 16449.

[68] E. J. Yoo, J. Kim, E. Hosono, H. S. Zhou, T. Kudo, I. Honma, *Nano Lett.* **2008**, *8*, 2277.

[69] P. Guo, H. Song, X. Chen, *Electrochem. Commun.* **2009**, *11*, 1320.

[70] G. Wang, X. Shen, J. Yao, J. Park, *Carbon N. Y.* **2009**, *47*, 2049.

[71] D. Pan, S. Wang, B. Zhao, M. Wu, H. Zhang, Y. Wang, Z. Jiao, *Chem. Mater.* **2009**, *21*, 3136.

[72] P. Lian, X. Zhu, S. Liang, Z. Li, W. Yang, H. Wang, *Electrochim. Acta* **2010**, *55*, 3909.

[73] H. F. Xiang, Z. D. Li, K. Xie, J. Z. Jiang, J. J. Chen, P. C. Lian, J. S. Wu, Y. Yu, H. H. Wang, *RSC Adv.* **2012**, *2*, 6792.

[74] S.-H. Ng, J. Wang, D. Wexler, K. Konstantinov, Z.-P. Guo, H.-K. Liu, *Angew. Chemie - Int. Ed.* **2006**, *45*, 6896.

[75] S. H. Ng, J. Wang, D. Wexler, S. Y. Chew, H. K. Liu, *J. Phys. Chem. C* **2007**, *111*, 11131.

[76] S. H. Ng, J. Wang, K. Konstantinov, D. Wexler, S. Y. Chew, Z. P. Guo, H. K. Liu, *J. Power Sources* **2007**, *174*, 823.

[77] J. Lai, H. Guo, Z. Wang, X. Li, X. Zhang, F. Wu, P. Yue, *J. Alloys Compd.* **2012**, *530*, 30.

[78] D. S. Jung, T. H. Hwang, S. B. Park, J. W. Choi, *Nano Lett.* **2013**, *13*, 2092.

[79] J. Luo, X. Zhao, J. Wu, H. D. Jang, H. H. Kung, J. Huang, *J. Phys. Chem. Lett.* **2012**, *3*, 1824.

[80] Y. Wen, Y. Zhu, A. Langrock, A. Manivannan, S. H. Ehrman, C. Wang, *Small* **2013**, *9*, 2810.

[81] S. Choi, D. S. Jung, J. W. Choi, *Nano Lett* **2014**, *14*, 7120.

[82] Z. Yang, J. Guo, S. Xu, Y. Yu, H. D. Abruña, L. A. Archer, *Electrochem. Commun.* **2013**, *28*, 40.

[83] M. Winter, J. O. Besenhard, *Electrochim. Acta* **1999**, *45*, 31.

[84] M. Valvo, U. Lafont, L. Simonin, E. M. Kelder, *J. Power Sources* **2007**, *174*, 428.

[85] S. H. Ju, H. C. Jang, Y. C. Kang, D. W. Kim, *J. Alloys Compd.* **2009**, *478*, 177.

[86] R. Zheng, X. Meng, F. Tang, Z. Lin, J. Ren, *J. Phys. Chem. C* **2009**, *113*, 13065.

[87] Y. Xu, Q. Liu, Y. Zhu, Y. Liu, A. Langrock, M. R. Zachariah, C. Wang, *Nano Lett.* **2013**, *13*, 470.

[88] J. Guo, Z. Yang, L. A. Archer, *J. Mater. Chem. A* **2013**, *1*, 8710.

[89] T.-F. Yi, S.-Y. Yang, Y. Xie, *J. Mater. Chem. A* **2015**, *3*, 5750.

[90] T. Doi, Y. Iriyama, T. Abe, Z. Ogumi, *Chem. Mater.* **2005**, *17*, 1580.

[91] S. H. Ju, Y. C. Kang, *J. Phys. Chem. Solids* **2009**, *70*, 40.

[92] S. H. Ju, Y. C. Kang, *J. Power Sources* **2009**, *189*, 185.

[93] S. H. Ju, Y. C. Kang, *J. Power Sources* **2010**, *195*, 4327.

[94] Q. Zhang, W. Peng, Z. Wang, X. Li, X. Xiong, H. Guo, Z. Wang, F. Wu, *Solid State Ionics* **2013**, *236*, 30.

[95] S.-L. Chou, J.-Z. Wang, D. Wexler, K. Konstantinov, C. Zhong, H.-K. Liu, S.-X. Dou, *J. Mater. Chem.* **2010**, *20*, 2092.

[96] S.-L. Chou, J.-Z. Wang, Z.-X. Chen, H.-K. Liu, S.-X. Dou, *Nanotechnology* **2011**, *22*, 265401.

ADVANCED
ENERGY
MATERIALS

www.advenergymat.de

ADVANCED
SCIENCE NEWS

www.advancedsciencenews.com

REVIEW

[97] E. García-Tamayo, M. Valvo, U. Lafont, C. Locati, D. Munao, E. M. Kelder, *J. Power Sources* **2011**, *196*, 6425.

[98] M. Y. Son, Y. J. Hong, J.-K. Lee, Y. C. Kang, *Nanoscale* **2013**, *5*, 11592.

[99] Y. Xu, G. Jian, Y. Liu, Y. Zhu, M. R. Zachariah, C. Wang, *Nano Energy* **2014**, *3*, 26.

[100] S. H. Choi, Y. C. Kang, *Carbon N. Y.* **2014**, *79*, 58.

[101] S. A. Needham, G. X. Wang, K. Konstantinov, Y. Tournayre, Z. Lao, H. K. Liu, *Electrochem. Solid-State Lett.* **2006**, *9*, A315.

[102] M. Y. Son, J. H. Kim, Y. C. Kang, *Electrochim. Acta* **2014**, *116*, 44.

[103] M. M. Rahman, S.-L. Chou, C. Zhong, J.-Z. Wang, D. Wexler, H.-K. Liu, *Solid State Ionics* **2010**, *180*, 1646.

[104] C. Zhong, J.-Z. Wang, S.-L. Chou, K. Konstantinov, M. Rahman, H.-K. Liu, *J. Appl. Electrochem.* **2010**, *40*, 1415.

[105] S. H. Choi, Y. C. Kang, *ACS Appl. Mater. Interfaces* **2014**, *6*, 2312.

[106] S. H. Choi, Y. N. Ko, J.-K. Lee, Y. C. Kang, *Sci. Rep.* **2014**, *4*, 5786.

[107] J. Y. Huang, L. Zhong, C. M. Wang, J. P. Sullivan, W. Xu, L. Q. Zhang, S. X. Mao, N. S. Hudak, X. H. Liu, A. Subramanian, H. Fan, L. Qi, A. Kushima, J. Li, *Science* **2010**, *80*, 1515.

[108] H. Huang, E. Kelder, L. Chen, J. Schoonman, *J. Power Sources* **1999**, *81–82*, 362.

[109] R. Ayouchi, F. Martin, J. R. Ramos Barrado, M. Martos, J. Morales, L. Sánchez, *J. Power Sources* **2000**, *87*, 106.

[110] M. Mohamedi, S.-J. Lee, D. Takahashi, M. Nishizawa, T. Itoh, I. Uchida, *Electrochim. Acta* **2001**, *46*, 1161.

[111] L. Yuan, Z. P. Guo, K. Konstantinov, J. Z. Wang, H. K. Liu, *Electrochim. Acta* **2006**, *51*, 3680.

[112] L. Yuan, Z. P. Guo, K. Konstantinov, H. K. Liu, S. X. Dou, *J. Power Sources* **2006**, *159*, 345.

[113] L. Yuan, J. Wang, S. Y. Chew, J. Chen, Z. P. Guo, L. Zhao, K. Konstantinov, H. K. Liu, *J. Power Sources* **2007**, *174*, 1183.

[114] Y. J. Hong, M. Y. Son, Y. C. Kang, *Adv. Mater.* **2013**, *25*, 2279.

[115] S. H. Choi, Y. C. Kang, *Nanoscale* **2013**, *5*, 4662.

[116] J. Morales, L. Sánchez, F. Martín, J. R. Ramos-Barrado, M. Sánchez, *Thin Solid Films* **2005**, *474*, 133.

[117] S. H. Choi, Y. C. Kang, *Chem. - A Eur. J.* **2014**, *20*, 3014.

[118] K. Konstantinov, S. H. Ng, J. Z. Wang, G. X. Wang, D. Wexler, H. K. Liu, *J. Power Sources* **2006**, *159*, 241.

[119] M. Martos, J. Morales, L. Sánchez, R. Ayouchi, D. Leinen, F. Martin, J. R. R. Barrado, *Electrochim. Acta* **2001**, *46*, 2939.

[120] S. H. Ng, J. Wang, K. Konstantinov, D. Wexler, J. Chen, H. K. Liu, *J. Electrochem. Soc.* **2006**, *153*, A787.

[121] M. H. Kim, Y. J. Hong, Y. C. Kang, *RSC Adv.* **2013**, *3*, 13110.

[122] S. M. Lee, S. H. Choi, J.-K. Lee, Y. C. Kang, *Electrochim. Acta* **2014**, *132*, 441.

[123] J. Guo, Q. Liu, C. Wang, M. R. Zachariah, *Adv. Funct. Mater.* **2012**, *22*, 803.

[124] Y. N. Ko, S. B. Park, S. H. Choi, Y. C. Kang, *Sci. Rep.* **2014**, *4*, 5751.

[125] W. Cho, J. H. Song, J.-H. Kim, G. Jeong, E. Y. Lee, Y.-J. Kim, *J. Appl. Electrochem.* **2012**, *42*, 909.

[126] Y. N. Ko, S. B. Park, K. Y. Jung, Y. C. Kang, *Nano Lett.* **2013**, *13*, 5462.

[127] C. H. Chen, A. A. J. Buysman, E. M. Kelder, J. Schoonman, *Solid State Ionics* **1995**, *80*, 1.

[128] Y. Li, C. Wan, Y. Wu, C. Jiang, Y. Zhu, *J. Power Sources* **2000**, *85*, 294.

[129] S. H. Kim, C.-S. Kim, *J. Electroceramics* **2008**, *23*, 254.

[130] S. H. Choi, J. H. Kim, Y. N. Ko, K. M. Yang, Y. C. Kang, *J. Power Sources* **2013**, *244*, 129.

[131] D. Y. Kim, S. H. Ju, Y. C. Kang, *Mater. Res. Bull.* **2007**, *42*, 362.

[132] H. Jang, C. Seong, Y. Suh, H. Kim, C. Lee, *Aerosol Sci. Technol.* **2004**, *38*, 1027.

[133] W. Liu, P. Oh, X. Liu, M.-J. Lee, W. Cho, S. Chae, Y. Kim, J. Cho, *Angew. Chemie Int. Ed.* **2015**, *54*, 4440.

[134] A. Manthiram, J. C. Knight, S.-T. Myung, S.-M. Oh, Y.-K. Sun, *Adv. Energy Mater.* **2016**, *6*, 1501010.

[135] A. S. Song, S. B. Park, J. Han, *Jpn. J. Appl. Phys.* **2012**, *51*, 105202.

[136] S. H. Ju, H. C. Jang, Y. C. Kang, *Electrochim. Acta* **2007**, *52*, 7286.

[137] H. Gao, Z. Zhang, Y. Lai, J. Li, Y. Liu, *J. Cent. South Univ. Technol. (Engl. Ed.)* **2008**, *15*, 830.

[138] S. W. Oh, S. H. Park, C.-W. Park, Y.-K. Sun, *Solid State Ionics* **2004**, *171*, 167.

[139] S. H. Park, C. S. Yoon, S. G. Kang, H.-S. Kim, S.-I. Moon, Y.-K. Sun, *Electrochim. Acta* **2004**, *49*, 557.

[140] S. K. Hu, G. H. Cheng, M. Y. Cheng, B. J. Hwang, R. Santhanam, *J. Power Sources* **2009**, *188*, 564.

[141] S.-H. Park, S. W. Oh, Y.-K. Sun, *J. Power Sources* **2005**, *146*, 622.

[142] M. Shui, S. Gao, J. Shu, W. Zheng, D. Xu, L. Chen, L. Feng, Y. Ren, *Ionics (Kiel)*. **2012**, *19*, 47.

[143] H.-C. Wu, Z.-Z. Guo, M.-H. Yang, C.-H. Lu, T.-Y. Wu, I. Taniguchi, *Chem. Lett.* **2005**, *34*, 1398.

[144] S. K. Kim, W. T. Jeong, H. K. Lee, J. Shim, *Int. J. Electrochem. Sci.* **2008**, *3*, 1504.

[145] J. H. Kim, J. H. Yi, Y. N. Ko, Y. C. Kang, *Mater. Chem. Phys.* **2012**, *134*, 254.

[146] K. Matsuda, I. Taniguchi, *J. Power Sources* **2004**, *132*, 156.

[147] C. M. Sim, S. H. Choi, Y. C. Kang, *Chem. Commun.* **2013**, *49*, 5978.

[148] S. H. Choi, J. H. Kim, Y. N. Ko, Y. J. Hong, Y. C. Kang, *J. Power Sources* **2012**, *210*, 110.

[149] M. Lee, S. Lee, P. Oh, Y. Kim, J. Cho, *Nano Lett* **2013**, *14*, 903.

[150] I. Taniguchi, N. Fukuda, M. Konarova, *Powder Technol.* **2008**, *181*, 228.

[151] C.-H. Lu, T.-Y. Wu, H.-C. Wu, M.-H. Yang, Z.-Z. Guo, I. Taniguchi, *Mater. Chem. Phys.* **2008**, *112*, 115.

[152] S.-H. Park, Y.-K. Sun, *Electrochim. Acta* **2004**, *50*, 431.

[153] S. H. Choi, Y. J. Hong, Y. C. Kang, *Nanoscale* **2013**, *5*, 7867.

[154] Z. Bakenov, I. Taniguchi, *Solid State Ionics* **2005**, *176*, 1027.

[155] I. Taniguchi, D. Song, M. Wakihara, *J. Power Sources* **2002**, *109*, 333.

[156] I. Taniguchi, *Mater. Chem. Phys.* **2005**, *92*, 172.

[157] L. Zhang, T. Yabu, I. Taniguchi, *Mater. Res. Bull.* **2009**, *44*, 707.

[158] S.-H. Park, S.-W. Oh, S.-T. Myung, Y.-K. Sun, *Electrochem. Solid-State Lett.* **2004**, *7*, A451.

[159] J. Liu, T. E. Conry, X. Song, M. M. Doeff, T. J. Richardson, *Energy Environ. Sci.* **2011**, *4*, 885.

[160] K. Konstantinov, S. Bewlay, G. Wang, M. Lindsay, J. Wang, H. Liu, S. Dou, J. Ahn, *Electrochim. Acta* **2004**, *50*, 421.

[161] F. Yu, J.-J. Zhang, Y.-F. Yang, G.-Z. Song, *J. Mater. Chem.* **2009**, *19*, 9121.

[162] S. L. Bewlay, K. Konstantinov, G. X. Wang, S. X. Dou, H. K. Liu, *Mater. Lett.* **2004**, *58*, 1788.

[163] F. Yu, J. Zhang, Y. Yang, G. Song, *J. Power Sources* **2010**, *195*, 6873.

[164] M.-R. Yang, T.-H. Teng, S.-H. Wu, *J. Power Sources* **2006**, *159*, 307.

[165] F. Yu, J. Zhang, Y. Yang, G. Song, *J. Power Sources* **2009**, *189*, 794.

[166] M. Konarova, I. Taniguchi, *J. Power Sources* **2010**, *195*, 3661.

[167] X. Zhou, F. Wang, Y. Zhu, Z. Liu, *J. Mater. Chem.* **2011**, *21*, 3353.

[168] W. Luo, L. Wen, H. Luo, R. Song, Y. Zhai, C. Liu, F. Li, *New Carbon Mater.* **2014**, *29*, 287.

[169] M. Konarova, I. Taniguchi, *Powder Technol.* **2009**, *191*, 111.

[170] W. Liu, P. Gao, Y. Mi, J. Chen, H. Zhou, X. Zhang, *J. Mater. Chem. A* **2013**, *1*, 2411.

[171] S.-M. Oh, S.-W. Oh, C.-S. Yoon, B. Scrosati, K. Amine, Y.-K. Sun, *Adv. Funct. Mater.* **2010**, *20*, 3260.

[172] T. N. L. Doan, I. Taniguchi, *J. Power Sources* **2011**, *196*, 5679.

[173] T. N. L. Doan, I. Taniguchi, *J. Power Sources* **2011**, *196*, 1399.

[174] Z. Bakenov, I. Taniguchi, *Electrochem. Commun.* **2010**, *12*, 75.

[175] S. M. Oh, S. W. Oh, S. T. Myung, S. M. Lee, Y. K. Sun, *J. Alloys Compd.* **2010**, *506*, 372.

[176] T. N. L. Doan, I. Taniguchi, *Powder Technol.* **2012**, *217*, 574.

**ADVANCED
SCIENCE NEWS**

www.advancedsciencenews.com

**ADVANCED
ENERGY
MATERIALS**

www.advenergymat.de

REVIEW

[177] I. Taniguchi, T. N. L. Doan, B. Shao, *Electrochim. Acta* **2011**, *56*, 7680.

[178] S. Akimoto, I. Taniguchi, *J. Power Sources* **2013**, *242*, 627.

[179] M. Lengyel, X. Zhang, G. Atlas, H. L. Bretscher, I. Belharouak, R. L. Axelbaum, *J. Electrochem. Soc.* **2014**, *161*, A1338.

[180] P. Oh, M. Ko, S. Myeong, Y. Kim, J. Cho, *Adv. Energy Mater.* **2014**, *4*, 1400631.

[181] S. N. Lim, W. Ahn, S.-H. Yeon, S. Bin Park, *Chem. Asian J.* **2014**, *9*, 2946.

[182] M. Y. Son, Y. J. Hong, S. H. Choi, Y. C. Kang, *Electrochim. Acta* **2013**, *103*, 110.

[183] X. Zhang, R. L. Axelbaum, *J. Electrochem. Soc.* **2012**, *159*, A834.

[184] M. Y. Son, J.-K. Lee, Y. C. Kang, *Sci. Rep.* **2014**, *4*, 5752.

[185] Y. N. Ko, J. H. Kim, S. H. Choi, Y. C. Kang, *J. Power Sources* **2012**, *211*, 84.

[186] S. Lin, B. Shao, I. Taniguchi, *Mater. Res. Bull.* **2014**, *49*, 291.

[187] Y. N. Ko, S. H. Choi, Y. C. Kang, S. B. Park, *ACS Appl. Mater. Interfaces* **2013**, *5*, 3234.

[188] Y. N. Ko, Y. C. Kang, S. B. Park, *Nanoscale* **2013**, *5*, 8899.

[189] S. H. Choi, Y. C. Kang, *Chem. - A Eur. J.* **2013**, *19*, 17305.

[190] S. H. Choi, Y. C. Kang, *Chem. - A Eur. J.* **2014**, *20*, 6294.

[191] X. Jia, L. Zhang, R. Zhang, Y. Lu, F. Wei, *RSC Adv.* **2014**, *4*, 21018.

[192] N. Tran, K. G. Bramnik, H. Hibst, J. Prölß, N. Mronga, M. Holzapfel, W. Scheifele, P. Novák, *J. Electrochem. Soc.* **2008**, *155*, A384.

[193] X. Xiong, Z. Wang, H. Guo, X. Li, F. Wu, P. Yue, *Electrochim. Acta* **2012**, *71*, 206.

[194] Y. N. Ko, H. Y. Koo, J. H. Kim, J. H. Yi, Y. C. Kang, J.-H. Lee, *J. Power Sources* **2011**, *196*, 6682.

[195] L.-L. Zhang, G. Peng, G. Liang, P.-C. Zhang, Z.-H. Wang, Y. Jiang, Y.-H. Huang, H. Lin, *Electrochim. Acta* **2013**, *90*, 433.

[196] H. Nagano, I. Taniguchi, *J. Power Sources* **2015**, *298*, 280.

[197] M. Hasumi, I. Taniguchi, *Mater. Lett.* **2014**, *134*, 202.

[198] B. Shao, Y. Abe, I. Taniguchi, *Powder Technol.* **2013**, *235*, 1.

[199] S. H. Choi, Y. C. Kang, *Nano Res.* **2015**, *8*, 1595.

[200] Y. Liu, N. Zhang, L. Jiao, Z. Tao, J. Chen, *Adv. Funct. Mater.* **2015**, *25*, 214.

[201] Y. Lu, N. Zhang, Q. Zhao, J. Liang, J. Chen, *Nanoscale* **2015**, *7*, 2770.

[202] N. Zhang, Y. Liu, Y. Lu, X. Han, F. Cheng, J. Chen, *Nano Res.* **2015**, *8*, 3384.

[203] N. Zhang, X. Han, Y. Liu, X. Hu, Q. Zhao, J. Chen, *Adv. Energy Mater.* **2015**, *5*, 1401123.

[204] S. H. Choi, Y. N. Ko, J.-K. Lee, Y. C. Kang, *Adv. Funct. Mater.* **2015**, *25*, 1780.

[205] Y. N. Ko, S. H. Choi, S. B. Park, Y. C. Kang, *Nanoscale* **2014**, *6*, 10511.

[206] S. H. Choi, Y. C. Kang, *Nanoscale* **2015**, *7*, 6230.

[207] J. Mao, C. Luo, T. Gao, X. Fan, C. Wang, *J. Mater. Chem. A* **2015**, *3*, 10378.

[208] C. Luo, Y. Zhu, Y. Xu, Y. Liu, T. Gao, J. Wang, C. Wang, *J. Power Sources* **2014**, *250*, 372.

[209] A. Langrock, Y. Xu, Y. Liu, S. Ehrman, A. Manivannan, C. Wang, *J. Power Sources* **2013**, *223*, 62.

[210] T. Kodera, T. Ogihara, *J. Ceram. Soc. Japan* **2014**, *122*, 483.

[211] H. Zou, S. Li, X. Wu, M. J. McDonald, Y. Yang, *ECS Electrochem. Lett.* **2015**, *4*, A53.

[212] J. Ma, Z. Fang, Y. Yan, Z. Yang, L. Gu, Y.-S. Hu, H. Li, Z. Wang, X. Huang, *Adv. Energy Mater.* **2015**, *5*, 1500046.

[213] D. S. Jung, T. H. Hwang, J. H. Lee, H. Y. Koo, R. A. Shakoor, R. Kahraman, Y. N. Jo, M. Park, J. W. Choi, *Nano Lett.* **2014**, *14*, 4418.

[214] X. Wang, T. Gao, X. Fan, F. Han, Y. Wu, Z. Zhang, J. Li, C. Wang, *Adv. Funct. Mater.* **2016**, DOI 10.1002/adfm.201602264.

[215] X. Hu, F. Cheng, N. Zhang, X. Han, J. Chen, *Small* **2015**, *11*, 5545.

[216] T. Yuan, W. Zhang, W. Li, C. Song, Y.-S. He, J. M. Razal, Z.-F. Ma, J. Chen, *2D Mater.* **2015**, *2*, 24002.

[217] D. Zhang, B. Wang, Y. Jiang, P. Zhou, Z. Chen, B. Xu, M. Yan, *J. Alloys Compd.* **2015**, *653*, 604.

[218] H.-C. Youn, J. H. Jeong, K. C. Roh, K.-B. Kim, *Sci. Reports* **2016**, *6*, 30865.

[219] Y. Xu, Y. Zhu, F. Han, C. Luo, C. Wang, *Adv. Energy Mater.* **2015**, *5*, 1400753.

[220] M. Kim, T. R. Hinklin, R. M. Laine, *Chem. Mater.* **2008**, *27*, 5154.